

# Undular bottom topography as a salt intrusion mitigation measure

A study on the potential of trapped internal  
waves to enhance vertical mixing

T.M. (Tess) Wegman



Delft University of Technology

# Undular bottom topography as a salt intrusion mitigation measure

**A study on the potential of trapped internal waves  
to enhance vertical mixing**

by

T.M. (Tess) Wegman

to obtain the degree of Master of Science

at the Delft University of Technology,

to be defended publicly on January 25, 2021 at 14:30.

Student number: 4350324  
Thesis committee: Prof. dr. J.D. Pietrzak, TU Delft, chair  
Dr. ir. R.J. Labeur, TU Delft  
Dr. ir. W.M. Kranenburg, Deltares  
Prof. dr. ir. M. Verlaan, TU Delft

An electronic version of this thesis is available at <http://repository.tudelft.nl/>.  
Cover: picture by Gabriel Viisoreanu



# Preface

This thesis complements my masters in Hydraulic Engineering, and thereby finalises my study time at Delft University of Technology.

This study looks at the potential of internal waves generated over undular bottom topography as a salt intrusion mitigation measure. Salt intrusion is becoming an increasingly relevant problem worldwide. Due to the societal relevance, I felt motivated to work on this topic. I am glad that Julie Pietrzak and Wouter Kranenburg offered me the chance to work on this subject, where I could combine my interests of stratified flows and turbulent mixing processes. I am thankful that I got the opportunity to combine this research with an internship at Deltares. With lots of joy I investigated salt intrusion, internal waves and mixing processes. The topic was very challenging and therefore this thesis was a valuable learning experience. I learned a lot about the relevant physical processes and CFD modelling.

I would like to use this opportunity express my gratitude to everyone that contributed to my thesis, first of all my committee. I would like to thank Julie Pietrzak for sharing her knowledge on the topic and for always having a positive note to keep me motivated. Wouter Kranenburg, I appreciate the weekly meetings we had, where we exchanged ideas and where he challenged me with critical questions. I want to express my gratitude to Robert Jan Labeur for all his time and patience to help me with the model, for his detailed feedback and the stimulating discussions we had. Thanks to Martin for his critical feedback during the committee meetings to keep me sharp.

I would like to thank all my friends for the positive distractions, encouraging words and occasional proofreading. Special thanks goes out to Tjerk, for his unconditional support. I am very grateful for my family's support and their endless faith in me.

*T.M. (Tess) Wegman  
Delft, January 2021*

# Summary

Due to climate change and human interventions, saltwater intrusion is becoming a topic of increasing concern worldwide. Salt water intrudes into the Rotterdam Waterway (RWW) by an exchange flow, where the denser sea water propagates landwards at the bottom. The main competing mechanism for this stratified exchange flow is vertical mixing, which can be realised by internal wave induced shear instabilities or wave breaking. The goal of this study is to investigate whether internal waves generated over undular bottom topography in the RWW can generate additional vertical mixing. The underlying assumption is that a decrease in stratification decreases salt intrusion.

The approach to answer the main research question is a combination of an analytical and a numerical analysis. The analytical study is based on frictionless linear theory. Internal wave behaviour is further analysed with FinLab, a finite element model which includes the non-hydrostatic processes and effects of density differences. FinLab is evaluated for the application of this study by means of a validation case.

In the analytical study, linear theory is applied to obtain a relation between the bed wave parameters and average internal wave energy density  $E$  for internal waves generated over sinusoidal bottom topography in a linearly stratified fluid. The derived expression describes that the bottom topography amplitude  $h_0$  and bed wave number  $k_\tau$  both have a positive quadratic relation with the energy. Additionally,  $k_\tau$  influences the resonance conditions.

To validate FinLab for internal wave breaking and mixing an experiment in a wave tank, according to an example from literature, is simulated. The validation case reveals a shortcoming in the turbulent mixing parameterization. However, on scales relevant for the RWW the effect of this will not have the same significance. The validation case offers a suggestion for a subgrid closure of diffusion, where density effects are taken into account.

Numerical simulations of a 2D channel stretch with sinusoidal bottom topography, a linearly stratified fluid and a linearly varying background velocity, show generation of resonant trapped internal waves for the first two resonant modes. These occurrences correspond to the highest values of kinetic energy as function of vertical velocity averaged over the bed wave domain.

The vertical buoyancy flux  $b$  is downward directed during occurrences of internal waves and becomes upward directed for increasing background flow. Vertical mixing is associated with an increase in average potential energy  $\overline{E_p}$ , which is 17% higher for the base case (containing bed waves) than for a similar case without bed waves. This increase is larger when bottom shear stress increases. Richardson numbers below 0.25, associated with shear instabilities and mixing, are only observed near the bed, mainly when internal waves are present. The effect of variations in bottom topography wavelength  $L_\tau$  and amplitude  $h_0$  on internal wave energy can be explained by the analytical formulation. The effect of bed wave parameter changes on  $b$  and relative increase in  $\overline{E_p}$  can be related to the effect of the changed amount of bed friction rather than the difference in wave energy.

The first resonant mode is the most energetic, however, the average energy density found for these waves is only 0.4% to 6.7% of the potential energy anomaly (PEA); the energy required to fully mix a stratified water column. In the simulations the only mechanism that could transfer internal wave energy to turbulent kinetic energy are shear instabilities near the bed. Over the full simulation, the net vertical buoyancy transport is of negligible magnitude, where  $\overline{E_p}$  shows significant increases between 6% and 99% compared to similar cases without bed waves and is enhanced during the presence of internal waves. However, it is yet to be quantified how significant the vertical mixing caused by internal waves is.

The main discussion point is that the quantification of vertical mixing requires improvement, particularly to determine the importance of mixing by internal wave-induced shear instabilities and by bed shear. Mixing by local shear instabilities (of which the relevant scales cannot be resolved with the current grid resolution) does not have an adequate parameterization, because density effects are not included in the turbulence closure. The bed friction parameter, which greatly influences the behaviour of the system, has to be validated. Furthermore, cases where internal waves might break in practice (e.g. at banks) were not considered. Finally, the observed internal wave energy is of small magnitude, however field measurements by Pietrzak et al. (1991) shows that turbulence production by internal waves was significant.

# Contents

<b>Summary</b>	<b>ii</b>
<b>Nomenclature</b>	<b>vi</b>
<b>List of Figures</b>	<b>vii</b>
<b>List of Tables</b>	<b>x</b>
<b>1 Introduction</b>	<b>1</b>
1.1 Research context . . . . .	1
1.2 Problem statement . . . . .	2
1.3 Research objective . . . . .	2
1.4 Research approach . . . . .	3
1.5 Readers guide . . . . .	3
<b>2 Theoretical framework</b>	<b>4</b>
2.1 Salt intrusion in estuaries . . . . .	5
2.1.1 Forcing mechanisms of salt intrusion . . . . .	5
2.1.2 Measure of stratification . . . . .	5
2.2 Internal Waves . . . . .	6
2.2.1 Internal Waves in the Rotterdam Waterway . . . . .	6
2.2.2 Internal waves trapped to bottom topography . . . . .	7
2.2.3 Internal Froude number . . . . .	8
2.2.4 Internal wave energy . . . . .	8
2.3 Vertical mixing by internal waves . . . . .	9
2.3.1 Internal wave breaking . . . . .	9
2.3.2 Mixing efficiency . . . . .	9
2.4 Summary of theoretical framework . . . . .	10
<b>3 Analytical study</b>	<b>11</b>
3.1 Conceptual model . . . . .	11
3.2 Resonance conditions . . . . .	12
3.3 Energy content . . . . .	12
3.3.1 Derivation . . . . .	13
3.4 Influence of parameters . . . . .	16
3.4.1 Parameters influencing resonance conditions . . . . .	17
3.4.2 Parameters influencing magnitude . . . . .	18
3.5 Conclusion analytical study . . . . .	19
<b>4 Model description and validation</b>	<b>20</b>
4.1 FinLab . . . . .	20
4.1.1 Governing equations . . . . .	20
4.1.2 Model settings . . . . .	21
4.1.3 Model outputs . . . . .	22
4.2 Validation approach . . . . .	22
4.2.1 Earlier validation . . . . .	22
4.2.2 Experiment description and validation cases . . . . .	23
4.3 Results of validation . . . . .	23
4.3.1 Wave modes . . . . .	24
4.3.2 Energy balance . . . . .	26
4.3.3 Diffusion of salt . . . . .	28
4.3.4 Turbulence model and breaking . . . . .	30

4.4	Discussion of the model . . . . .	31
4.4.1	Ratio between dissipation and diffusion . . . . .	31
4.4.2	Relation to RWW model . . . . .	32
4.5	Conclusions validation . . . . .	33
<b>5</b>	<b>Numerical study: Parameter study</b>	<b>34</b>
5.1	Method . . . . .	34
5.1.1	Cases and set-up . . . . .	34
5.1.2	Methods of evaluation . . . . .	36
5.2	General response . . . . .	37
5.3	Comparison to reference cases . . . . .	40
5.3.1	Baroclinic flow over flat bottom . . . . .	40
5.3.2	Barotropic flow over sinusoidal bottom topography . . . . .	41
5.4	Analysis of vertical mixing . . . . .	42
5.4.1	Shear instabilities . . . . .	42
5.4.2	Vertical buoyancy flux . . . . .	42
5.5	Influence of bed friction . . . . .	44
5.5.1	Variations in Nikuradse roughness . . . . .	44
5.5.2	Frictionless bottom . . . . .	46
5.6	Variation of bottom topography parameters . . . . .	47
5.6.1	Bottom topography amplitude . . . . .	47
5.6.2	Bottom topography wavelength . . . . .	49
5.7	Summary parameter study . . . . .	51
<b>6</b>	<b>Discussion</b>	<b>52</b>
6.1	Quantification of vertical mixing . . . . .	52
6.1.1	Performance of the turbulence model . . . . .	52
6.1.2	Representation of diffusion in the model . . . . .	53
6.1.3	Linear stratification . . . . .	53
6.1.4	Wave breaking . . . . .	53
6.1.5	Quantification of mixing efficiency . . . . .	53
6.1.6	Significance of vertical mixing for salt intrusion . . . . .	54
6.2	Simplifications and assumptions in the model . . . . .	54
6.2.1	Velocity boundaries . . . . .	54
6.2.2	Rigid lid surface . . . . .	55
6.2.3	Internal wave reflection at open boundaries . . . . .	55
6.3	Practical applicability . . . . .	55
6.4	Concluding remarks . . . . .	55
<b>7</b>	<b>Conclusions and recommendations</b>	<b>56</b>
7.1	Conclusions . . . . .	56
7.2	Recommendations . . . . .	57
	<b>Bibliography</b>	<b>58</b>
<b>A</b>	<b>Case description: the Rotterdam Waterway</b>	<b>60</b>
<b>B</b>	<b>Resonance conditions</b>	<b>62</b>
<b>C</b>	<b>Workings of depth-averaging</b>	<b>65</b>
<b>D</b>	<b>Model settings</b>	<b>66</b>
<b>E</b>	<b>Derivation energy change FinLab</b>	<b>68</b>
<b>F</b>	<b>Additional figures</b>	<b>70</b>

# Nomenclature

## Roman symbols

$a_n$	forcing velocity of the wave paddle	rad./s
$b$	average vertical buoyancy flux	J/s/m <sup>3</sup>
$E$	total internal wave energy density	J/m <sup>3</sup>
$E_k$	kinetic energy	J/m <sup>3</sup>
$E_p$	potential energy	J/m <sup>3</sup>
$E_{k,z}$	kinetic energy as function of vertical velocity	J/m <sup>3</sup>
$E_{tot}$	total energy averaged over the wave tank	J/m <sup>3</sup>
$Fr_i$	internal Froude number	-
$h$	piezometric head	m
$L$	salt intrusion length	m
$Q_f$	river discharge	m <sup>3</sup> /s
$Ri$	gradient Richardson number	-
$Ri_f$	flux Richardson number	-
$S$	salinity	PSU
$\mathcal{M}$	irreversible mixing rate	J
$\mathcal{P}$	production of turbulent kinetic energy	J
$\hat{w}$	vertical velocity amplitude	m/s
$c_g$	wave group velocity	m/s
$c_i$	phase velocity of a moving fluid	m/s
$c_r$	phase velocity relative to the moving fluid	m/s
$C_s$	Smagorinsky constant	-
$G$	production and destruction of turbulence by buoyancy	J
$g$	gravitational acceleration	ms <sup>-2</sup>
$H$	water depth	m
$h_0$	amplitude of sinusoidal bottom topography	m
$k$	horizontal wave number	m <sup>-1</sup>
$k_n$	Nikuradse roughness	m
$k_\tau$	wave number of sinusoidal bottom topography	m <sup>-1</sup>
$L_\tau$	wavelength of sinusoidal bottom topography	m
$m$	vertical wave number	m <sup>-1</sup>

$N$	buoyancy frequency	$s^{-1}$
$P$	power delivered by the wave paddle	$Js^{-1}$
$s$	wave steepness	-
$u$	horizontal velocity	m/s
$U_0$	velocity of the background flow	m/s
$W$	work delivered by the wave paddle	J
$w$	vertical velocity	m/s
$x$	horizontal coordinate	m
$z$	vertical coordinate	m

**Greek symbols**

$\alpha$	amplitude of the wave paddle	rad.
$\Delta\rho$	density difference with respect to the reference density	$kg/m^3$
$\eta$	mixing efficiency	-
$\kappa$	diffusivity	$m^2/s$
$\kappa_t$	turbulence diffusivity	$m^2/s$
$\mu$	fluid viscosity	$Ns/m^2/s$
$\nu$	kinematic viscosity	$m^2/s$
$\nu_t$	eddy viscosity	$m^2/s$
$\omega$	radian frequency	rad./s
$\rho$	density	$kg/m^3$
$\rho_0$	constant reference density	$kg/m^3$
$\rho_w$	perturbation of isopycnals due to the internal wave	$kg/m^3$
$\sigma$	Prandtl-Schmidt number	-
$\tau_{sgs}$	subgrid stress	$Ns/m^2/s$
$\theta$	rotation of the wave paddle	rad.
$\varepsilon$	viscous dissipation	J
$\varphi$	potential energy anomaly (PEA)	$J/m^3$
$\zeta$	internal wave amplitude	m

**Diacritical marks**

$\langle \square \rangle$	time averaging
$\overline{\square}$	spatial averaging

# List of Figures

2.1	Conceptual model . . . . .	4
2.2	Schematic of gravitational circulation (Schulz, 2014) . . . . .	6
3.1	Energy conversions in an estuary with bottom topography . . . . .	11
3.2	Magnitude of the internal wave amplitude $\zeta$ for varying background flow velocity $U_0$ . Resonant conditions are met for different flow velocities corresponding to different internal wave modes marked with black dots (indicated on the right y-axis). Here $L_\tau = 50$ m, $N = 0.099$ s <sup>-1</sup> . . . . .	12
3.3	Schematic of sinusoidal bottom topography, with bottom topography wavelength $L_\tau$ and bottom topography amplitude $h_0$ . . . . .	13
3.4	Vertical velocity $w$ as function of water depth $z$ for mode 1, 2 and 3, described by Equation 3.8. With $U_0 = 0.41$ m/s, $h_0 = 0.50$ m, $N = 0.099$ s <sup>-1</sup> , at $x = 0$ m . . . . .	15
3.5	Ratio between internal wave energy density and potential energy anomaly ( $E/\varphi$ see Equation 3.15) for varying flow velocity $U_0$ . Resonant conditions are met for different flow velocities corresponding to different internal modes. Here $L_\tau = 50$ m, $h_0 = 0.5$ m and $N = 0.099$ s <sup>-1</sup> . . . . .	16
3.6	Internal wave energy density for varying flow velocities $U_0$ and bottom topography wavelength $L_\tau$ . Here $h_0 = 0.5$ m and $N = 0.099$ s <sup>-1</sup> . . . . .	17
3.7	The ratio between internal wave energy density and potential energy anomaly $E/\varphi$ for varying flow velocities $U_0$ . Variations in $L_\tau$ causes a shift of the resonant conditions to higher $U_0$ for larger $L_\tau$ . Here $h_0 = 0.5$ m and $N = 0.099$ s <sup>-1</sup> . . . . .	18
3.8	The ratio between internal wave energy density and potential energy anomaly $E/\varphi$ for varying bottom topography amplitude $h_0$ . For different flow velocities near mode 1 resonance ( $U_0 = 0.41$ m/s) an exponential relation between energy density and $h_0$ is visible. Here $L_\tau = 50$ m and $N = 0.099$ s <sup>-1</sup> . . . . .	18
3.9	The ratio between internal wave energy density and potential energy anomaly $E/\varphi$ for varying bottom topography wavelength $L_\tau$ . For different flow velocities near mode 1 resonance ( $U_0 = 0.41$ m/s) an exponential relation between energy density and $h_0$ is visible. Here $h_0 = 0.5$ m and $N = 0.099$ s <sup>-1</sup> . . . . .	19
4.1	Experimental set-up from McEwan (1983), numerical simulations are based on the same set-up, however with dimensions of Taylor (1992) . . . . .	23
4.2	Run 2A: forced mode 2,1 structure . . . . .	24
4.3	Run 4A: forced mode 3,1 structure . . . . .	25
4.4	Mean values of energy Run 2A (600x60), showing that the difference between the total energy $E_{tot}$ and work by the wave maker $W$ increase linearly in time. Here $\sigma = 1$ and $\nu = 10^{-6}$ m <sup>2</sup> /s . . . . .	26
4.5	Total energy $E_{tot}$ and work of the wave maker $W$ over time shows that the total energy in the tank becomes larger than the input delivered by the wave maker. Simulations with medium resolution (600x60), $\sigma = 1$ and $\nu = 10^{-6}$ m <sup>2</sup> /s . . . . .	27
4.6	Fluctuation total energy and work wave maker. Amplitude of total energy and work wave maker Run 2A (600x60), $\sigma = 1$ , $\nu = 10^{-6}$ m <sup>2</sup> /s . . . . .	28
4.7	Effect of different Prandtl-Schmidt number $\sigma$ . Total energy and work wave maker Run 2A and Run 2B showing the difference between $\sigma = 1$ and $\sigma = 100$ . Here $\nu = 10^{-6}$ m <sup>2</sup> /s . . . . .	29
4.8	Run 2B (600x60) for a low amount of diffusion, here $\sigma = 100$ and $\nu = 10^{-6}$ m <sup>2</sup> /s . . . . .	29
4.9	Difference in grid resolution. Total energy $E_{tot}$ and work wave maker $W$ showing the difference for a low (300x30, Run 2C), medium (600x60, Run 2A) and extra fine (1340x240, Run 2D) grid. Here $\sigma = 1$ and $\nu = 10^{-6}$ m <sup>2</sup> /s . . . . .	30
4.10	Difference between turbulence models showing total energy $E_{tot}$ and work $W$ wave maker Run 2A for LES and Run 2E $k - \varepsilon$ model. Here $\sigma = 1$ and $\nu = 10^{-6}$ m <sup>2</sup> /s . . . . .	31

5.1	Domain of the modelling cases. Sinusoidal bottom topography is located between $x = -X$ and $x = X$ m. . . . .	34
5.2	Mode 1 structure where the internal wave is trapped to the bottom topography at $t = 180$ minutes when $U_0 = 0.50$ m/s for case <i>L50h050</i> . . . . .	38
5.3	Mode 2 structure where the internal wave is trapped to the bottom topography at $t = 100$ minutes when $U_0 = 0.28$ m/s for case <i>L50h050</i> . . . . .	38
5.4	Kinetic energy $\overline{E_{k,z}}$ and vertical density flux $b$ for the base case <i>L50h050</i> . . . . .	39
5.5	Comparison between the base case <i>L50h050</i> (solid line) and the reference case without bottom topography <i>ref_nbw</i> (dashed line). Domain-averaged kinetic energy $\overline{E_{k,z}}$ , domain-averaged vertical buoyancy flux $b$ , domain-averaged potential energy $\overline{E_p}$ and total density flux $\frac{d\overline{E_p}}{dt}$ for a linearly increasing background flow $U_0$ . . . . .	40
5.6	Domain-averaged kinetic energy $\overline{E_{k,z}}$ for the base case and two reference cases. The reference cases without bed waves ( <i>ref_nbw</i> ) and without stratification ( <i>ref_barotrop</i> ) have a negligible amount of kinetic energy compared to the base case with stratification and bottom topography ( <i>L50h050</i> ). . . . .	41
5.7	Richardson number $Ri$ for base case <i>L50h050</i> where $h_0 = 0.50$ m and $L_\tau = 50$ m . . . . .	42
5.8	Domain-averaged vertical velocity $w$ and vertical buoyancy flux $b$ plotted over time for case <i>L50h050</i> . . . . .	43
5.9	Pressure field in the bed wave domain for the base case <i>L50h050</i> where $h_0 = 0.50$ m and $L_\tau = 50$ m . . . . .	43
5.10	Density field [kg/m <sup>3</sup> ] of the full domain for the base case <i>L50h050</i> where $h_0 = 0.50$ m and $L_\tau = 50$ m . . . . .	44
5.11	Domain averaged kinetic energy $\overline{E_{k,z}}$ over bed wave domain for cases <i>L50h050</i> , <i>kn_02</i> and <i>kn_0002</i> showing influence with different values of Nikuradse roughness $k_n$ . The kinetic energy increases for a lower bed friction. . . . .	45
5.12	Effect of varying Nikuradse bed roughness $k_n$ on energy parameters . . . . .	45
5.13	Density field [kg/m <sup>3</sup> ] of case <i>kn_0</i> which has a frictionless bed, at $t = 150$ minutes when $U_0 = 0.42$ m/s when high amplitude mode 1 internal waves have overturning structures . . . . .	46
5.14	Difference between the base case without bottom friction <i>kn_0</i> (solid line) and the reference case without bottom topography or bottom friction <i>kn_0_nbw</i> (dashed line). Domain-averaged kinetic energy $\overline{E_{k,z}}$ , domain-averaged vertical buoyancy flux $b$ , domain-averaged potential energy $\overline{E_p}$ and total density flux $\frac{d\overline{E_p}}{dt}$ for a linearly increasing background flow $U_0$ . . . . .	46
5.15	The effect of varying bottom topography amplitude $h_0$ on domain-averaged kinetic energy $\overline{E_{k,z}}$ . For higher values of $h_0$ the energy content is higher. . . . .	47
5.16	Effect of varying bottom topography amplitude $h_0$ on energy parameters . . . . .	48
5.17	Richardson number $Ri$ for simulation <i>L50h150</i> where $h_0 = 1.50$ m and $L_\tau = 50$ m . . . . .	48
5.18	Density field [kg/m <sup>3</sup> ] for simulation <i>L50h150</i> where $h_0 = 1.50$ m and $L_\tau = 50$ m overturning structures near the bottom at $t = 180$ minutes . . . . .	49
5.19	The effect of varying bottom topography wavelength $L_\tau$ on domain-averaged kinetic energy $\overline{E_{k,z}}$ . For higher values of $L_\tau$ the maxima shifts to later time instances, corresponding to higher flow velocities . . . . .	50
5.20	Effect of varying bottom topography wavelength $L_\tau$ on energy parameters . . . . .	50
A.1	Characteristic density profile of the RWW, measurement taken at 16:07 near Hoek van Holland (51.9732313, 4.121972) on 06-07-2016 . . . . .	60
A.2	a) Schematic of stratification in an estuary, adapted from Groenenboom et al. (2019) b) Idealized cross-sectionally averaged salinity vs distance along estuary, adapted from Lerczak et al. (2009) . . . . .	61
B.1	Magnitude of the internal wave amplitude $\zeta$ for varying background flow velocity $U_0$ . Resonant conditions are met for flow velocities of 0.26, 0.19, 0.14 and 0.11 m/s with corresponding internal modes 1, 2, 3 and 4 respectively. Internal wave modes are marked with black dots (indicated on the right y-axis). Here $L_\tau = 20$ m, $N = 0.099$ s <sup>-1</sup> . . . . .	62
B.2	Magnitude of the internal wave amplitude $\zeta$ for varying background flow velocity $U_0$ . Resonant conditions are met for flow velocities of 0.34, 0.21, 0.15 and 0.11 m/s with corresponding internal modes 1, 2, 3 and 4 respectively. Internal wave modes are marked with black dots (indicated on the right y-axis). Here $L_\tau = 30$ m, $N = 0.099$ s <sup>-1</sup> . . . . .	63
B.3	Magnitude of the internal wave amplitude $\zeta$ for varying background flow velocity $U_0$ . Resonant conditions are met for flow velocities of 0.38, 0.22, 0.15 and 0.12 m/s with corresponding internal modes 1, 2, 3 and 4 respectively. Internal wave modes are marked with black dots (indicated on the right y-axis). Here $L_\tau = 40$ m, $N = 0.099$ s <sup>-1</sup> . . . . .	63

B.4	Magnitude of the internal wave amplitude $\zeta$ for varying background flow velocity $U_0$ . Resonant conditions are met for flow velocities of 0.41, 0.23, 0.15 and 0.12 m/s with corresponding internal modes 1, 2, 3 and 4 respectively. Internal wave modes are marked with black dots (indicated on the right y-axis). Here $L_\tau = 50$ m, $N = 0.099$ s <sup>-1</sup> . . . . .	63
B.5	Magnitude of the internal wave amplitude $\zeta$ for varying background flow velocity $U_0$ . Resonant conditions are met for flow velocities of 0.43, 0.23, 0.16 and 0.12 m/s with corresponding internal modes 1, 2, 3 and 4 respectively. Internal wave modes are marked with black dots (indicated on the right y-axis). Here $L_\tau = 60$ m, $N = 0.099$ s <sup>-1</sup> . . . . .	64
B.6	Magnitude of the internal wave amplitude $\zeta$ for varying background flow velocity $U_0$ . Resonant conditions are met for flow velocities of 0.44, 0.23, 0.16 and 0.12 m/s with corresponding internal modes 1, 2, 3 and 4 respectively. Internal wave modes are marked with black dots (indicated on the right y-axis). Here $L_\tau = 70$ m, $N = 0.099$ s <sup>-1</sup> . . . . .	64
D.1	Domain discretization where the domain has three different regions with different horizontal resolution . . . . .	67
F.1	Kinetic energy $\overline{E_{k,z}}$ and vertical density flux $b$ for case <i>L50h025</i> . . . . .	70
F.2	Kinetic energy $\overline{E_{k,z}}$ and vertical density flux $b$ for the base case <i>L50h075</i> . . . . .	71
F.3	Kinetic energy $\overline{E_{k,z}}$ and vertical density flux $b$ for the base case <i>L50h100</i> . . . . .	71
F.4	Kinetic energy $\overline{E_{k,z}}$ and vertical density flux $b$ for the base case <i>L50h150</i> . . . . .	72
F.5	Kinetic energy $\overline{E_{k,z}}$ and vertical density flux $b$ for the base case <i>L20h050</i> . . . . .	72
F.6	Kinetic energy $\overline{E_{k,z}}$ and vertical density flux $b$ for the base case <i>L30h050</i> . . . . .	73
F.7	Kinetic energy $\overline{E_{k,z}}$ and vertical density flux $b$ for the case <i>L40h050</i> . . . . .	73
F.8	Kinetic energy $\overline{E_{k,z}}$ and vertical density flux $b$ for the base case <i>L60h050</i> . . . . .	74
F.9	Kinetic energy $\overline{E_{k,z}}$ and vertical density flux $b$ for the base case <i>L70h050</i> . . . . .	74
F.10	Difference between the a case with (solid line) and without (dashed line) bottom topography for a case with tidal flow $U_0$ with a velocity amplitude of 0.5 m/s. Domain-averaged kinetic energy $\overline{E_{k,z}}$ , vertical buoyancy flux $b$ , domain-averaged potential energy $\overline{E_p}$ and total density flux $\frac{d\overline{E_p}}{dt}$ . . . . .	75
F.11	Difference between the a case with (solid line) and without (dashed line) bottom topography for a case with a linearly increasing flow velocity up to a maximum of 0.5 m/s. Domain-averaged kinetic energy $\overline{E_{k,z}}$ , vertical buoyancy flux $b$ , domain-averaged potential energy $\overline{E_p}$ and total density flux $\frac{d\overline{E_p}}{dt}$ . . . . .	76

# List of Tables

4.1	Validation runs . . . . .	26
5.1	Parameters of the base case <i>L50h050</i> . . . . .	35
5.2	Cases parameter study . . . . .	36
A.1	Typical parameters RWW (Rijkswaterstaat, 2020a, Zijta, 2019) . . . . .	61
D.1	Model settings validation case . . . . .	66
D.2	Model settings RWW case . . . . .	67

# Introduction

Deltaic areas are increasingly vulnerable areas due to climate change. This is alarming, because these areas have a relatively large population density compared to the average population density on Earth (Ericson et al., 2006). Deltas are inhabited by 4.6% of the world's population, while these areas contribute to only 0.4% of the global land surface without ice cover (Ericson et al., 2006). Populations in delta areas have been living under increasing flood risk due to relative sea level rise, mainly caused by human actions (Ericson et al., 2006).

Another process threatening river deltas is saltwater intrusion. Due to climate change and human interventions this is becoming an increasingly relevant topic of concern worldwide. Saltwater intrusion is the flow of saline (sea)water into freshwater bodies, such as rivers and aquifers. Seawater intrusion has adverse effects on both the environment and economic activities of the affected area. The ecology in fresh water is negatively impacted. Fresh water resources cannot be guaranteed for industrial purposes. This is noticed by shortages of irrigation water in agricultural areas and shortages of cooling water in the industry. Also the facilitation of drinking water can be at risk (Mikhailova, 2013, Pörtner et al., 2019).

## 1.1 Research context

In the Netherlands the Rhine Meuse Delta is susceptible to saltwater intrusion. This delta, which is connected to the sea by the Rotterdam Waterway (RWW), is densely populated and extensively used for agricultural and industrial purposes. Periods of low river discharge, taking place during dry periods, are the most critical conditions for saltwater intrusion. Due to climate change and human interventions those extreme conditions are expected to occur more frequently in the future (Drinkwaterplatform, 2019). To guarantee fresh water resources in the Rhine Meuse Delta, Rijkswaterstaat has been investigating mitigation measures for saltwater intrusion through the Corporate Innovatieprogramma (CIP).

Gravitational circulation is an important salt import mechanism in the RWW. Gravitational circulation is a net exchange flow which takes place in an estuary, where fresh river water and saline seawater interact. Averaged over a tidal cycle freshwater flows seawards at the surface and salt water flows landwards at the bottom. In many estuaries the presence of both saline and fresh water cause a stratified system. Vertical mixing is the main competing mechanism for stratification. Under low discharge conditions, a decrease in stratification reduces salt intrusion. Hence CIP studies of 2015 to 2017 investigated measures based on the principles of increased vertical mixing. Examples of possible solutions are pumping vessels, bubble boats and constructing flow channels in the 'Splittingsdam'. Pumping vessels and bubble boats were found most effective for vertical mixing, however they require a lot of power (Groenenboom and Veenstra, 2017). From 2018 onward more nature-based solutions were posed (Van der Heijden, 2018). The possibility to generate extra turbulence and mixing by dredged trenches on the river bed was explored.

This gave inspiration for a currently investigated measure, generating internal waves over dredged river bed topography. Periodic bed forms have the potential to create resonant internal waves in a stratified fluid. Consequently larger wave heights and local turbulence production is stimulated (Klymak et al., 2012). Those internal waves contain energy that can contribute to the vertical mixing and potentially reduce stratification. The ques-

tion still remains whether those internal waves, generated over bottom topography, can be an effective measure against salt intrusion in estuaries.

Many studies from the past support that internal waves contribute to increased turbulent transport of mass and momentum (e.g. Kranenburg (1988), Pietrzak et al. (1991), Hogg et al. (2017)), and hereby have the potential to decrease the salt intrusion length (Pietrzak et al., 1991). Field campaigns conducted in the years 1987 and 1988 in the RWW, analysed by various studies (Pietrzak et al. (1990), Pietrzak et al. (1991), Kranenburg et al. (1991)), showed the presence of large-amplitude (trapped) internal waves linked to the periodic bottom topography in the RWW. These studies support the idea that internal waves generated over bottom topography could be a promising mitigation measure to salt intrusion through the RWW.

Proper development and design of salt intrusion mitigation measures, requires a good prediction of salt intrusion. Such prediction includes how, where, when and for how long salt intrusion takes place (NWO, 2020). These predictions can be made by large-scale 3D-models. The main challenge of salt intrusion modelling, is that small-scale and non-hydrostatic processes cannot be neglected, while they cannot be directly resolved in large-scale models. These processes are relevant for the general behaviour of interaction of salt and fresh water, but also for the mitigation measures that could be integrated. The effects of the processes that are not resolved in the model, can be included through parametrizations. For mitigation measures affecting the small scale processes, their effect needs to be included, which requires that the effects of the mitigation measure are well understood. In the context of internal waves, breaking and mixing behaviour of internal waves has to be quantified.

## 1.2 Problem statement

The Netherlands has an increased risk of saltwater intrusion due to dry summers with low river discharges (Rijkswaterstaat, 2020b, Waterforum, 2018). One of the salt intrusion mitigation measures which is currently under investigation for the RWW is changing the bed topography such, that internal waves can be generated.

This study aims to take a step towards using internal waves generated over bottom topography as an effective salt intrusion mitigation measure. The first step towards a salt intrusion mitigation measure is knowing how this mitigation measure behaves on a small scale. Relevant aspects are quantifying to what extend those internal waves can reduce stratification and under what circumstances.

The focus of this study will be on when (near-)resonant waves are generated, how much energy they contain, how much of their energy can be utilized for vertical mixing and thereby reduce stratification.

## 1.3 Research objective

The objective of this study is to investigate whether internal waves generated over undular bottom topography in the RWW can generate a significant additional amount of vertical mixing and thus reduce stratification. The hypothesis is that this additional vertical mixing breaks down stratification. This is relevant, because the expectation is that reduced stratification results in a decrease of horizontal salt intrusion. This is based on the assumption that the landward transport under critical conditions for salt intrusion is governed by gravitational circulation. The main research question to be answered in this study is:

*Can internal waves, generated over bottom topography, contribute to vertical mixing and hereby reduce stratification in estuaries?*

To answer the main research question the sub-questions listed below will be answered. Considering undular bottom topography and critical conditions in the RWW:

1. What bottom topography configurations are suitable to generate resonant internal waves?
2. How much energy do those internal waves contain and how does this relate to the amount of energy required to fully mix a stratified water column?
3. Through what processes is internal wave energy converted into turbulent kinetic energy and how much of the internal wave energy is converted to vertical mixing?

4. What is the relation between bottom topography wavelength and wave amplitude and the amount of vertical mixing?

## 1.4 Research approach

To answer the research questions the concepts of the generation of resonant internal waves over bottom topography and the vertical mixing that these internal waves can generate have to be understood and described.

This study starts with an analytical study to apply the known theory on the problem. The numerical modelling tool applied in this study is evaluated for the present application by means of a validation case. A numerical study is done to study the generation and mixing behaviour of internal waves. Throughout this study the case of the RWW is used as a reference situation to obtain relevant parameters.

The analytical analysis uses linear theory to obtain understanding under which circumstances resonant internal waves are generated. An analytical approach has limitations for the prediction of the internal wave amplitude and consequently the energy content of the waves in near-resonant conditions. Describing complex stratified flow behaviour and quantifying the mixing generated by internal waves can be best approached by numerical modelling. Key elements that this numerical modelling tool should capture are density differences and non-hydrostatic processes.

FinLab is a finite element model for transport and non-hydrostatic flow (Labeur, 2009). As concluded by Pietrzak and Labeur (2004) and Van der Boon (2011) FinLab is suitable for reproducing internal waves over bed topography and non-linear and non-hydrostatic effects of (breaking) internal waves. FinLab is verified for internal wave-induced mixing by simulating lab experiments by Taylor (1992).

## 1.5 Readers guide

Chapter 2 extends the theoretical framework in addition to the literature outline given in the research context. Chapter 3 gives results of the analytical study. Chapter 4 explains the numerical modelling tool and the model validation. Chapter 5 shows results of the numerical study, which are discussed in Chapter 6. Chapter 7 draws the main conclusions and gives recommendations for future studies.

# 2

## Theoretical framework

To study the effect on stratification by resonant internal waves generated over undular bottom topography the understanding of several physical processes is crucial. First, the relation between decreased stratification and salt intrusion in estuaries. Second, several energy conversions can be distinguished when tidal flow over topography generates internal waves (Chen et al., 2013). When the barotropic tide flows over topography, part of this barotropic energy is converted to baroclinic energy in form of internal waves (Figures 2.1a and 2.1b). The internal wave energy can be transferred to turbulent kinetic energy (TKE) through the mechanisms of wave breaking and wave-induced shearing (Figure 2.1c). The effectiveness of mixing is expressed in a mixing efficiency.

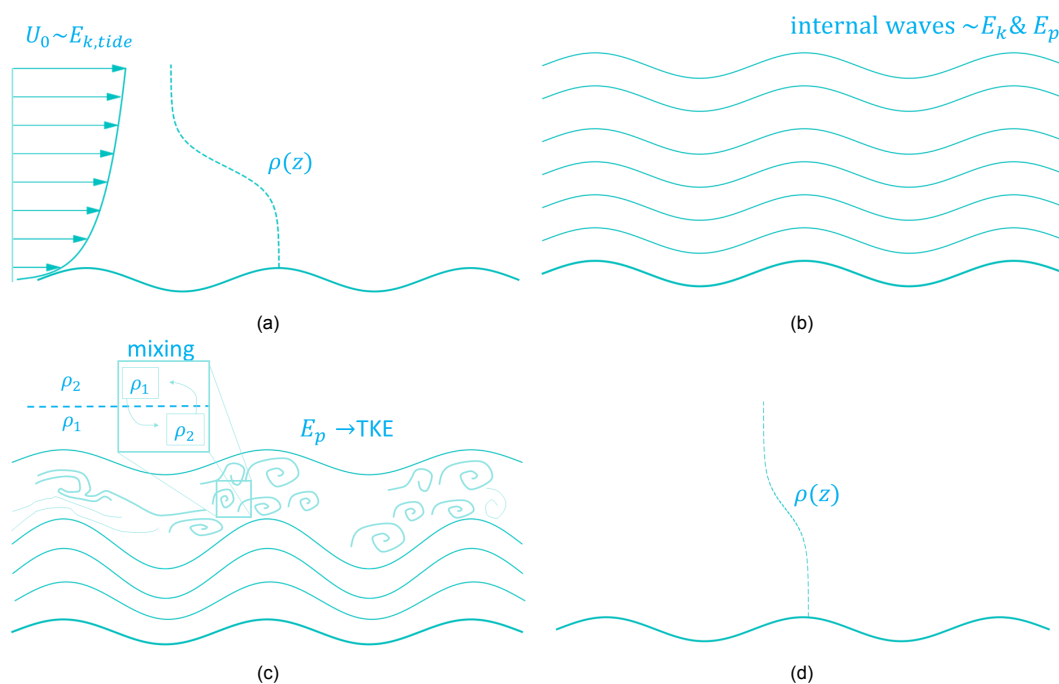


Figure 2.1: Conceptual model

In short the following processes are relevant:

1. the relation between vertical mixing and salt intrusion length;
2. internal wave generation over topography, especially near-resonant conditions;
3. internal wave energy transmission to TKE by wave shearing and breaking;
4. mixing of the stratified water column due to released TKE.

## 2.1 Salt intrusion in estuaries

The hypothesis of this study is that an increase in vertical mixing by internal waves reduces stratification. The relevance of this study is found in the underlying assumption that a reduction in stratification leads to a decrease in salt intrusion. This section explains the mechanisms leading to salt intrusion, to further verify this assumption.

### 2.1.1 Forcing mechanisms of salt intrusion

An estuary is defined as the transition from saline seawater to fresh river water. The balance between external forcing mechanisms determines the physical conditions of an estuary. In most partially mixed estuaries, such as the RWW, the dominant forcing mechanisms are river discharge and the tide (Geyer and MacCready, 2014, Lerczak et al., 2009).

The two main forcing mechanisms affect salt intrusion length as follows (Lerczak et al., 2009)

1. **Increase in river discharge** increases stratification due to the added buoyancy of freshwater. Furthermore, it reduces salt intrusion length due to seaward advection of the salt intrusion.
2. **Increase in tidal forcing** causes an increase in vertical mixing and shear stress, and a resulting decrease in gravitational circulation and stratification.

Internal waves could also bring about additional vertical mixing, with similar effects to tidal induced vertical mixing. Under critical conditions for salt intrusion in the RWW there is a low river discharge. A relatively small increase in river discharge increases buoyancy and hereby counteracts with (wave-induced) mixing for the final effect on stratification.

A tidally averaged longitudinal salt balance of an estuary can be defined according to an advection-diffusion equation (Lerczak et al., 2009). This describes the competition between flushing by river flow and import by horizontal dispersion.

For an idealised estuary, with a linear salinity distribution between  $S = S_0$  at the sea side  $x = 0$  and  $S = 0$  at the freshwater boundary  $x = L$  (see Figure A.2), the length-integrated advection-diffusion equation is described by Lerczak et al. (2009) according to

$$\frac{1}{2}AS_0 \frac{dL}{dt} = -Q_f S_0 + \alpha \frac{(g\beta)^2 H^8}{\kappa^3} A \frac{S_0^3}{L^3} \quad (2.1)$$

From Equation 2.1 follows that an increase in vertical mixing  $\kappa$  results into a decrease in salt intrusion length  $L$ . Furthermore, this equation shows that an increase in water depth  $H$  gives a significant increase in salt intrusion length. An increase in river discharge  $Q_f$  decreases salt intrusion length. The definition of the remaining parameters can be found in Lerczak et al. (2009).

Kranenburg and van der Kaaij (2019) found that gravitational circulation is the main salt import mechanism in the RWW. Gravitational circulation is driven by the longitudinal density difference in an estuary, this happens at an open boundary between fresh river water and saline seawater, see schematic of Figure 2.2. The residual flow pattern is characterised by a landward propagating salt wedge at the bottom and a seaward-directed freshwater plume at the top of the water column (Geyer and MacCready, 2014). Therefore this flow pattern is also referred to as exchange flow.

### 2.1.2 Measure of stratification

As discussed in Section 2.1.1, salt intrusion can be reduced by a reduction in stratification. Therefore two parameters are introduced to quantify the measure of stratification.

#### Potential Energy Anomaly

The potential energy anomaly is the amount of work per unit volume required to achieve a fully mixed fluid. In this study internal wave energy is a relevant parameter which can be linked to the measure of stratification in

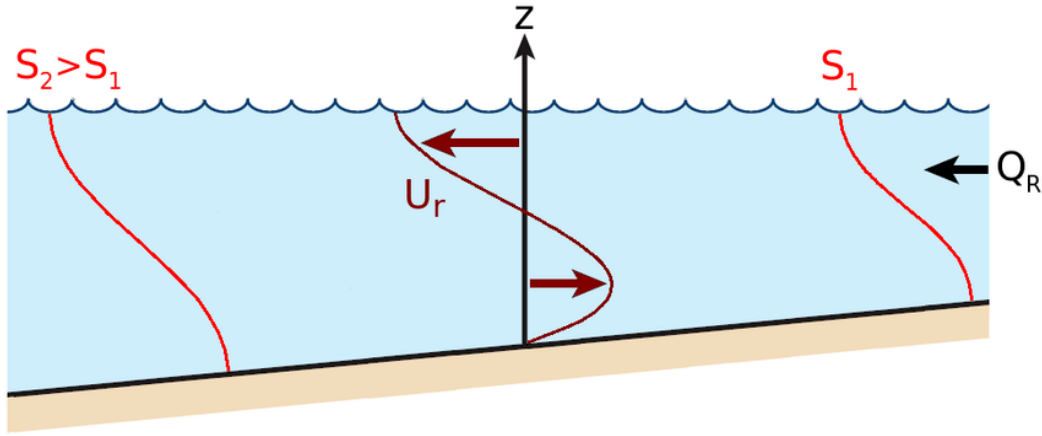


Figure 2.2: Schematic of gravitational circulation (Schulz, 2014)

terms of energy density. The potential energy anomaly  $\varphi$  ( $\text{Jm}^{-3}$ ) is given by

$$\varphi = \frac{1}{H} \int_{-h}^{\eta} (\bar{\rho} - \rho)gzdz \quad (2.2)$$

Here  $\rho(z)$  is the density of the water column as a function of the vertical coordinate  $z$ .  $H$  is the height of the fluid with an average density of  $\bar{\rho}$ . The free surface is given by  $\eta$ , the depth of the bed by  $h$  and  $g$  is the gravitational acceleration (Simpson et al., 1990).

### Buoyancy frequency

Alternatively the degree of stratification can be expressed by the buoyancy frequency. For a linearly stratified water column the buoyancy frequency is constant over depth, which makes it a convenient parameter in mathematical expressions. The buoyancy frequency  $N$  ( $\text{s}^{-1}$ ) is given by

$$N^2(z) = -\frac{g}{\rho_0} \frac{\partial \rho}{\partial z}. \quad (2.3)$$

where  $\rho_0$  is reference density.  $N$  is the frequency at which a displaced water particle will oscillate when it is displaced vertically within a stratified water column. Hence this is a local variable.

## 2.2 Internal Waves

Internal waves are gravity waves that can exist in a stratified fluid. The wave propagates as disturbances of the isopycnals, relative to isopycnals for a stratified fluid at rest. Internal waves can grow by extracting energy from the system. In the RWW this is kinetic energy from the background flow.

This section describes how the system works that generates the resonant trapped internal waves and what determines the conditions for resonance.

### 2.2.1 Internal Waves in the Rotterdam Waterway

Field campaigns conducted in the RWW in the years 1987 and 1988, showed the presence of large-amplitude (trapped) internal waves linked to the periodic bottom topography (Pietrzak et al. (1990), Pietrzak et al. (1991), Kranenburg et al. (1991)). Resonant internal waves with wave heights up to 4 m were observed in the roughly 16 m deep channel (Pietrzak et al., 1990). Those waves are present under certain conditions of the background flow, of which the variation is governed by the tide (Pietrzak et al., 1990).

During measurement campaigns internal waves were observed during subcritical flow, with Froude numbers

ranging from 0.9 to 0.6 (Pietrzak and Labeur, 2004). Higher amplitudes for resonant internal waves were found during flood than during ebb, this can be explained by relatively larger near-bed velocities during flood due to estuarine circulation (Kranenburg et al., 1991). The wavelengths of those high-amplitude waves were governed by the wavelength of the periodic bottom topography. Linear theory under quasi-steady flow conditions can predict the resonant flow conditions, however cannot predict the wave amplitudes (Pietrzak et al., 1990) (see Equation 2.8 in Section 2.2.2).

Pietrzak and Labeur (2004) investigates the internal wave behaviour with the non-hydrostatic finite element numerical model FINEL3D. The model proves it can reproduce the linear behaviour under stationary flow conditions in accordance with data from the RWW. In non-linear simulations with time-dependence, resonant internal waves are observed as the flow becomes subcritical.

### 2.2.2 Internal waves trapped to bottom topography

For internal waves over topography two different categories can be distinguished; subcritical and supercritical topography, depending on the ratio between wave steepness and topography steepness. Generation behaviour of internal waves in the case of subcritical topography is relatively linear, like in the RWW (Pietrzak and Labeur, 2004, Pietrzak et al., 1990)).

In non-hydrostatic conditions vertical accelerations cannot be neglected. Assuming linear theory under the Boussinesq approximation in a linearly stratified fluid, the vertical velocity can be described by the Taylor-Goldstein equation (Pietrzak and Labeur, 2004)

$$\frac{d^2 \hat{w}}{dz^2} + \{l^2 - k^2\} \hat{w} = 0 \quad (2.4)$$

here  $z$  is the vertical coordinate and  $k$  the horizontal wave number of the free wave, given by

$$k^2 = \frac{N^2}{c_r^2} - \frac{n^2 \pi^2}{H^2} \quad (2.5)$$

$N$  is the buoyancy frequency (see Equation 2.3),  $H$  is water depth and  $c_r$  is the relative phase velocity. The phase speed of the internal waves with respect to the bed  $c_i$  is given by

$$c_i = U_0 + c_r = 0 \quad (2.6)$$

which is zero in case of internal waves trapped to the topography. This implies that the relative phase velocity  $c_r$  is equal and oppositely directed to the background flow  $U_0$ . Here  $U_0$  is considered to be depth-uniform and in the case of trapped internal waves  $l^2$  is given by

$$l^2 = \frac{N^2}{U_0^2} \quad (2.7)$$

Considering a bottom boundary condition with sinusoidal bed waves, internal wave amplitude  $\zeta$  can be described by (Pietrzak and Labeur, 2004)

$$\zeta(x, z) = h_0 \frac{\sin \left[ (l^2 - k^2)^{1/2} (H - z) \right]}{\sin \left[ (l^2 - k^2)^{1/2} H \right]} \sin(k_\tau x) \quad (2.8)$$

with bottom topography wave number  $k_\tau$

$$k_\tau = \frac{2\pi}{L_\tau} \quad (2.9)$$

where  $h_0$  is bottom topography amplitude and  $L_\tau$  is the bottom topography wavelength.

From the formulation for  $\zeta$  can be explained when resonance occurs. In case of a sinusoidal bottom topography this occurs for an internal wavelength equal to the wavelength of the bottom topography (Pietrzak et al., 1990), hence  $k = k_\tau$ . In this case the magnitude of  $c_r$  equals  $U_0$  and for every vertical wave mode ( $n = 0, 1, 2, \dots$ ) the denominator of Equation 2.8 goes to zero and the amplitude goes to infinity. For this reason the internal wave amplitude is not predictable with linear theory near-resonant conditions (Kranenburg et al., 1991).

### 2.2.3 Internal Froude number

Flow behaviour of wave perturbations can be partially predicted by the internal Froude Number, which can be defined as follows (Pietrzak and Labeur, 2004)

$$Fr_i = \frac{U_0}{c_r} \quad (2.10)$$

The flow is internally supercritical for  $Fr_i > 1$  and internally subcritical for  $Fr_i < 1$ . Resonant trapped internal waves are generated when  $Fr_i = 1$ . This also explains, why trapped internal waves can start propagating when the flow velocity starts deviating from the velocity corresponding to the velocity of wave generation.

For subcritical conditions long waves can propagate upstream, which will influence the upstream conditions. This phenomenon should be taken into account for numerical modelling.

### 2.2.4 Internal wave energy

Describing internal waves in terms of their energy content creates the possibility to relate this to the degree of stratification ( $\varphi$ ) and once the waves start releasing their energy with resulting mixing, expressing this in a mixing efficiency (see Section 2.3.2.)

Internal wave energy  $E$  can be defined as the sum of kinetic energy  $E_k$  (Equation 2.12) and available potential energy  $E_p$  (Equation 2.13) (Moum et al., 2007):

$$E = E_k + E_p \quad (2.11)$$

with

$$E_k = \frac{1}{2} \rho_0 u^2 \quad (2.12)$$

and

$$E_p = \rho_w g z \quad (2.13)$$

where  $u$  is the wave velocity. For a continuously stratified water column this energy is expressed per unit volume ( $\text{Jm}^{-3}$ ) and for interfacial waves (e.g. on the interface of a two-layered system) as the energy of the entire water column, per unit horizontal area ( $\text{Jm}^{-2}$ ) (Kundu et al., 2016).  $E_p$  is the portion of potential energy that is present due to the (wave) perturbations in the fluid. Therefore  $E_p$  is the fraction of potential energy that can potentially be converted to turbulent kinetic energy, and thereby contribute to mixing (Chen et al., 2013, Moum et al., 2007).

Density  $\rho$  is defined by

$$\rho(x, z, t) = \rho_0 + \rho_b(z) + \rho_w(x, z, t) \quad (2.14)$$

where  $\rho_0 + \rho_b(z)$  is the background density (dependent on  $z$ ) and  $\rho_w(x, z, t)$  is the perturbation of isopycnals due to the internal wave (Moum et al., 2007).

## 2.3 Vertical mixing by internal waves

Turbulence can be brought to regions of stable stratification by

- Wave shearing;
- Wave breaking.

The result is a decay in wave height (Kranenburg, 1988). Pietrzak et al. (1991) concludes that the generation of turbulent kinetic energy of non-breaking internal waves cannot be neglected with respect to the turbulent kinetic energy produced by the background flow, especially for short internal waves. Low values of the local Richardson number (Equation 2.15) are associated with increased local shear due to internal waves and results in shear instabilities (Kranenburg et al., 1991). Turbulence measurements by Uittenbogaard and Imberger (1993) found displacement length scales between 20 and 200 mm of internal waves in the RWW.

This section further describes internal wave breaking. The Richardson number is described, because it gives a measure of the stability of the stratification. The mixing efficiency describes the effectiveness of mixing by internal waves.

### 2.3.1 Internal wave breaking

In the wave breaking process, turbulence is produced and irreversible energy dissipation takes place. Section 2.3.2 further discusses how this mixing can be formulated.

Internal waves can break due to two causes (Uittenbogaard, 1995):

1. Instantaneous unstable density gradient, this happens when  $\frac{\partial \rho}{\partial z} > 0$ ;
2. Hydrodynamic Kelvin-Helmholtz instability, this happens when locally and temporally  $Ri < \frac{1}{4}$ ;
3. Wave steepness.

The gradient Richardson number  $Ri$  gives a balance between turbulent mixing  $\left(\frac{\partial u}{\partial z}\right)^2$  and stratification  $\frac{\partial \rho}{\partial z}$ .  $Ri$  is given by

$$Ri = -\frac{g \frac{\partial \rho}{\partial z}}{\rho \left(\frac{\partial u}{\partial z}\right)^2} \quad (2.15)$$

where  $\rho$  is the average density of the fluid (Venayagamoorthy and Koseff, 2016). The stability criterion for a stably stratified fluid is  $Ri > \frac{1}{4}$ .

In the case of a shear instability, wave breaking occurs when a wave reaches a critical amplitude (Uittenbogaard, 1995). Nonlinear wave-wave interactions can drive the wave energy to higher wave numbers. This causes an increase in wave steepness (Holloway, 1988, Laurent et al., 2001).

Wave steepness  $s$  is derived from the Froude number and is given by (Staquet and Sommeria, 2002):

$$s = \frac{u_{max}}{c_r} \quad (2.16)$$

here  $u_{max}$  is the maximum wave induced horizontal velocity and  $c_r$  is the wave speed relative to the moving fluid. Waves are statically stable for  $s < 1$  and statically unstable for  $s > 1$ . Therefore internal waves are expected to break for  $s > 1$ . Note that this criterion holds for propagating waves.

### 2.3.2 Mixing efficiency

In the end, it is relevant to quantify how much of the turbulent kinetic energy can be effectively used for mixing, and hence for the break down of stratification. Fluid motions from turbulence can lead to either stirring or mixing. Here stirring is associated with a lifted fluid particle that can later fall under the influence of gravity. Through this reversible process the density of the fluid is not changed. When irreversible mixing occurs the fluid density

changes. Hereby, the loss of kinetic energy provides energy for the potential energy of the water column to increase. To distinguish between these reversible and irreversible processes, Peltier and Caulfield (2003) defines the mixing efficiency  $\eta$  as 'the ratio of irreversible increases in the potential energy of the density distribution to the irreversible loss of kinetic energy'

$$\eta = \frac{\mathcal{M}}{\mathcal{M} + \varepsilon} \quad (2.17)$$

Here  $\mathcal{M}$  is the irreversible mixing rate and  $\varepsilon$  the viscous dissipation. If all the available energy for mixing is utilized, there is no dissipation of energy, then Equation 2.17 becomes equal to one.

A more practical definition of mixing efficiency for internal waves is given by Taylor (1992)

$$\eta = \frac{b}{\partial(APE)/\partial t} \quad (2.18)$$

here  $b$  is the average buoyancy flux and  $APE$  is the available potential energy in the internal waves.

In current literature it is still unknown what the efficiency of mixing of breaking internal waves is (Klymak et al., 2012).

## 2.4 Summary of theoretical framework

It is known that salt intrusion in the RWW for the most critical cases occurs due to gravitational circulation. A reduction of stratification is promising to counteract salt intrusion by gravitational circulation. There have been observations of high amplitude internal waves generated over bottom topography in the RWW. Linear theory can predict when these resonant waves are generated. However, the amplitude of those near-resonant internal waves have to be predicted by a numerical model. Also the amount of mixing that those internal waves can bring about and the efficiency of the energy transfer of internal wave energy to turbulent kinetic energy utilized for mixing is unknown.

## Analytical study

This chapter outlines physical concepts for the generation of internal waves over undular bottom topography. Those concepts are qualitatively and where possible quantitatively described. This is done for a simplified stratified flow case (linearly stratified fluid) with linear internal waves.

### 3.1 Conceptual model

Relevant physical concepts to analyse the effectiveness of internal waves generated over bottom topography as a potential salt intrusion mitigation measure, can be described by subsequent energy conversions in an estuary with bottom topography (see chart of Figure 3.1).

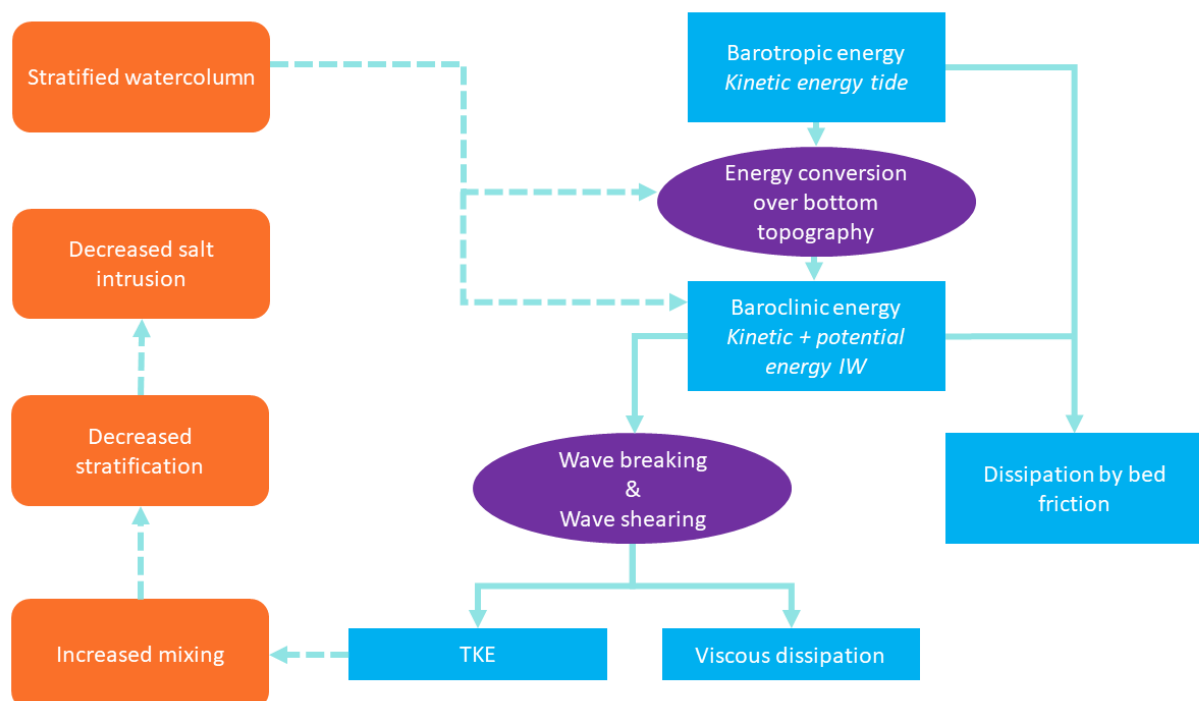


Figure 3.1: Energy conversions in an estuary with bottom topography

## 3.2 Resonance conditions

In Figure 3.2 internal wave amplitudes are plotted, based on Equation 2.8. This case, the base case, is inspired on parameters and dimensions typical for the RWW. A linearly stratified fluid is assumed for the purpose of the analytical approach. The density  $\rho$  varies between  $1000 \text{ kg/m}^3$  and  $1015 \text{ kg/m}^3$  in a channel of 15 m depth, approximately the mean depth according to Rijkswaterstaat (2020a). This corresponds to a buoyancy frequency of  $N = 0.099 \text{ s}^{-1}$ . Sinusoidal bed waves with a bottom topography amplitude  $h_0$  of 0.50 m and bottom topography wavelength  $L_\tau$  of 50 m is applied. These values are based on the typical values for bottom topography wavelengths (30 to 80 m) and bottom topography amplitudes (0.5 to 1.0 m) found by Pietrzak et al. (1990) in a field campaign in the RWW. The magnitude of the amplitude of Figure 3.2 is determined for flow velocities varying between 0.1 and 0.8 m/s, which are common tidal flow velocities in the RWW (see Table A.1). In the rest of this study these parameters are the basic assumptions, unless stated otherwise.

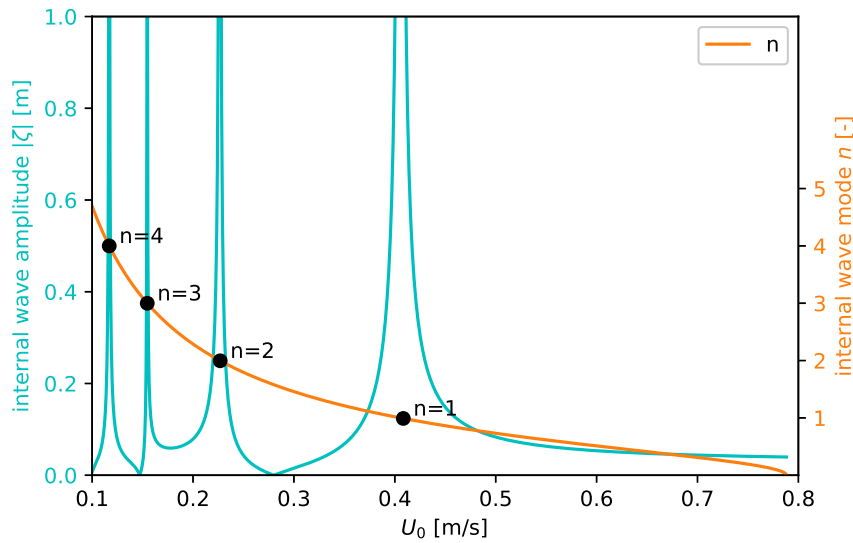


Figure 3.2: Magnitude of the internal wave amplitude  $\zeta$  for varying background flow velocity  $U_0$ . Resonant conditions are met for different flow velocities corresponding to different internal wave modes marked with black dots (indicated on the right y-axis). Here  $L_\tau = 50 \text{ m}$ ,  $N = 0.099 \text{ s}^{-1}$

The infinite internal wave amplitudes belong to resonant conditions for the corresponding vertical wave modes. This gives an indication which background flow velocities are most likely to generate resonance. Appendix B shows variations on Figure 3.2 with other values of  $L_\tau$ .

The moments of infinite wave amplitudes, correspond to moments with a large wave energy density. It is of great importance to know at which time instances a high wave energy content occurs, because then internal waves have a higher tendency of vertical mixing and hence have more potential to decrease stratification.

## 3.3 Energy content

An expression is derived to estimate the internal wave energy density for internal waves generated over sinusoidal bottom topography (Figure 3.3). In the remain of this study purely sinusoidal bed waves are assumed with bottom topography wavelength  $L_\tau$  and bottom topography amplitude  $h_0$ . Internal wave energy density is expressed in the same unit as potential energy anomaly (PEA). The latter is the amount of energy required to fully mix a stratified water column. Hence comparing the internal wave energy to the PEA, puts into perspective how much energy is available for mixing and how much energy is required to fully mix the water column.

For this analysis sinusoidal linear waves in a linearly stratified fluid are considered. Due to occurring resonance (hence values going to infinity), the solution becomes singular. However, expressing the internal wave energy content for internal trapped waves, gives an insight into the relevant parameters.

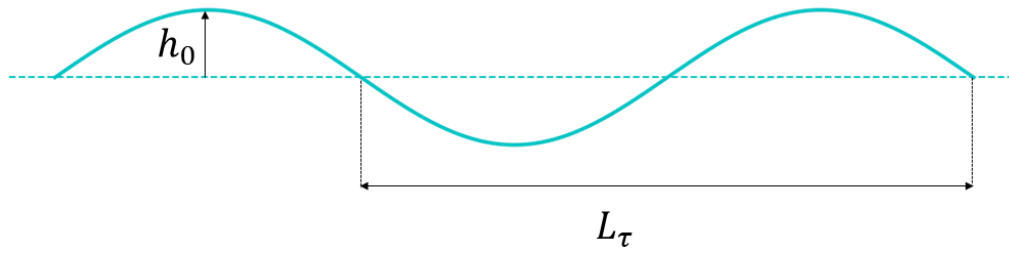


Figure 3.3: Schematic of sinusoidal bottom topography, with bottom topography wavelength  $L_\tau$  and bottom topography amplitude  $h_0$

First, the internal wave energy content is expressed in a form suitable to rewrite it in terms of internal waves generated over sinusoidal bottom topography based on Kundu et al. (2016). A solution for internal waves generated over bottom topography is derived from Pietrzak and Labeur (2004) to substitute in the energy equation. Finally the parameters of this expression are categorized in parameters relevant for resonance conditions and parameters influencing the magnitude of internal wave energy density.

### 3.3.1 Derivation

For a linearly stratified fluid, under Boussinesq assumption, a constant background flow  $U_0$  and no viscous dissipation an expression for internal wave energy for internal waves over sinusoidal bottom topography is derived.

Purely sinusoidal waves are assumed, hence the vertical wave velocity  $w$  can be expressed as follows

$$w(x, z, t) = \hat{w}(z) \cdot e^{i(kx - \omega t)} \quad (3.1)$$

Here  $k$  is horizontal wave number,  $m$  is vertical wave number and  $\omega$  is radian frequency. For trapped internal waves over sinusoidal bottom topography vertical velocity is not a full wavelength over depth, therefore  $w$  is written such that the vertical velocity amplitude  $\hat{w}$  has dependency of  $z$ .

From this starting point the average wave energy over one wavelength per unit volume can be expressed in terms of vertical velocity amplitude  $\hat{w}$ . Expressing internal wave energy in terms of  $\hat{w}$  creates the possibility to substitute a solution to the Taylor-Goldstein equation for internal waves generated over sinusoidal bottom topography in an expression for internal wave energy. First the derivation from Kundu et al. (2016) is summarized and applied to trapped wave generated over sinusoidal bottom topography.

#### Expression for internal wave energy density

The horizontal momentum equation (Equation 3.2) and buoyancy equation (Equation 3.3) (of the linear inviscid Boussinesq equations) are rewritten in terms of  $\hat{w}$  with a substitution of  $w$  (Kundu et al., 2016):

$$\frac{\partial u}{\partial t} = -\frac{1}{\rho_0} \frac{\partial p'}{\partial x} \quad \rightarrow \quad u = -\frac{m}{k} \hat{w}(z) \cdot e^{i(kx - \omega t)} \quad (3.2)$$

$$\frac{\partial \rho_w}{\partial t} = \frac{N^2 \rho_0}{g} w \quad \rightarrow \quad \rho_w = i \frac{N^2 \rho_0}{\omega g} \hat{w}(z) \cdot e^{i(kx - \omega t)} \quad (3.3)$$

The parameters  $u$ ,  $w$  and  $\rho_w$  appear in the energy equations in quadratic form. The average over one wavelength of  $\cos^2(x)$  equals  $\frac{1}{2}$  (Kundu et al., 2016). Horizontal wave-length averaged expressions for  $u$ ,  $w$  and  $\rho_w$  are given by

$$\overline{u^2} = \frac{m^2}{k^2} \hat{w}^2(z) \frac{1}{2}, \quad \overline{w^2} = \hat{w}^2(z) \frac{1}{2} \quad \text{and} \quad \overline{\rho_w^2} = \frac{N^4 \rho_0^2}{\omega^2 g^2} \hat{w}^2(z) \frac{1}{2} \quad (3.4)$$

Those squared quantities can be substituted in expressions for kinetic and potential energy to obtain the wavelength averaged internal wave energy content as a function of vertical velocity amplitude. For the kinetic energy  $E_k$  Kundu et al. (2016) finds

$$E_k = \frac{1}{2} \rho_0 \overline{(u^2 + w^2)} = \frac{1}{4} \rho_0 \left( \frac{m^2}{k^2} + 1 \right) \hat{w}^2(z) \quad (3.5)$$

For the potential energy  $E_p$  Kundu et al. (2016) finds

$$E_p = \frac{g^2 \rho_w^2}{2 \rho_0 N^2} = \frac{N^2 \rho_0}{4 \omega^2} \hat{w}^2(z) = \frac{1}{4} \rho_0 \left( \frac{m^2}{k^2} + 1 \right) \hat{w}^2(z) \quad (3.6)$$

Summing up  $E_k$  and  $E_p$  gives the total average energy per unit area. The total wave energy depends on the reference density  $\rho_0$ , horizontal and vertical wave number  $k$  and  $m$  and vertical velocity amplitude  $\hat{w}$  according to (Kundu et al., 2016)

$$E = E_k + E_p = \frac{1}{2} \rho_0 \left( \frac{m^2}{k^2} + 1 \right) \hat{w}^2(z) \quad (3.7)$$

In the next step  $\hat{w}^2(z)$  is depth averaged to obtain the average energy density per unit volume.

### Expression for vertical velocity amplitude

Pietrzak and Labeur (2004) solves the Taylor-Goldstein equation (Equation 2.4) to find vertical velocity  $w$  as function of horizontal coordinate  $x$  and vertical coordinate  $z$ . Here the bottom boundary is at  $z = 0$  and the surface boundary is at  $z = H$ . Below the formulation is given as function of vertical  $z$  coordinate

$$w(z) = k_\tau U_0 h_0 \frac{\sin \left[ (l^2 - k^2)^{1/2} (H - z) \right]}{\sin \left[ (l^2 - k^2)^{1/2} H \right]} \quad (3.8)$$

The solution is based on a bottom boundary condition of sinusoidal bed waves according to Pietrzak and Labeur (2004)

$$\hat{w}(x, z = h_0 \cos(k_\tau x)) = U_0 \frac{dh}{dx} = k_\tau U_0 h_0 \cos(k_\tau x) \quad (3.9)$$

Section 2.2.2 gives the definitions of all the parameters above. Equation 3.8 for  $w$  can be rewritten in a form of vertical velocity amplitude with dependency of the vertical coordinate  $\hat{w}(z)$

$$\hat{w}(z) = \hat{w} \cdot \sin \left[ (l^2 - k^2)^{1/2} (H - z) \right] \quad (3.10)$$

This is the vertical velocity amplitude with dependency of  $z$  which was defined by  $\hat{w}(z)$  in Equation 3.1.

### Substitution

Plotting  $w$  as a function of  $z$  for different modes according to Equation 3.8 shows the behaviour of vertical velocity over depth in Figure 3.4.

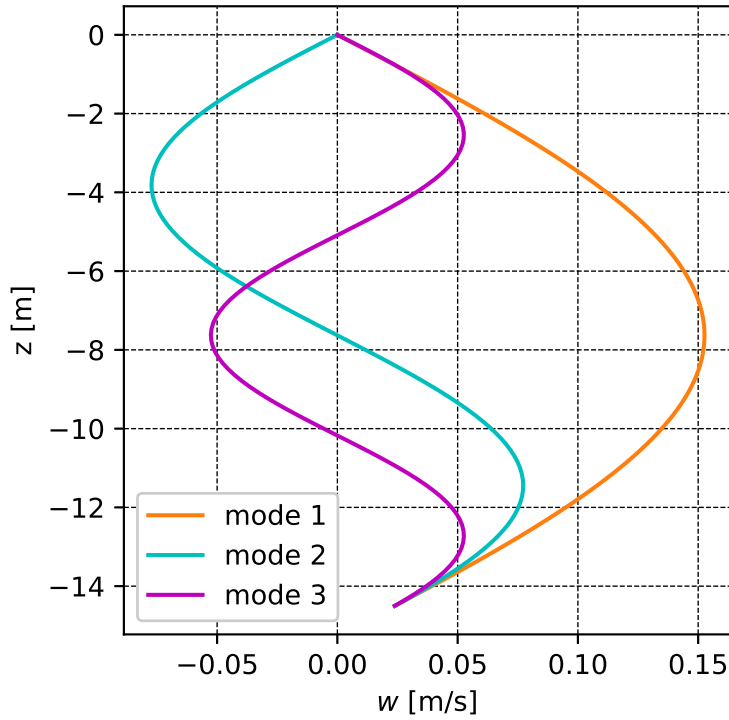


Figure 3.4: Vertical velocity  $w$  as function of water depth  $z$  for mode 1, 2 and 3, described by Equation 3.8. With  $U_0 = 0.41$  m/s,  $h_0 = 0.50$  m,  $N = 0.099$  s $^{-1}$ , at  $x = 0$  m

Now  $\widehat{w}^2(z)$  (Equation 3.10) is depth averaged to substitute in the expression of  $E$  given by Equation 3.7. A more detailed working can be found in Appendix C.

$$\overline{\widehat{w}^2(z)} = \frac{1}{H} \int_0^H \widehat{w}^2 \cdot \sin^2 \left[ (l^2 - k^2)^{1/2} (H - z) \right] dz = \widehat{w}^2 \left( \frac{1}{2} - \frac{\sin \left[ 2H (l^2 - k^2)^{1/2} \right]}{4H (l^2 - k^2)^{1/2}} \right) \quad (3.11)$$

Resonant trapped waves are generated when the background flow has the same magnitude as the wave celerity. Then  $|c_r| = |U_0|$  holds and in this case  $(l^2 - k^2)$  reduces to  $n\pi H$  with  $n = 1, 2, 3, \dots$ . In this case Equation 3.11 reduces to  $\frac{1}{2}\widehat{w}^2$ . From Equation 3.11 can be seen that the right term between brackets goes to zero for cases of resonance.

Now the internal wave energy (Equation 3.7) can be expressed in relevant parameters for internal waves generated over sinusoidal bottom topography. This is done by substitution of  $\widehat{w}^2(z)$  (Equation 3.11) which yields

$$E = \frac{1}{2} \left( \frac{m^2}{k^2} + 1 \right) \frac{\rho_0 k_\tau^2 U_0^2 h_0^2 \left( \frac{1}{2} - C \right)}{\left( \sin^2 \left[ (l^2 - k^2)^{1/2} H \right] \right)} \quad (3.12)$$

with  $C$  according to

$$C = \frac{\sin \left[ 2H (l^2 - k^2)^{1/2} \right]}{4H (l^2 - k^2)^{1/2}} \quad (3.13)$$

From Equation 3.12 can be seen which parameters influence the energy density of internal waves. This will be further elaborated on in Section 3.4.

### Relation internal wave energy content and potential energy anomaly

The internal wave energy content is related to the potential energy anomaly  $\phi$  (Equation 2.2), the amount of energy required to fully mix a stratified water column.

$$\phi = \frac{1}{H} \int_0^H \left( \frac{\rho_{\text{bottom}} - \rho_{\text{surface}}}{2} - \left( \rho_{\text{surface}} - (\rho_{\text{bottom}} - \rho_{\text{surface}}) \frac{z}{H} \right) \right) g z dz = \frac{gH}{12} (\rho_{\text{bottom}} - \rho_{\text{surface}}) \quad (3.14)$$

From this the ratio between internal wave energy density and potential energy anomaly  $\frac{E}{\phi}$  is determined

$$\frac{E}{\phi} = \frac{6}{gH (\rho_{\text{bottom}} - \rho_{\text{surface}})} \left( \frac{m^2}{k^2} + 1 \right) \frac{\rho_0 k_\tau^2 U_0^2 h_0^2 \left( \frac{1}{2} - C \right)}{\left( \sin^2 \left[ (l^2 - k^2)^{1/2} H \right] \right)} \quad (3.15)$$

For a linearly stratified flow ranging from 1000 to 1015 kg/m<sup>3</sup> the PEA is 184 J/m<sup>3</sup>. Figure 3.5 shows the ratio between internal wave energy density and potential energy anomaly (PEA) for the base case described in Section 3.2.

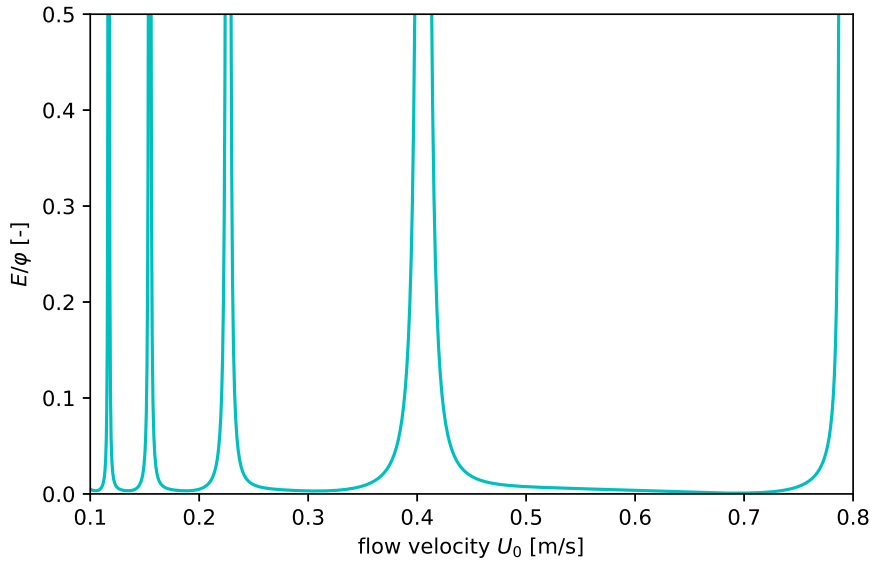


Figure 3.5: Ratio between internal wave energy density and potential energy anomaly ( $E/\phi$  see Equation 3.15) for varying flow velocity  $U_0$ . Resonant conditions are met for different flow velocities corresponding to different internal modes. Here  $L_\tau = 50$  m,  $h_0 = 0.5$  m and  $N = 0.099$  s<sup>-1</sup>

In this case a substantial amount of wave energy with respect to PEA is generated only around the resonance conditions.

## 3.4 Influence of parameters

For a good insight into parameters relevant for the design of bed waves suitable to generate a lot of internal wave energy, the parameters of Equation 3.12 can be distinguished between two categories:

- Parameters influencing the resonant conditions:
  - present wave structure determined by  $k$  and  $m$ ;

- wave number of the bed wave form  $k_\tau$ ;
- velocity of the background flow  $U_0$  ( $k$  is function of  $U_0$ );
- stratification expressed in buoyancy frequency  $N$  ( $k$  and  $l$  are functions of  $N$ ).
- Parameters influencing the magnitude of internal wave energy density:
  - amplitude of the bed wave form  $h_0$ ;
  - velocity of the background flow  $U_0$ ;
  - wave number of the bed wave form  $k_\tau$ .

Here water depth  $H$  and reference density  $\rho_0$  are assumed constant parameters.

### 3.4.1 Parameters influencing resonance conditions

The ratio between the generated internal wave energy density divided by the PEA is shown in Figure 3.5 similar to the graph of Figure 3.2.

Figure 3.5 shows the parameters relevant for the resonant conditions. For varying **background flow velocity**  $U_0$  different internal wave modes are generated (different peaks). Those peaks correspond to different **internal modes**  $n$  with their corresponding vertical wave number  $m$ . The lower modes (which are usually more distinct) are found for higher background velocities. For varying **bottom topography wavelength**  $L_\tau$  the resonance conditions shift to higher background flow velocities for larger  $L_\tau$ . Figure 3.6 also shows that the range of velocities upon which resonance occurs is larger for larger  $L_\tau$ .

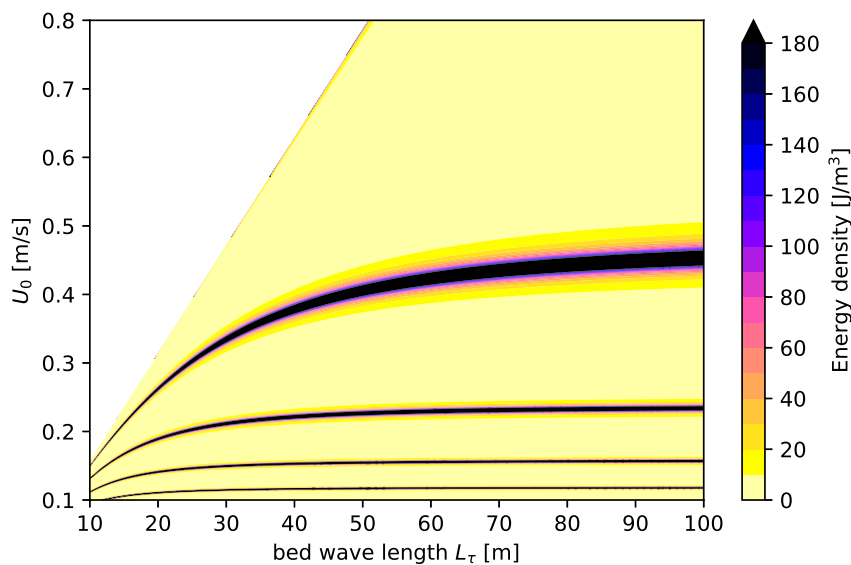


Figure 3.6: Internal wave energy density for varying flow velocities  $U_0$  and bottom topography wavelength  $L_\tau$ . Here  $h_0 = 0.5$  m and  $N = 0.099$  s $^{-1}$

When  $U_0$  is plotted against the ratio between internal wave energy density and potential energy anomaly  $E/\varphi$  (Figure 3.7) for different bottom topography wavelengths, also for smaller  $L_\tau$  the resonant peaks shift to lower flow velocities. Additionally, the range of near-resonance is wider, causing a longer time frame of high energy conditions.

Varying **buoyancy frequency**  $N$  shifts the resonance conditions to higher background flow velocity for increasing buoyancy frequency (corresponding to a stronger stratification).

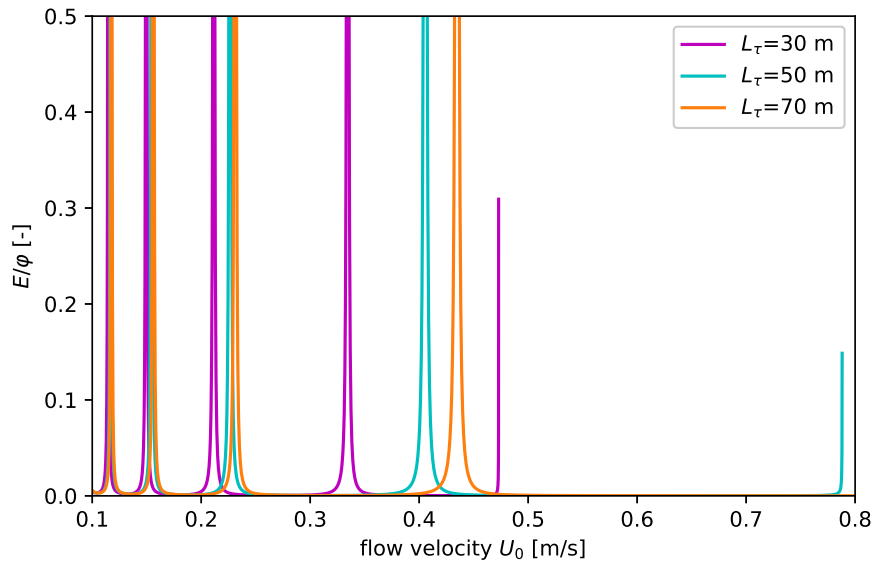


Figure 3.7: The ratio between internal wave energy density and potential energy anomaly  $E/\varphi$  for varying flow velocities  $U_0$ . Variations in  $L_\tau$  causes a shift of the resonant conditions to higher  $U_0$  for larger  $L_\tau$ . Here  $h_0 = 0.5$  m and  $N = 0.099$  s $^{-1}$

### 3.4.2 Parameters influencing magnitude

The ratio between the generated internal wave energy density divided by the PEA for varying **bottom topography amplitude**  $h_0$  is shown in Figure 3.8. In this case an exponential increase of internal wave energy content for increasing bottom topography amplitude is observed.

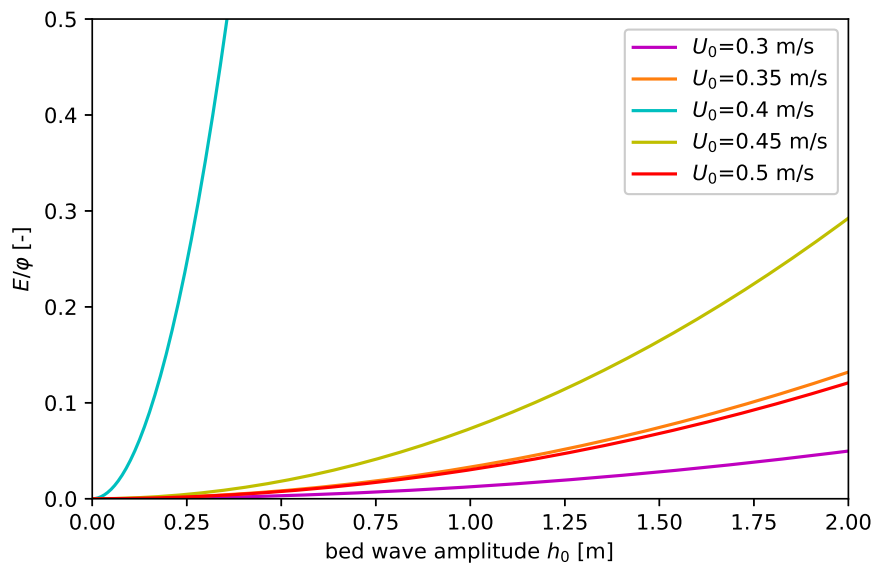


Figure 3.8: The ratio between internal wave energy density and potential energy anomaly  $E/\varphi$  for varying bottom topography amplitude  $h_0$ . For different flow velocities near mode 1 resonance ( $U_0 = 0.41$  m/s) an exponential relation between energy density and  $h_0$  is visible. Here  $L_\tau = 50$  m and  $N = 0.099$  s $^{-1}$

The effect of **bottom topography wave number** on the magnitude of the energy is that with a larger  $k_\tau$  (so smaller bottom topography wavelength) the energy increases exponentially. As mentioned in Section 3.4.1 this bottom topography wave number is also influencing the resonance conditions. When  $L_\tau$  is plotted against  $E/\varphi$  (Figure 3.9) this behaviour is dominated by resonance conditions.

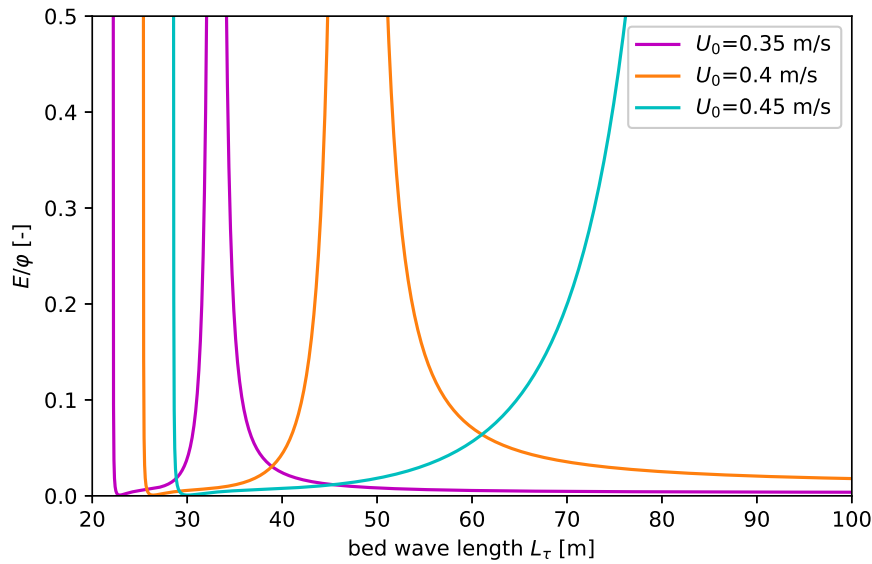


Figure 3.9: The ratio between internal wave energy density and potential energy anomaly  $E/\varphi$  for varying bottom topography wavelength  $L_\tau$ . For different flow velocities near mode 1 resonance ( $U_0 = 0.41$  m/s) an exponential relation between energy density and  $h_0$  is visible. Here  $h_0 = 0.5$  m and  $N = 0.099$  s $^{-1}$

Variation of **background flow velocity**  $U_0$  has an additional effect than determining the resonance conditions. From Figure 3.5 can be seen that the lower modes, which are generated under a higher background flow have a broader range of near-resonance, with a high energy content.

### 3.5 Conclusion analytical study

Equation 3.12 gives an estimation of internal wave energy density for internal waves generated over sinusoidal bottom topography. Important parameters to quantify the wave energy generated by sinusoidal bottom topography can be distinguished between parameters that lead to the resonance condition and parameters that influence the magnitude.

Linear theory can predict when resonance occurs and when most wave action can be expected. However, when resonance is reached the equation does not mathematically hold anymore. At these moments there is a lot of internal wave energy generated with respect to the PEA according to the analytical formulation.

How much of the internal wave energy will be suitable for mixing depends on the effectiveness of transmission processes, such as shear instabilities and internal wave breaking. Such mixing efficiency is not approachable by analytical analysis. The amount of generated energy around resonance and the mixing by internal waves is further investigated with a numerical model in Chapter 5.

# 4

## Model description and validation

This study requires deep insight into complex flow problems with varying density, where non-hydrostatic phenomena are important. Describing behaviour of high amplitude internal waves and possible breaking by these waves goes beyond the possibilities of an analytical approach. For near-resonant waves Kranenburg et al. (1991) found overestimations of 45% of the wave height by using the small-amplitude model and thus suggests a numerical model which solves the non-linear initial-value problem for large-amplitude waves. Therefore, this problem can be best approached with a non-hydrostatic model.

This study uses FinLab, a finite element model for transport and non-hydrostatic flow (Labeur, 2009).

This chapter describes FinLab and the model settings. FinLab is verified for internal wave-induced mixing by numerical simulations of a lab experiment in a wave tank by Taylor (1992).

### 4.1 FinLab

#### 4.1.1 Governing equations

The governing equations implemented in FinLab are derived from the incompressible isotherm Navier-Stokes equations. They are given by Equations (4.1) to (4.3) (Labeur, 2009).

*Continuity equation:*

$$\nabla \cdot \vec{u} = 0 \quad (4.1)$$

*Momentum equation:*

$$\frac{\partial(\rho\vec{u})}{\partial t} + \nabla \cdot (\rho\vec{u} \otimes \vec{u}) + \nabla p - \nabla \cdot (2\mu\nabla^s\vec{u}) = \vec{f} \quad (4.2)$$

Here  $\nabla^s = \frac{1}{2}\nabla(\cdot) + \frac{1}{2}\nabla(\cdot)^T$  is the symmetric gradient operator with fluid viscosity  $\mu$ . The external forces acting on the fluid are  $f$ .

*Transport equation:*

$$\frac{\partial\phi_i}{\partial t} + \vec{u} \cdot \nabla\phi_i - \nabla \cdot (\kappa_t\nabla\phi_i) = f_i \quad (4.3)$$

Here transport is described as a mass fraction of constituent  $i$  by means of  $\phi_i = \rho_i/\rho$  and  $\kappa_t$  is the turbulence diffusivity.

## 4.1.2 Model settings

### Initial conditions

Initial conditions have to be imposed on the model. These consist of a divergence free velocity field and a density distribution.

### Boundary conditions

The domain has to be enclosed by boundaries. FinLab has various possibilities of boundary conditions, of which the following have been used.

- Wall boundary, closed boundary with friction described by a Nikuradse wall roughness  $k_n$ ;
- Symmetrical boundary, closed frictionless boundary;
- Velocity boundary, open boundary where a velocity is imposed. This can be a constant velocity or a velocity with time dependence;
- For the inflow boundaries also an inflow concentration is imposed.

For the specific runs the exact application of those boundary conditions and initial conditions are stated in the corresponding chapter.

### Time integration

Crank-Nicolson scheme which is used for time integration, with implicitness of the momentum equation of 1. The advantage of the Crank-Nicolson scheme is that it introduces damping and reduces the spin-up. Also Fractional-Step is used, this is a relatively fast method, which reduces the calculation time.

### Turbulence modelling

FinLab has two turbulent close models; the  $k - \varepsilon$  model and the Large Eddy Simulation (LES) model. LES solves the large turbulent eddies with a scale of  $\ell$ . The turbulence viscosity is modelled by a Smagorinsky formulation, with a Smagorinsky constant  $C_s$  (Nieuwstadt et al., 2016).

$$\ell = C_s \Delta \quad (4.4)$$

where  $\Delta$  is the grid size. The subgrid stress  $\tau_{sgs}$  is given by

$$\tau_{sgs} = -\rho_0 ([u_i u_j] - [u_i][u_j]) \quad (4.5)$$

where  $[u_i]$  and  $[u_j]$  are the velocities of the filtered Navier-Stokes equations. Hence the eddy viscosity  $\nu_t$  is defined as

$$\nu_t = (C_s \Delta)^2 \left| \frac{\partial [u_i]}{\partial x_j} + \frac{\partial [u_j]}{\partial x_i} \right| \quad (4.6)$$

LES modelling should be used in combination with a grid discretization fine enough to resolve the eddies relevant for the flow problem.

The  $k - \varepsilon$  model uses two transport equations (Bahari and Hejazi, 2009) one for turbulent kinetic energy  $k$

$$\frac{\partial k}{\partial t} + u_i \frac{\partial k}{\partial x_i} = \frac{\partial}{\partial x_i} \left( \frac{\nu_t}{\sigma_k} \frac{\partial k}{\partial x_i} \right) + \mathcal{P} + G - \varepsilon \quad (4.7)$$

and one for turbulent dissipation  $\varepsilon$

$$\frac{\partial \varepsilon}{\partial t} + u_i \frac{\partial \varepsilon}{\partial x_i} = \frac{\partial}{\partial x_i} \left( \frac{\nu_t}{\sigma_\varepsilon} \frac{\partial \varepsilon}{\partial x_i} \right) + c_{1\varepsilon} \frac{\varepsilon}{k} (\mathcal{P} + G) (1 + c_{3\varepsilon} R_f) - c_{2\varepsilon} \frac{\varepsilon^2}{k} \quad (4.8)$$

here  $\mathcal{P}$  is the production of  $k$  by interaction of Reynolds stresses and mean-velocity gradient and  $G$  is the production and destruction of turbulence by buoyancy

$$\mathcal{P} = \nu_t \left( \frac{\partial u_i}{\partial x_j} + \frac{\partial u_j}{\partial x_i} \right) \frac{\partial u_i}{\partial x_j} \quad (4.9) \quad G = \beta g_i \frac{\nu_t}{\sigma_t} \frac{\partial \phi}{\partial x_i} \quad (4.10)$$

the quantities of  $k$  and  $\varepsilon$  are coupled to the eddy viscosity  $\nu_t$  by

$$\nu_t = c_\mu \frac{k^2}{\varepsilon} \quad (4.11)$$

$R_f$  is the flux Richardson number and  $g_i$  is the gravitational constant in  $x_i$  direction. The remaining parameters  $\beta$ ,  $c_\mu$ ,  $c_{1\varepsilon}$ ,  $c_{2\varepsilon}$  and  $c_{3\varepsilon}$  are empirical constants, of which more can be found in Bahari and Hejazi (2009).

### 4.1.3 Model outputs

The model returns values of concentration of the solved constituent, velocity and piezometric head for all elements on all the computed time steps.

## 4.2 Validation approach

The initial goal of this validation case was to validate the breaking of internal waves and the resulting mixing after breaking. Here the lab experiment from the study of Taylor (1992) is compared by a numerical simulation of this experiment by FinLab. The choice of this particular case is elaborated on based on earlier validation with FinLab.

Taylor (1992) quantifies the behaviour of wave breaking on microscale (overturning scale) and mesoscale (average quantities for the entire tank). It is too computationally challenging to reach a resolution high enough to observe the microscales in the numerical model outcomes. Invalid assumptions in the model for this application, make it impossible to validate for the mesoscales. The energy balance from the model results are not consistent, hence no useful values of the required parameters can be derived from this. Despite the fact that this validation case is not suitable for direct validation of mixing behaviour of breaking waves, other insights are obtained.

### 4.2.1 Earlier validation

In order to answer the research questions posed in Section 1.3 various physical processes have to be validated for the modelling tool FinLab:

1. Generation of internal waves over bottom topography;
2. Resonance conditions for internal waves;
3. Breaking of internal waves due to wave steepness;
4. Mixing as a result of breaking internal waves.

Pietrzak and Labeur (2004) has proven FinLab is able to adequately reproduce the linear behaviour under steady state conditions of internal waves. In this study non-breaking resonant internal waves show behaviour similar to analytical solutions of internal waves over undular topography. Also breaking internal waves over topography have been successfully simulated with FinLab by Van der Boon (2011). Here two cases were validated with lab

experiments. A two-layered fluid in a closed tank with a tilted interface and a sloping bottom. In this experiment the energy loss from internal solitary waves in the shoaling process and internal wave breaking behaviour is well reproduced. Secondly, a two-layered flow over a small bottom obstacle to generate solitons and lee waves according to theory.

The most important physical process yet to be validated is the mixing associated with breaking of internal waves. A lab experiment found most suitable for the validation of mixing efficiency of breaking internal waves is by Taylor (1992).

### 4.2.2 Experiment description and validation cases

Mixing efficiency induced by wave breaking is validated by modelling a lab experiment conducted by Taylor (1992), reproduced from McEwan (1983). Here internal waves are created with a moving wave paddle in a closed tank, with a flat bed. The tank is filled with a linearly stratified fluid. The surface is covered with polystyrene sheets to provide a rigid and non-diffusing upper surface. The created wave eventually reaches a point of breaking. Taylor (1992) found breaking events which started with ordered overturning structures, breaking down into smaller turbulent structures. The setup is shown in Figure 4.1.

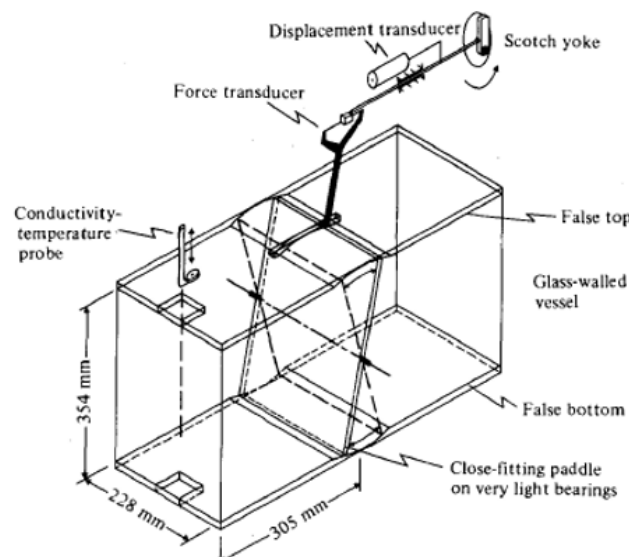


Figure 4.1: Experimental set-up from McEwan (1983), numerical simulations are based on the same set-up, however with dimensions of Taylor (1992)

- **Domain size (2D):** water column  $H = 530$  mm, length tank  $l = 2950$  mm;
- **Initial conditions:** linearly stratified fluid with  $N^2 = 0.2 \text{ s}^{-2}$  at mid-depth. For a water depth of 530 mm this corresponds to  $\Delta\rho = 10.8 \text{ kg/m}^3$ , hence  $\rho_{bottom} = 1000 \text{ kg/m}^3$  and  $\rho_{top} = 1010.8 \text{ kg/m}^3$ . In all runs the kinematic viscosity  $\nu = 10^{-6} \text{ m}^2/\text{s}$
- **Boundary conditions:** all sides are walls with a free slip condition.
- **Wave forcing:** by a paddle moving around an axis at mid-depth with an amplitude  $\alpha$  and forcing velocity  $a_n$  varying for different cases according to Table 4.1. The correlation between the two is given by  $a_n = -4\alpha\omega H/(\pi n)^2$ , where  $\omega$  is the forcing frequency and  $n$  the vertical mode number. The rotation of the wave paddle is modelled by  $\theta(t) = \alpha \cdot \sin(\omega t)$ .  
**Modelled cases:** Runs 1 to 3 had a forced mode structure of 2,1 (2 nodes in horizontal and 1 node in vertical) and runs 4 to 6 had a 3,1 structure. For the validation Run 2 and Run 4 are chosen to have one case of each wave structure.

## 4.3 Results of validation

First the general response of the model is shown. Then the energy balance is applied to the results.

### 4.3.1 Wave modes

Figures 4.2 and 4.3 show the resulting salinity and vertical velocity profiles of Run 2A and Run 4A. The frequency of the wave paddle forces a standing wave of a certain wave mode in the tank.

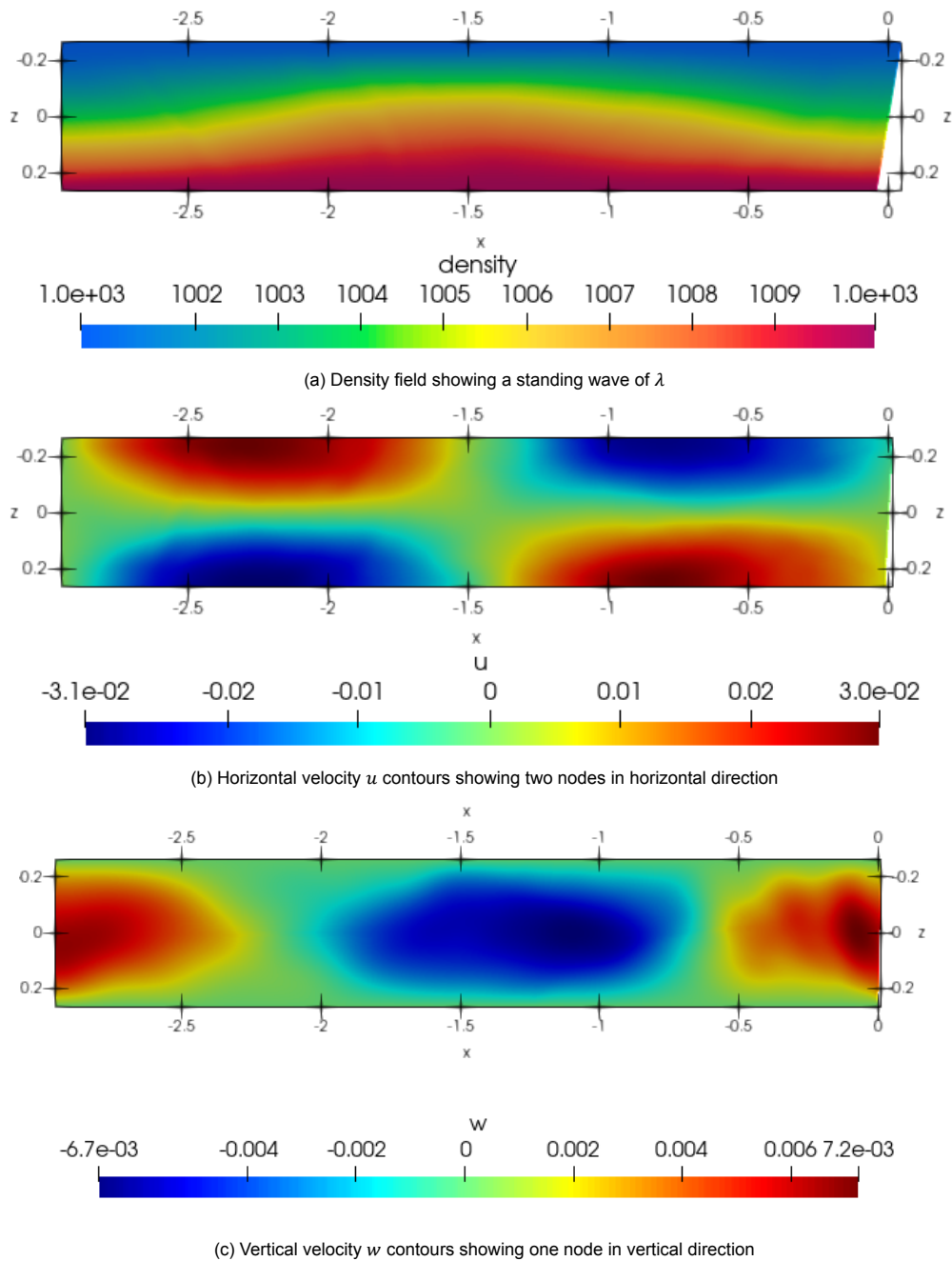


Figure 4.2: Run 2A: forced mode 2,1 structure

Figure 4.2 shows that Run 2 has a 2,1 structure (2 nodes in horizontal and 1 node in vertical). The horizontal velocity  $u$  in Figure 4.2b shows 2 nodes in horizontal direction and the vertical velocity  $w$  Figure 4.2c in shows one node in vertical direction.

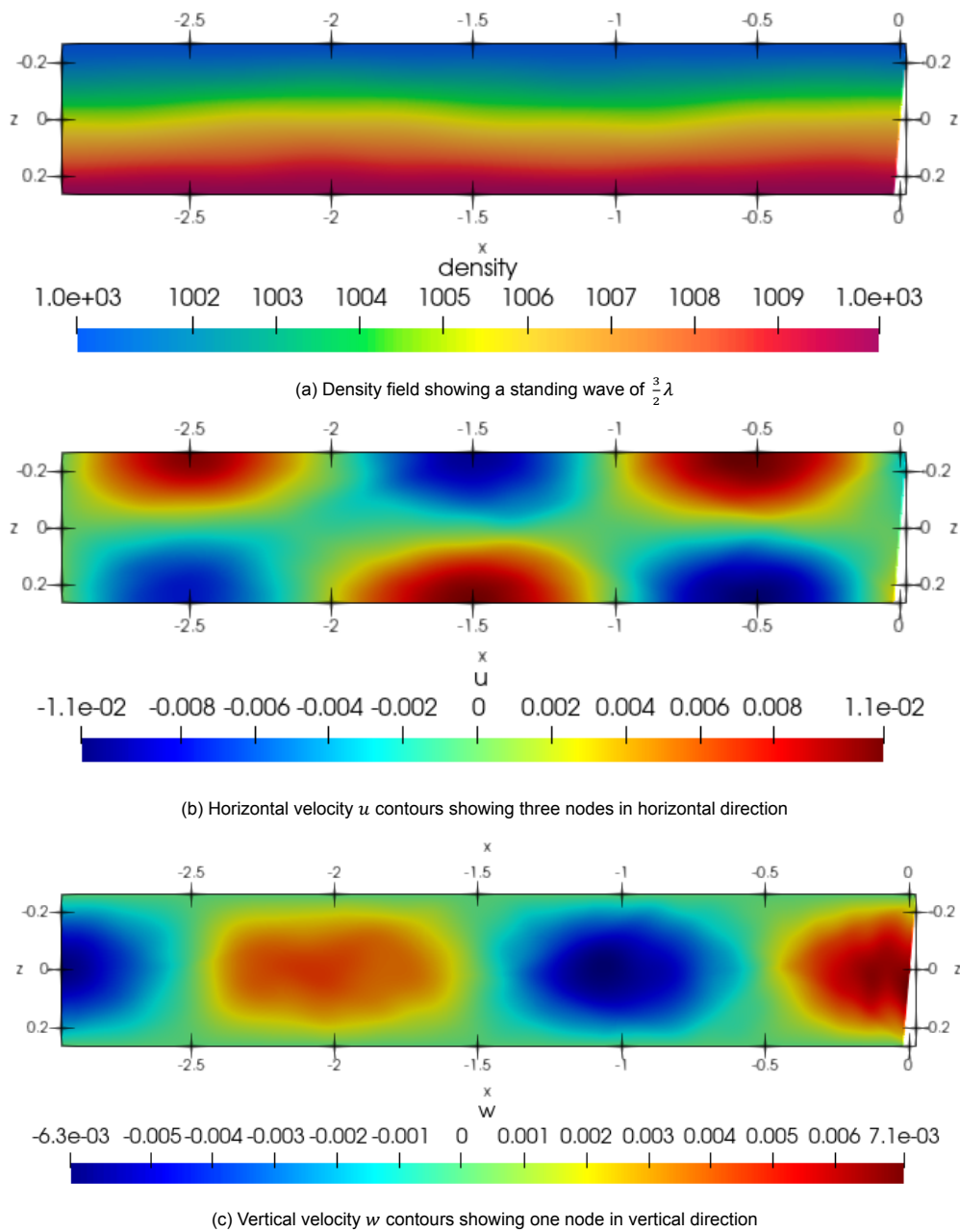


Figure 4.3: Run 4A: forced mode 3,1 structure

Figure 4.3 shows that Run 4 has a 3,1 structure (3 nodes in horizontal and 1 node in vertical). The horizontal velocity  $u$  in Figure 4.3b shows 3 nodes in horizontal direction and the vertical velocity  $w$  Figure 4.3c in shows one node in vertical direction. These wave structures in the model outcomes are in line with the wave structures found in the experiment.

Run nr	Forcing amplitude	Frequency	Resolution	Prandtl-Schmidt number	Turbulence model
	[rad]	[s <sup>-1</sup> ]	[-]	[-]	[-]
2A	0.174	-0.14	600x60	1	LES
2B	0.174	-0.14	600x60	100	LES
2C	0.174	-0.14	300x30	1	LES
2D	0.174	-0.14	1340x240	1	LES
2E	0.174	-0.14	600x60	1	$k - \varepsilon$
4A	0.102	-0.22	600x60	1	LES

Table 4.1: Validation runs

### 4.3.2 Energy balance

Through formulations of energy the internal wave energy can be linked to the amount of mixing by means of a mixing efficiency, therefore an energy balance is considered. Energy is computed as the bulk energy over time. Bulk energy is the sum of the total energy in the tank. The energy balance in the tank is described as follows

$$\frac{dE_{tot}}{dt} = \frac{d(E_p + E_k)}{dt} = W - \varepsilon - g\kappa \frac{\partial \Delta \rho}{\partial z} \quad (4.12)$$

where the total energy in the tank  $E_{tot}$  consists of potential energy  $E_p$  and kinetic energy  $E_k$  and  $\varepsilon$  is viscous dissipation. The work delivered by the wave maker  $W$  is described by

$$W = \int P(t) dt \quad (4.13)$$

where  $P$  is the power delivered by the wave maker over time, this is calculated by integrating the power normal to the moving wave paddle over the length of the wave paddle

$$P(t) = \int_{\text{boundary}} \vec{u} \cdot \vec{n} \rho g h dz \quad (4.14)$$

where  $\vec{u}$  is the velocity vector,  $\vec{n}$  is the normal vector and  $h$  is piezometric head on the wave paddle. Those parameters are all calculated in the model.

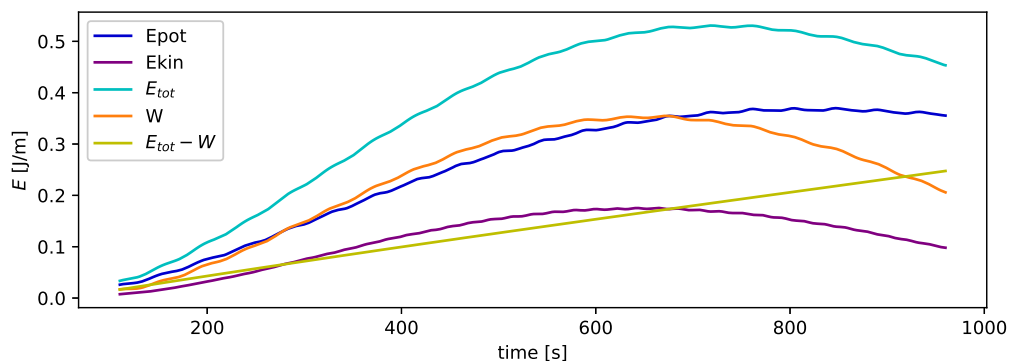
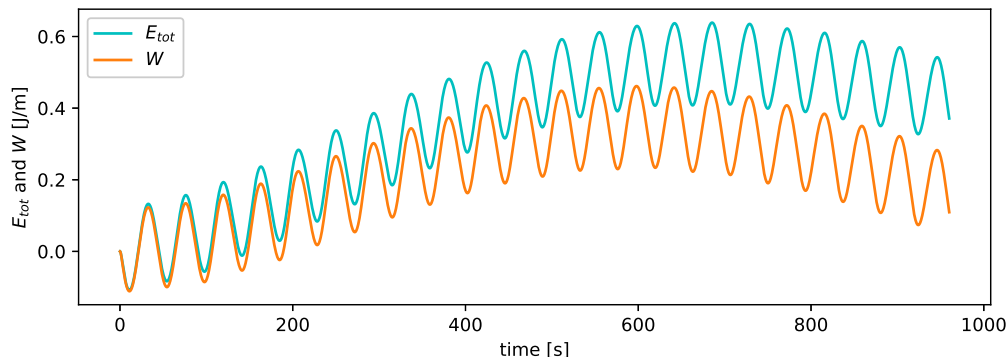


Figure 4.4: Mean values of energy Run 2A (600x60), showing that the difference between the total energy  $E_{tot}$  and work by the wave maker  $W$  increase linearly in time. Here  $\sigma = 1$  and  $\nu = 10^{-6} \text{ m}^2/\text{s}$

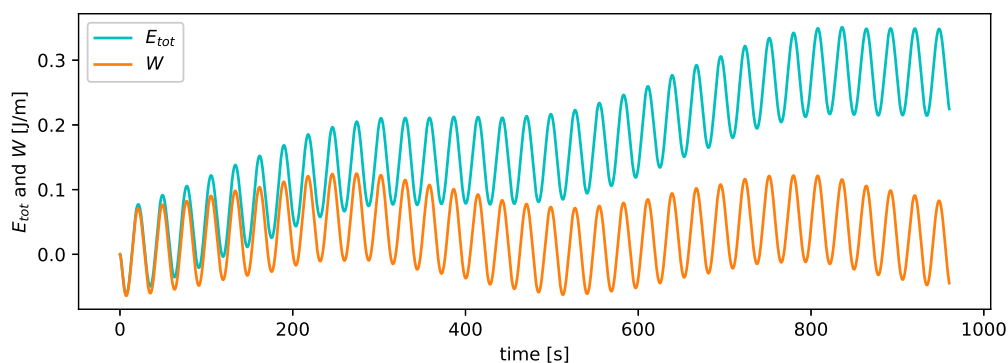
For both Run 2 and Run 4 Figures 4.4 and 4.5 show that  $E_{tot}$  is larger than  $W$ , which means that the energy content in the tank increases at a higher rate than the energy input provided by the wave maker. This is not in

line with the law of conservation of energy.

As can be seen in Figure 4.9 the difference between  $E_{tot}$  and  $W$  decreases with an increasing grid resolution, hence decreasing numerical diffusion. However, there is still a significant difference. Based on the grid size (0.2 - 0.9 mm) and the observed velocities ( $O(\text{mm/s})$ ) the numerical diffusion is expected in order  $O(\Delta x \cdot u) = O(10^{-7} - 10^{-5} \text{ m}^2/\text{s})$ . The observed diffusion is about an order magnitude larger, so it cannot merely be related to numerical diffusion.



(a) Run 2A: forced mode 2,1 structure



(b) Run 4A: forced mode 3,1 structure

Figure 4.5: Total energy  $E_{tot}$  and work of the wave maker  $W$  over time shows that the total energy in the tank becomes larger than the input delivered by the wave maker. Simulations with medium resolution (600x60),  $\sigma = 1$  and  $\nu = 10^{-6} \text{ m}^2/\text{s}$

To further analyse the consistency in the energy balance only Run 2 will be considered, because both cases show similar behaviour. Another remarkable observation is that the difference between  $E_{tot}$  and  $W$  is merely seen in the mean of the energy, the amplitude of the oscillations  $E_{tot,w}$  and  $W_w$  are exactly the same (see Figure 4.6). Plotting the means over time (Figure 4.4) shows that the difference between  $E_{tot}$  and  $W$  increases linearly in time. From this we can conclude a truncation error is not causing this divergence. Additionally, Figure 4.4 shows that the total energy increase is mainly caused by the increase in potential energy.

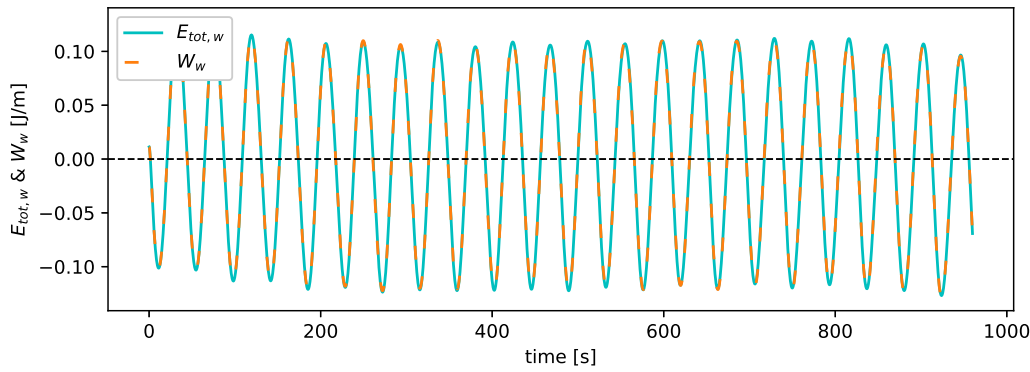


Figure 4.6: Fluctuation total energy and work wave maker. Amplitude of total energy and work wave maker Run 2A (600x60),  $\sigma = 1$ ,  $\nu = 10^{-6} \text{ m}^2/\text{s}$

### 4.3.3 Diffusion of salt

The large increase of the total energy is mainly caused by the diffusion of salt. This can be directly derived from the energy equations implemented in FinLab. Additional variations on Run 2 confirm that this energy increase imposed by the model is dominant over numerical diffusion. Those variations are the amount imposed diffusion and the grid resolution.

#### Energy equations

The energy balance is rewritten to find an expression for the change of total energy in the tank over time  $\frac{dE_{tot}}{dt}$ . A full derivation can be found in Appendix E.

$$\frac{d}{dt} \int_{\text{domain}} (E_{tot}) dx = - \int_{\text{domain}} \mu |\nabla \vec{u}|^2 dx - \int_{\text{domain}} g\kappa \frac{\partial \Delta \rho}{\partial z} dx + \int_{\text{domain}} W dx \quad (4.15)$$

The viscous term of Equation 4.15 is always negative. For a stable stratification the density gradient  $\frac{\partial \Delta \rho}{\partial z}$  is always negative, which makes the diffusion term of Equation 4.15 positive. The diffusion of salt can cause an energy increase.

For small values of  $u$  the viscous term is negligible, the change of total energy in the tank reduces to

$$\frac{dE_{tot}}{dt} = \kappa g L (\Delta \rho_{bottom} - \Delta \rho_{top}) \quad (4.16)$$

The amount of diffusion coincides with the numbers found in the numerical results. This is found by solving Equation 4.15 for  $\kappa$ . This shows that the model outcome is consistent with the energy balance derived from the equations resolved in the model (Equations (4.1) to (4.3)). A limitation of the parameterization of mixing is causing the energy in the tank  $E_{tot}$  to exceed the energy input  $W$ , not a numerical defect.

The value of  $\frac{dE}{dt}$  can be estimated from the average increase in energy for the linear regime of  $E_{tot}$ . This is done for a case with  $\sigma = 1$  and  $\sigma = 100$  (Figures 4.4 and 4.8b). The diffusion  $\kappa$  is of the same order as the diffusion imposed by the model.

This means the energy balance equations in FinLab are consistent, and the results are not caused by a numerical artefact. From this can be concluded that at the scale of this experiment the parameterization of mixing is not adequate.

#### Effect of diffusivity

Reducing the diffusivity of dissolved constituent (only salt in this model)  $\kappa$ , is expected to decrease the difference between  $E_{tot}$  and  $W$ . Assuming that this difference is indeed caused by the diffusion of salt.

In the model diffusivity is imposed by the Prandtl-Schmidt number  $\sigma$ . This dimensionless number gives the ratio between eddy viscosity  $\nu_t$  and eddy diffusivity  $\kappa_t$  according to Equation 4.17.

$$\sigma = \frac{\nu_t}{\kappa_t} \tag{4.17}$$

Figure 4.8 shows that the difference between  $E_{tot}$  and  $W$  vanishes for  $\sigma = 100$ . The difference between  $E_{tot}$  and  $W$ , plotted by the yellow line in Figure 4.8b, is almost zero and stays constant in time. A higher value of sigma and hence a lower value for diffusivity  $\kappa$  gives a smaller difference between  $E_{tot}$  and  $W$ , see Figure 4.7. The other way around smaller values for sigma ( $\sigma > 1$ ) give a larger difference between the two.

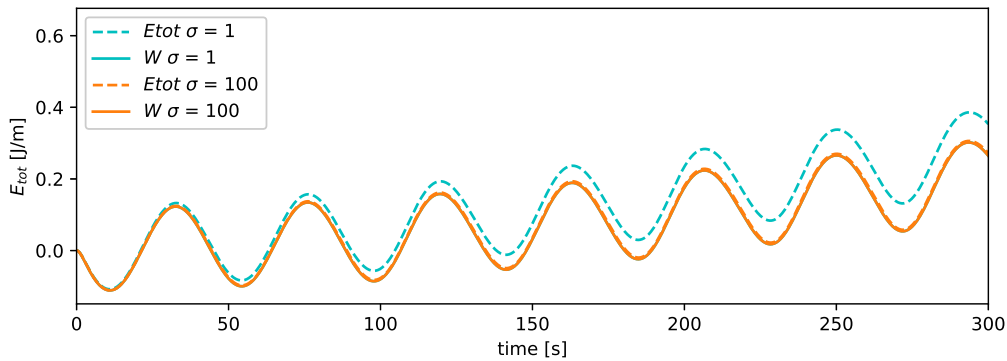
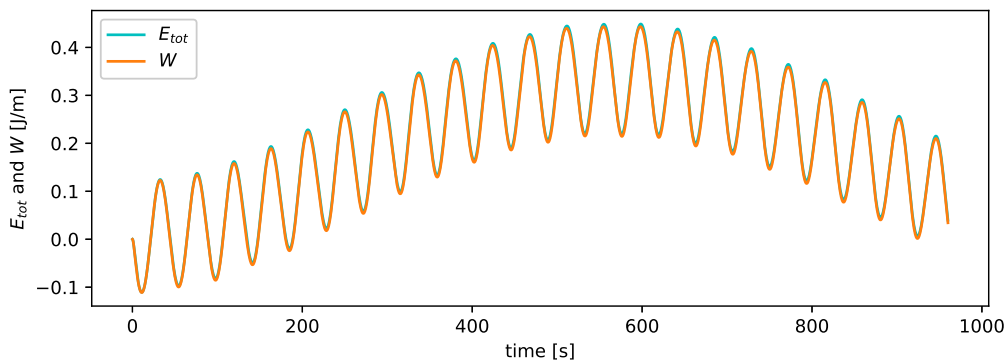
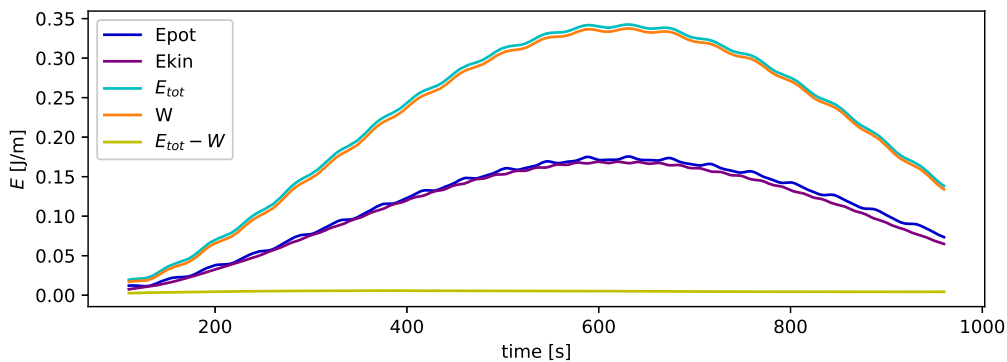


Figure 4.7: Effect of different Prandtl-Schmidt number  $\sigma$ . Total energy and work wave maker Run 2A and Run 2B showing the difference between  $\sigma = 1$  and  $\sigma = 100$ . Here  $\nu = 10^{-6} \text{ m}^2/\text{s}$



(a) Total energy  $E_{tot}$  and work wave maker  $W$



(b) Mean values of bulk energy

Figure 4.8: Run 2B (600x60) for a low amount of diffusion, here  $\sigma = 100$  and  $\nu = 10^{-6} \text{ m}^2/\text{s}$

### Effect of numerical diffusion

A simulation with a higher grid resolution will result into less numerical diffusion. Figure 4.9 shows that an increase in resolution from 300x30 to 600x60 there is a smaller error of overestimation of the total energy in the tank. However, if the resolution is further increased to 1340x240 this overestimation stays the same, hence it cannot be linked to numerical diffusion.

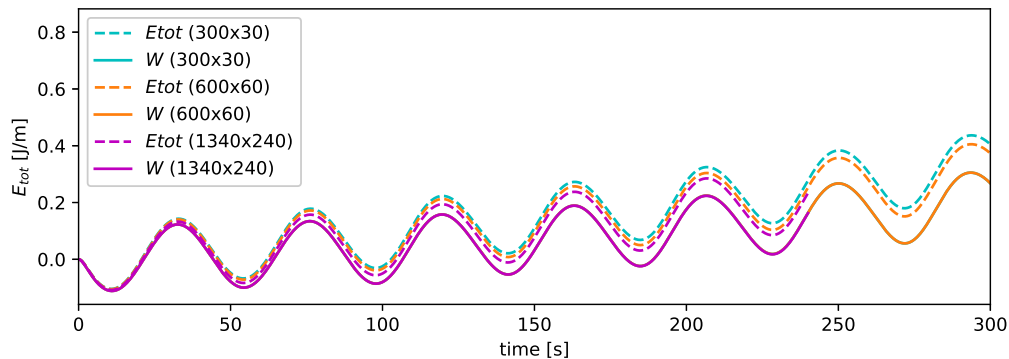
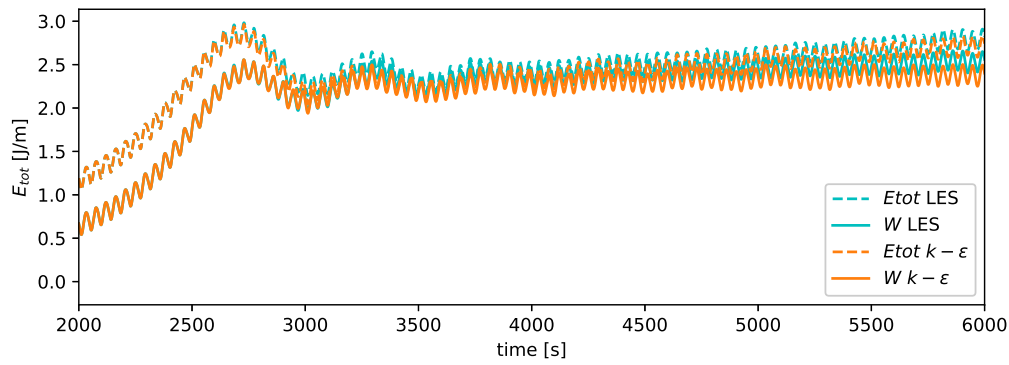


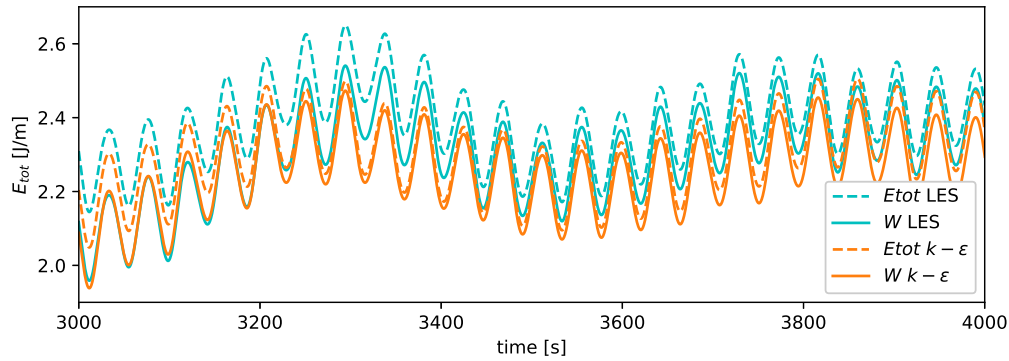
Figure 4.9: Difference in grid resolution. Total energy  $E_{tot}$  and work wave maker  $W$  showing the difference for a low (300x30, Run 2C), medium (600x60, Run 2A) and extra fine (1340x240, Run 2D) grid. Here  $\sigma = 1$  and  $\nu = 10^{-6} \text{ m}^2/\text{s}$

### 4.3.4 Turbulence model and breaking

Simulations with two different turbulence models give different results for wave breaking. The turbulence closure models  $k-\varepsilon$  and LES are compared for this simulation. Section 4.1.2 explains more about the difference of those models. The main observation from Figure 4.10 is that the total bulk energy  $E_{tot}$  computed by both models give the same outcomes till a certain point. From change of the potential energy can be seen that the point where the model outcomes start diverging is the point where wave breaking starts.



(a) Time interval 2000 to 6000 seconds



(b) Time interval 2000 to 6000 seconds gives a more detailed view of the different results when wave breaking has started

Figure 4.10: Difference between turbulence models showing total energy  $E_{tot}$  and work  $W$  wave maker Run 2A for LES and Run 2E  $k-\epsilon$  model. Here  $\sigma = 1$  and  $\nu = 10^{-6} \text{ m}^2/\text{s}$

This shows the relevance of a good choice of a turbulence model when dealing with breaking waves. With turbulence measurements of breaking waves from experiments can be validated which turbulence model fits this application best.

## 4.4 Discussion of the model

The wave tank experiment shows an inconsistency in the energy balance caused by a physically impossible amount of salt diffusion. The excess amount of diffusion is not caused by numerical artefacts, but by the effects of the small scale of the modelling case. This section puts these findings in a larger perspective and explains what implications the physical shortcomings of FinLab have on the modelling cases on the scale of the RWW.

### 4.4.1 Ratio between dissipation and diffusion

In the incompressible Navier-Stokes equations, implemented in FinLab, the rate of change in energy is determined by a viscous dissipation term and a diffusion term (Equation 4.15). For the conservation of energy these terms should be balanced as follows

$$-g\kappa \frac{\partial \Delta \rho}{\partial z} - \mu |\nabla u|^2 < 0 \quad (4.18)$$

The ratio of these terms is analogous to the Richardson number (Equation 2.15) by

$$1 < Ri \cdot \frac{\kappa}{\nu} = Ri \cdot \frac{1}{\sigma} \quad (4.19)$$

Hence

$$Ri < \frac{\nu}{\kappa} \quad (4.20)$$

In this case Equation 4.20 implies that for values of  $Ri > 1$  the Prandtl-Schmidt number cannot be assumed the value of 1, because  $\nu > \kappa$ .

Schönfeld and Kranenburg (1977) describes that for high Richardson numbers the diffusive transport is hindered more than turbulent transport. Which implies lower values of  $\kappa$  than  $\nu$ . In this case is assumed that there is a balance between the turbulence produced by shear stress and upward mass transport. Here the turbulent kinetic energy that could be transported from elsewhere by turbulence is neglected (Schönfeld and Kranenburg, 1977).

With these assumptions you can rewrite the expression of Equation 4.20 as a mixing efficiency  $\eta$

$$\eta = \frac{Ri}{\sigma} \quad (4.21)$$

The definition of a mixing efficiency is that the inequality should hold

$$\eta < 1 \quad (4.22)$$

This definition of  $\eta$  can be used as a starting point for a subgrid mixing efficiency. This is especially relevant if a significant part of the unresolved turbulent scales are responsible for mixing. This could be implemented by means of a subgrid closure, similar to closures used for LES. A limiting factor would be that this mixing efficiency should be estimated on forehand. For example by means of measurements.

#### 4.4.2 Relation to RWW model

In most modelling cases the assumption is made that  $\sigma = 1$ . With the assumptions made in the wave tank this only holds for  $Ri < 1$ . To put this into perspective the Richardson number is estimated for the wave tank and the RWW.

Tank:

$$Ri = -\frac{10}{1000} \frac{\frac{10}{5 \cdot 10^{-1}}}{\left(\frac{2 \cdot 6 \cdot 10^{-2}}{5 \cdot 10^{-1}}\right)^2} = 100 - 2000 \quad (4.23)$$

RWW:

$$Ri = -\frac{10}{1000} \frac{\frac{15}{15}}{\left(\frac{1}{15}\right)^2} = 1 - 10 \quad (4.24)$$

This gives  $Ri \sim 100 - 2000$  for the wave tank and  $Ri \sim 1 - 10$  for the RWW. According to Equation 4.21 and the assumption that  $\sigma = 1$ , leads to  $\eta$  being larger than one for both the wave tank and the RWW. This implies the efficiency is higher than one which is physically impossible.

An efficiency higher than one was indeed observed in the wave tank, causing an increase in energy in the system. As mentioned before this balance for the efficiency only holds in regions where there is no supply of TKE from other regions. Close enough to the bed there is a constant supply of TKE, which increases the viscous dissipation. In the RWW there is a constant flow (tidal and river) over a bed with friction.

Therefore, in the case of the RWW the salt diffusion term is expected to be balanced by the viscous dissipation term. In many engineering applications there will also be enough forcing in the system to generate transport of TKE. However from this modelling study can be learned that simulations with the incompressible Navier-Stokes equations and high Richardson numbers the value of the Prandtl-Schmidt number should be carefully chosen.

## 4.5 Conclusions validation

A lab experiment in a tank with a moving wave paddle is reproduced, for validation of wave breaking and mixing behaviour in FinLab. Reaching a resolution fine enough to observe microstructures is too computationally challenging, which makes it impossible to compute parameters on overturning scales according to Taylor (1992). Therefore validation is based on bulk parameters.

The bulk parameters show that the total energy in the tank increases at a higher rate than the work delivered by the wave paddle; the energy input. This is the effect of an inadequate parameterization of mixing. Rewriting the equations of motion to an expression for the change in total energy in the tank shows that the observed effect is caused by the diffusion of salt. Additional observations further confirm this. An increase in the Prandtl-Schmidt number  $\sigma$  (and thereby decreasing the diffusion) of the model, reduces (and eventually eliminates) the overestimation of the total energy in the tank. An increase in the grid resolution and hence a decrease in numerical diffusion, reduces the overestimation of diffusion. However, a resolution finer than 60x600 does not further decrease the overestimation of diffusion. From this can be concluded that numerical diffusion plays a negligible role at this scale.

For any future applications of models with a similar parameterization for mixing the above conclusions have to be considered. The parameterization currently implemented in FinLab is a Smagorinsky turbulence closure, where the diffusion is related to the eddy viscosity  $\nu_t$  by a constant Prandtl-Schmidt number. The value of the eddy viscosity is based on the velocity shear, where the density effects are not taken into account. This parameterization is not suitable for similar problems. From Equation 4.15 can be seen that relatively small velocity gradients in combination with a large stratification gradient cause a similar regime as found in this experiment. The Richardson number gives an indication of the ratio between these terms.

Due to the unrealistic results this model has not yet been validated for the breaking and subsequent mixing behaviour. For any future validation cases the consideration has to be made how well the mixing behaviour is parameterized for the used application. When cases with high Richardson numbers  $Ri \sim O(10^2 - 10^3)$  or higher are modelled with a similar mixing parameterization, the value of the Prandtl-Schmidt number has to be carefully determined.

## Numerical study: Parameter study

The parameter study investigates the effect of applying sinusoidal bottom topography in a stratified channel on internal wave generation and vertical mixing. First the general flow behaviour is investigated for stratified flow over sinusoidal bed waves, this is compared to reference case without bed waves. Physical aspects of mixing are investigated, where the sensitivity of bed friction on internal wave generation and mixing is further elaborated on. Finally the effect of variation in bed wave parameters is investigated.

### 5.1 Method

#### 5.1.1 Cases and set-up

All cases in this study are based on the Rotterdam Waterway (RWW), values of the parameters are considered according to values commonly found in the RWW (see Section 3.2 and Appendix A for motivation of the parameters). A channel stretch is modelled according to a base case, after which a single parameter is varied for the subsequent other cases. The domain is a 2D stretch of a stratified channel with sinusoidal bed waves. The channel has a length of 1,600 m with an average water depth of 15 m. The base case has a linearly stratified fluid ranging, a background flow  $U_0$  linearly increasing in time and sinusoidal bed wave topography in the middle of the domain between  $x = -X$  and  $x = X$  m (see Figures 3.3 and 5.1).

The parameters of the base case (*L50h050*) are given in Table 5.1, variations on this case are made according to Table 5.2. In addition the sensitivity to bed friction is studied to explain the model results better. Other model settings can be found in Appendix D.

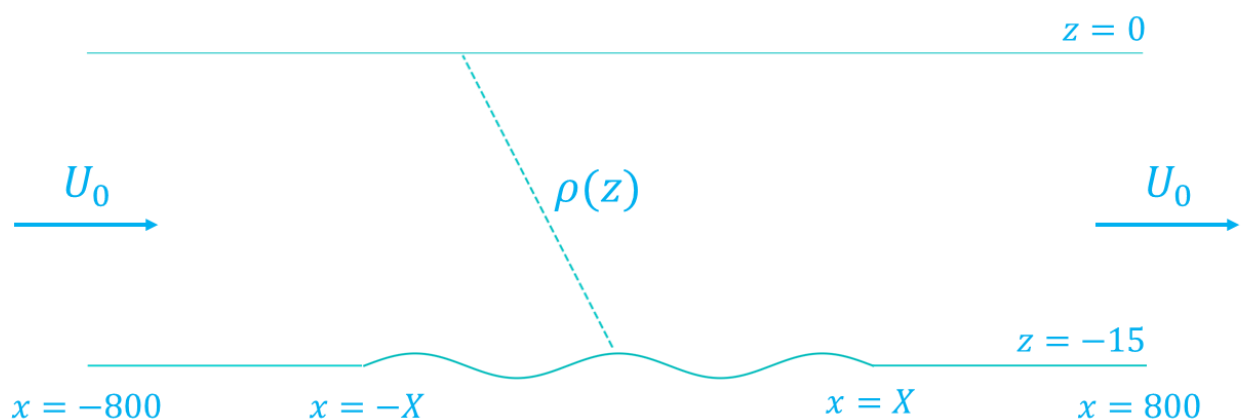


Figure 5.1: Domain of the modelling cases. Sinusoidal bottom topography is located between  $x = -X$  and  $x = X$  m.

The density profile in the RWW is usually a hyperbolic tangent structure (Figure A.1), a mix between a two-layer profile and a linearly stratified profile. In the simulations the latter simplification is chosen, since this is a main assumption of the analytical approach. The background flow velocity increases linearly in time. Here influence of changing background velocity on the emerging modes is visible, without adding tidal effects of increasing and decreasing velocities, acceleration and deceleration or flow reversal.

Parameter	Dimension	Unit
Channel length	1,600	m
Channel depth $H$	15	m
Background flow velocity $U_0$	0.0-1.0	m/s
Bed friction $k_n$	$2 \cdot 10^{-2}$	m
Stratification	linearly stratified	
Density surface $\rho_{\text{surface}}$	1000	kg/m <sup>3</sup>
Density bottom $\rho_{\text{bottom}}$	1015	kg/m <sup>3</sup>
BW length $L_\tau$	50	m
BW amplitude $h_0$	0.5	m
BW domain boundary $X$	275	m

Table 5.1: Parameters of the base case  $L50h050$

### Boundary conditions and initial conditions

The following conditions are used for the upper and lower boundaries:

- Wall boundary. Friction is imposed with a Nikuradse roughness of  $k_n = 2 \cdot 10^{-2}$  m, based on a sandy river bed;
- Symmetrical boundary (free slip). This is used as upper boundary condition. This study focuses on behaviour of internal waves, and therefore the presence of surface waves is neglected ( $\eta_{\text{surface}} = 0$ ). One case ( $kn_0$ ) uses a symmetrical boundary at the bottom, to have a completely frictionless case.

Both side boundaries are velocity boundaries. In stratified flows the piezometric level can fluctuate due to changing density distribution. Therefore, a combination of an inflow boundary (left boundary) and an outflow boundary (right boundary) is most appropriate to use.

The channel initially has a linear density profile over depth  $\rho(z)$ , where the surface is located at  $z = 0$ . This profile can be expressed as function of the vertical  $z$ -coordinate for a water depth of  $H$  according to

$$\rho(z) = \rho_{\text{surface}} - (\rho_{\text{bottom}} - \rho_{\text{surface}}) \frac{z}{H} \quad (5.1)$$

The inflow also has the same density distribution  $\rho(z)$  as the initial conditions.

### Parameter variations

Variations in parameters are considered to see the effect on the generated internal wave energy and the amount of vertical mixing. The considered parameters are further highlighted below.

The following parameters of the bottom topography are varied:

1. **bottom topography wavelength:** bottom topography wavelength is one of the major parameters of influence for the resonance conditions. (Section 3.4.)
2. **bottom topography wave amplitude:** the bottom topography amplitude is of influence of the internal wave amplitude. According to linear theory bottom topography amplitude has a linear relation with the internal wave amplitude, and hence a quadratic relation with internal wave energy (see Section 3.4).

The following parameter is varied to investigate the sensitivity:

- 3 **bottom friction:** increased bottom friction can cause increased bed shear stresses which can result in shear instabilities. On the other hand increased bottom friction also increases dissipation of (internal wave) energy.

Table 5.2 gives an overview of all the runs of the parameter study. Besides the above variations in bed wave forms, there are two reference cases. One without bed waves and one with bed waves and without stratification. The influence of friction is studied by varying  $k_n$ . Additionally all cases have a corresponding case without bed waves, indicated with *\_nbw*.

Case nr	Density gradient $\Delta\rho/H$	BW length $L_\tau$	BW amplitude $h_0$	BW domain $X$	Bed roughness $k_n$
[-]	[kg/m <sup>3</sup> ]	[m]	[m]	[m]	[m]
<i>L50h050</i>	15	50	0.50	275	$2 \cdot 10^{-2}$
<i>ref_nbw</i>	15	-	-	-	$2 \cdot 10^{-2}$
<i>ref_barotrop</i>	0	50	0.50	275	$2 \cdot 10^{-2}$
<i>L20h050</i>	15	20	0.50	260	$2 \cdot 10^{-2}$
<i>L30h050</i>	15	30	0.50	255	$2 \cdot 10^{-2}$
<i>L40h050</i>	15	40	0.50	260	$2 \cdot 10^{-2}$
<i>L60h050</i>	15	60	0.50	279	$2 \cdot 10^{-2}$
<i>L70h050</i>	15	70	0.50	280	$2 \cdot 10^{-2}$
<i>L50h050</i>	15	50	0.50	275	$2 \cdot 10^{-2}$
<i>L50h020</i>	15	50	0.25	275	$2 \cdot 10^{-2}$
<i>L50h070</i>	15	50	0.75	275	$2 \cdot 10^{-2}$
<i>L50h100</i>	15	50	1.00	275	$2 \cdot 10^{-2}$
<i>L50h150</i>	15	50	1.50	275	$2 \cdot 10^{-2}$
<i>kn_0002</i>	15	50	0.50	275	$2 \cdot 10^{-3}$
<i>kn_02</i>	15	50	0.50	275	$2 \cdot 10^{-1}$
<i>kn_0</i>	15	50	0.50	275	0
<i>kn_0002_nbw</i>	15	-	-	-	$2 \cdot 10^{-3}$
<i>kn_02_nbw</i>	15	-	-	-	$2 \cdot 10^{-1}$
<i>kn_0_nbw</i>	15	-	-	-	0

Table 5.2: Cases parameter study

### 5.1.2 Methods of evaluation

The goal of the simulations is to investigate the generated internal waves and their energy content. Secondly, to see what the effect of those internal waves is on the amount of vertical mixing. Lastly is analysed what processes drive vertical mixing and what the effectiveness of mixing is. This will be compared for the different bed wave form configurations.

To compare model outcomes the average energy integrated over the 2D domain of the bed waves (between  $x = -X$  m and  $x = X$  m) is considered as a function of time.

#### Quantities of energy

**Kinetic energy** as a result of vertical velocity is computed to analyse wave energy as a function of time. This kinetic energy  $E_{k,z}$  is a function of only vertical velocity  $w$ . This quantity is averaged over the bed wave domain  $\overline{E_{k,z}}$  is given by

$$\overline{E_{k,z}}(t) = \frac{1}{2X \cdot H} \int_{-H}^0 \int_{-X}^X \frac{1}{2} \rho_0 w^2(x, z, t) dx dz \quad (5.2)$$

The total spatially averaged potential energy and kinetic energy are parameters which are influenced by more processes than internal waves. Total kinetic energy is governed by horizontal background flow. Spatially averaged potential energy is expected to filter out the internal wave fluctuations. Therefore kinetic energy as function of vertical velocity is chosen to give an indication of the presence of internal wave energy. Note that this is not the total amount of wave energy, however it qualitatively describes when high amounts of wave energy are present. Quantitatively it gives an indication of the order magnitude of the internal wave energy. In the remain of this chapter  $E_{k,z}$  will be simply referred to as kinetic energy.

**Potential energy** of the bed wave domain is computed to analyse vertical mixing. The amount of mixing can be derived from the change in potential energy as a results of density distribution over depth. Therefore potential energy is defined with respect to a reference density of  $\rho_0 = 1000 \text{ kg/m}^3$ . The domain averaged potential energy  $\overline{E_p}(t)$  is defined according to

$$\overline{E_p}(t) = \frac{1}{2X \cdot H} \int_{-H}^0 \int_{-X}^X \Delta\rho(x, z, t) g z dx dz \quad (5.3)$$

Here  $\Delta\rho$  is the density difference with respect to the reference density  $\Delta\rho = \rho_b(z) + \rho_w(x, z, t) - \rho_0$  (see Equation 2.14). Also the **change in total potential energy**  $\frac{d\overline{E_p}}{dt}$  is derived by time integration of Equation 5.3 This change in total density can be compared to the vertical fluxes.

Alternatively mixing can be indicated by the change in potential energy due to vertical fluxes. The **vertical buoyancy flux** averaged over the total volume of the bed wave domain  $b$  is given by

$$b = \frac{1}{2X \cdot H} \int_{-H}^0 \int_{-X}^X \left( \Delta\rho(x, z, t) g w(x, z, t) - \kappa g \frac{\partial \Delta\rho}{\partial z} \right) dx dz \quad (5.4)$$

This gives the change in potential energy merely due to vertical mixing.

## 5.2 General response

First the general response of the base case *L50h050* with a bottom topography with  $L_\tau = 50 \text{ m}$  and  $h_0 = 0.5 \text{ m}$  is discussed. Simulation results show a clear generation of the first two internal wave modes of internal waves trapped to the bottom topography. Mode 1 (Figure 5.2) has its isopycnals in phase with the bottom topography, which is visible in the density field of Figure 5.2a. Mode 2, generated at another background flow velocity, is shown in Figure 5.3. In a mode 2 structure, the lower half of the water column has isopycnals in phase with the bottom topography and the upper half of the water column has isopycnals out of phase with the bottom topography (see Figure 5.3a). The mode structures also have a specific structure of vertical velocity  $w$ . Mode 1 has half a wavelength over the vertical, which means that either upward or downward velocities are present over one vertical (Figure 5.2b). Mode 2 has a full wavelength over the vertical, which implies both upward and downward velocities over the vertical (Figure 5.3b).

For this specific case, resonance of the first two modes is expected to occur at background velocities  $U_0$  of 0.41 and 0.23 m/s according to frictionless linear theory (see Figure B.4 in Appendix B). In the simulation these are the velocities imposed at the boundaries at  $t = 150$  minutes and  $t = 80$  minutes. Trapped internal waves with mode structures of 1 and 2 (shown in Figures 5.2 and 5.3) are generated around  $t = 180$  minutes ( $U_0 = 0.50 \text{ m/s}$ ) and  $t = 100$  minutes ( $U_0 = 0.28 \text{ m/s}$ ) respectively.

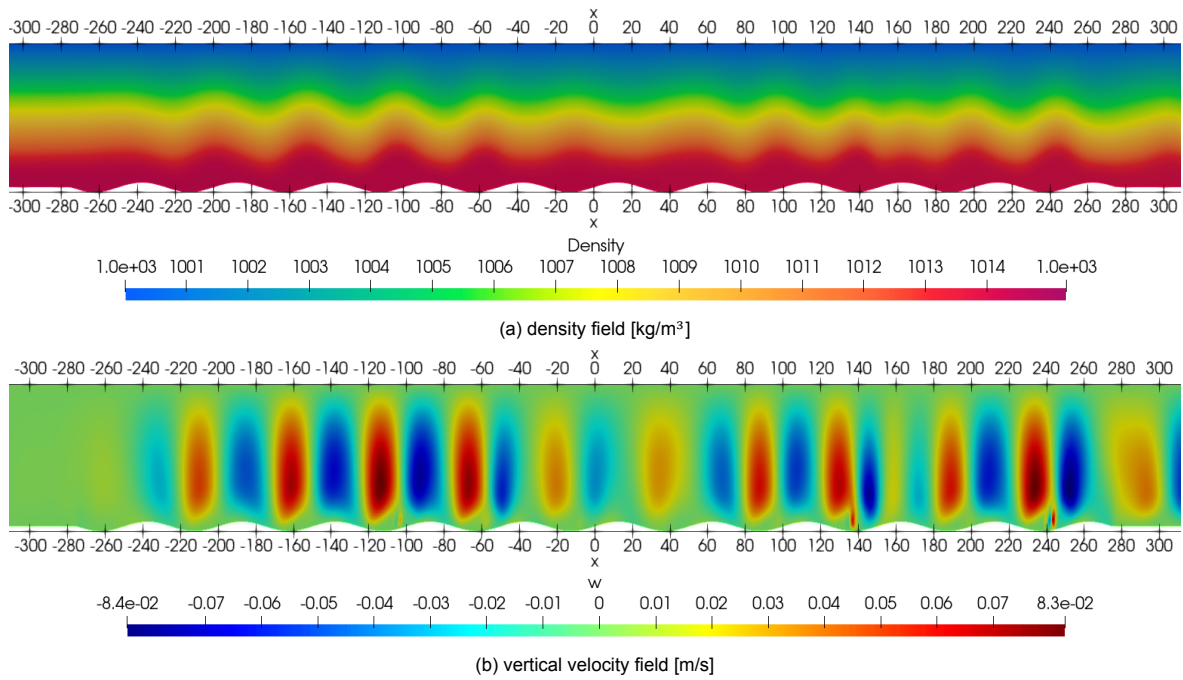


Figure 5.2: Mode 1 structure where the internal wave is trapped to the bottom topography at  $t = 180$  minutes when  $U_0 = 0.50$  m/s for case *L50h050*

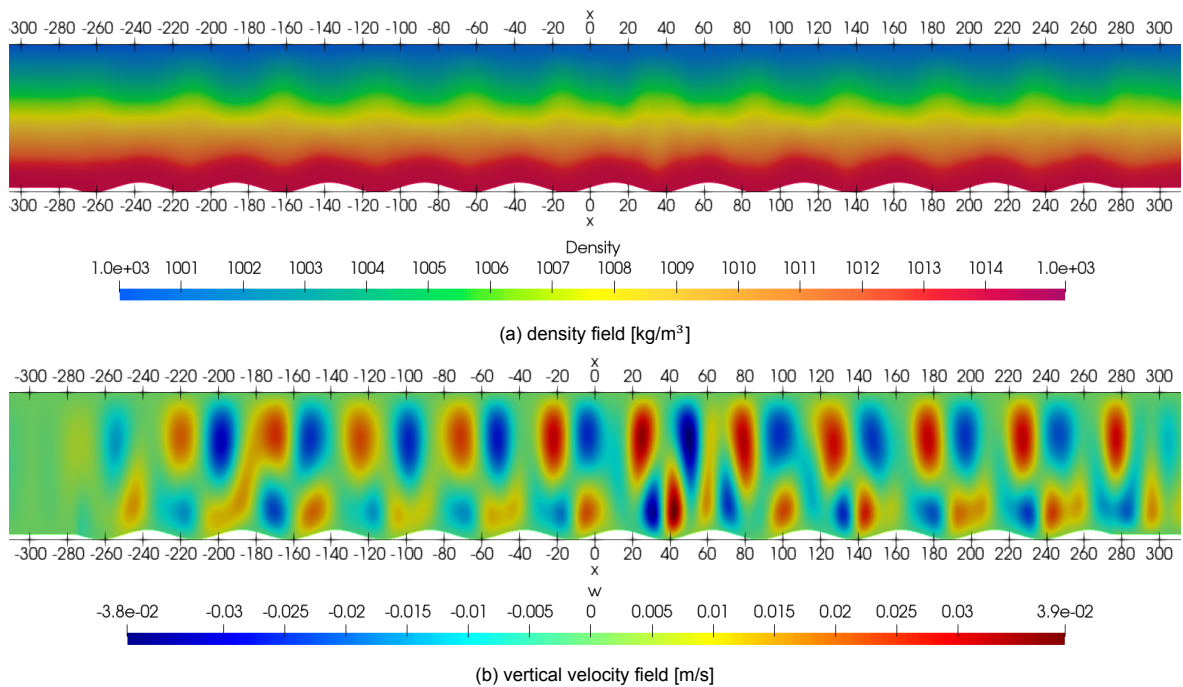


Figure 5.3: Mode 2 structure where the internal wave is trapped to the bottom topography at  $t = 100$  minutes when  $U_0 = 0.28$  m/s for case *L50h050*

The kinetic energy as function of vertical velocity  $E_{k,z}$  gives an indication of the internal wave action. The average vertical density flux  $b$  (Equation 5.4) gives an indication of vertical mixing. Both quantities are plotted as function of time in Figure 5.4. During presence of internal waves the kinetic energy and the buoyancy flux seem correlated. During occurrences of internal waves  $b$  is negative, which means a downward flux. An upward flux is observed without wave action and is therefore not directly caused by internal waves. The domain-averaged kinetic energy as function of vertical velocity  $\overline{E_{k,z}}$  is relatively small compared to the potential energy anomaly (PEA), the amount of energy required to fully mix the stratified water column. Due to the presence of upward and downward fluxes

over time, the net (time integrated) vertical buoyancy flux over the simulation time is small compared to the absolute buoyancy flux. The net (time integrated) vertical buoyancy flux over the 360 minutes simulation is only  $0.61 \text{ J/m}^3$ , while the absolute flux is  $8.56 \text{ J/m}^3$ . Another comparison to put  $b$  into perspective; to reach a total PEA of  $184 \text{ J/m}^3$  an average buoyancy flux of about  $0.5 \text{ J/s/m}^3$  would be required during the entire simulation. Figure 5.4 shows some correlation between vertical flux and kinetic energy before  $t = 225$  minutes ( $U_0 = 0.63 \text{ m/s}$ ). The magnitude of the net downward flux increases when the internal wave energy increases. The increasing upward flux between  $t = 225$  minutes and  $t = 300$  minutes (between  $U_0 = 0.63$  and  $U_0 = 0.83 \text{ m/s}$ ) occurs under little wave energy. Hence this is related to a process than vertical mixing by internal waves.

Maxima of  $\overline{E_{k,z}}$  are observed around 90, 100, 125 and 180 minutes when  $U_0$  is respectively 0.25, 0.27, 0.35 and 0.50 m/s (see Figure 5.4). At  $t = 100$  minutes and  $t = 180$  minutes mode 2 and mode 1 resonance occur. The velocity and density profiles of the time instances 90 and 125 minutes also show clear wave action, however not a structure trapped to the bottom topography.

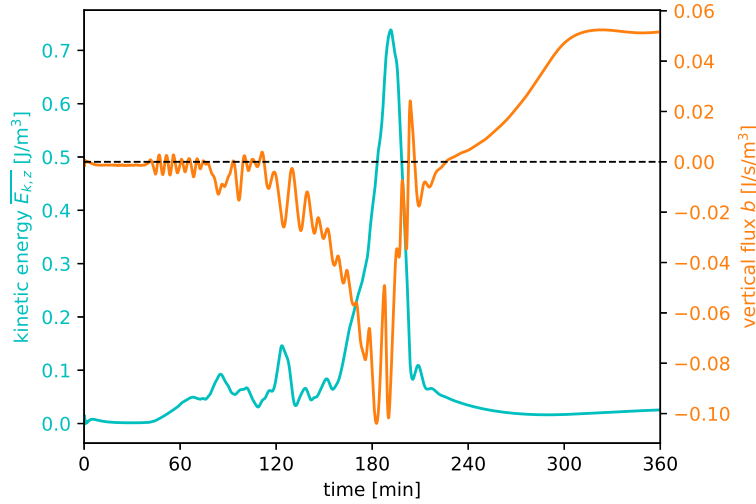


Figure 5.4: Kinetic energy  $\overline{E_{k,z}}$  and vertical density flux  $b$  for the base case *L50h050*

The above observations indicate that mode 1 is the most energetic internal wave mode, which is most clearly distinguished in the kinetic energy. The total kinetic energy is larger than the value of  $\overline{E_{k,z}}$  (which is the kinetic energy of only the vertical velocity), because it depends on both the horizontal velocity  $u$  and vertical velocity  $w$ . Assuming that the kinetic energy as function of  $u$  and  $w$  are equal and that the total kinetic internal wave energy is equal to the total potential internal wave energy, gives a total domain-average internal wave energy of  $\overline{E} \approx 4 \cdot \overline{E_{k,z}}$ . Based on this, the computed amount of energy can be related to formulation the outcome expected from the analytical formulation of total internal wave energy density given by Equation 3.7. The outcome gives the right order magnitude.

At  $t = 180$  minutes mode 1 resonance occurs and the kinetic energy  $\overline{E_{k,z}} = 0.74 \text{ J/m}^3$ . Considering resonance conditions, Equation 3.7 reduces to (explained in Section 3.3.1)

$$E = \frac{1}{4} \rho_0 \left( \frac{m^2}{k^2} + 1 \right) \hat{w}^2 \quad (5.5)$$

The value of  $\hat{w}$  for mode 1 resonance occurring at  $t = 180$  minutes can be estimated from Figure 5.2b, here  $\hat{w} = 8.3 \cdot 10^{-2} \text{ m/s}$ . An internal wave with a mode 1 structure trapped to a bed wave wave with  $L_\tau = 50 \text{ m}$  gives  $m = \frac{\pi}{15}$  and  $k = \frac{2\pi}{50}$ . Computing this in Equation 5.5 gives  $E = 6.51 \text{ J/m}^3$ . For mode 2 internal waves energy is computed by substituting  $m = \frac{2\pi}{15}$  and  $\hat{w} = 3.5 \cdot 10^{-2} \text{ m/s}$  in Equation 5.5, which gives  $E = 3.71 \text{ J/m}^3$ . The total internal wave energy estimated from the simulation value ( $\overline{E} \approx 4 \cdot \overline{E_{k,z}}$ ) gives  $2.96 \text{ J/m}^3$  and  $0.32 \text{ J/m}^3$  for mode 1 and 2 respectively. The difference between this value and the computed value of  $\overline{E_{k,z}}$  can be explained by the fact that  $\hat{w}$  is not uniform over the entire bed wave domain. Now the maximum value of  $\hat{w}$  is chosen, which is an upper end estimation.

### 5.3 Comparison to reference cases

Variations in parameters are considered to see the effect on the generated internal wave energy and the amount of vertical mixing. The base case with bed waves *L50h050* is compared to two reference cases for domain-averaged parameters associated with energy content of the internal waves (kinetic energy as function of vertical velocity  $\overline{E_{k,z}}$ ) and domain-averaged parameters associated with mixing (vertical buoyancy flux  $b$  and change in potential energy  $\frac{d\overline{E_p}}{dt}$ ). The first reference case (*ref\_nbw*) is a baroclinic flow over a flat bed, this shows what happens in a stratified channel without bed waves. The second reference case (*ref\_barotrop*) is a barotropic flow over sinusoidal bottom topography, this shows to what extent kinetic energy is caused by external flow over a sinusoidal bottom topography.

#### 5.3.1 Baroclinic flow over flat bottom

The difference between the base case (*L50h050*) and the reference case without bed waves (*ref\_nbw*) is shown in Figure 5.5 for various parameters. The main observation from Figure 5.5a is that the kinetic energy as function of vertical velocity  $\overline{E_{k,z}}$  for the case without bed waves is negligible compared to the base case with bed waves (*L50h050*). Simulations show that no internal waves are generated without bottom topography.

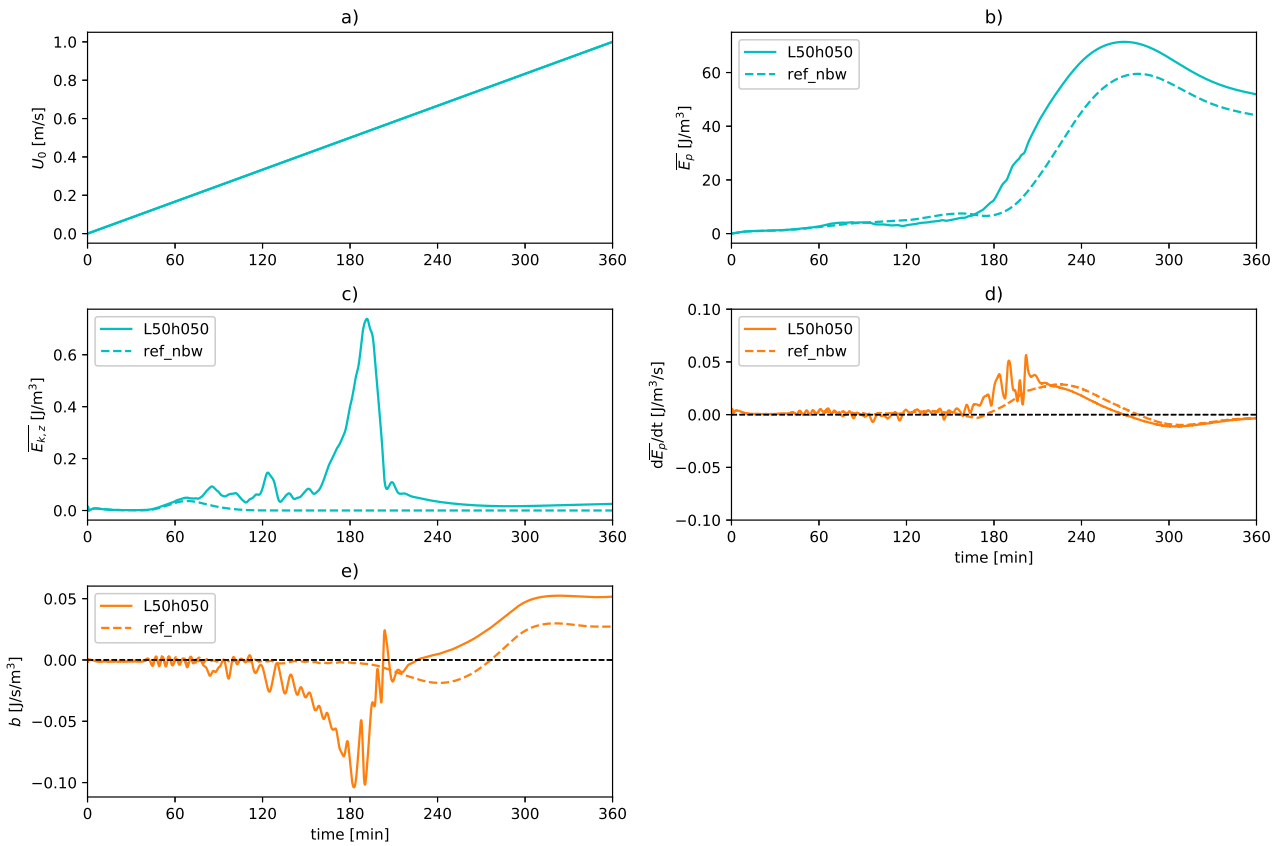


Figure 5.5: Comparison between the base case *L50h050* (solid line) and the reference case without bottom topography *ref\_nbw* (dashed line). Domain-averaged kinetic energy  $\overline{E_{k,z}}$ , domain-averaged vertical buoyancy flux  $b$ , domain-averaged potential energy  $\overline{E_p}$  and total density flux  $\frac{d\overline{E_p}}{dt}$  for a linearly increasing background flow  $U_0$ .

The vertical density flux  $b$  (Figure 5.5e) has a higher magnitude for the case with bottom topography around the time instances of high  $\overline{E_{k,z}}$ , which corresponds to occurrences of internal waves. Upward buoyancy fluxes were observed for high values of the background flow  $U_0$  (when internal waves were not present) in Figure 5.4. The same observation is made for the case without bed waves in Figure 5.5e. The vertical density flux  $b$  is around zero for the reference case up to  $t = 200$  minutes ( $U_0 = 0.56$  m/s). For the base case the flux is increasingly

negative for a higher value of  $\overline{E_{k,z}}$ . After  $t = 200$  minutes the vertical density flux follows the same structure for both cases, where the base case has a larger upward flux. The time integrated density flux without bottom topography ( $0.74 \text{ J/m}^3$ ) is slightly larger than the case with bottom topography ( $0.61 \text{ J/m}^3$ ). More about the vertical density flux and mixing is explained in Section 5.4.

The domain-averaged potential energy  $\overline{E_p}$  has a similar positive gradient in both cases, implying it is partially caused by mechanisms which are not related to the presence of bottom topography. The time instance of the greatest increase lags behind for case *ref\_nbw*. The derivative of  $\overline{E_p}$ , the total density flux, has more distinct differences between the two cases (see Figure 5.5d). When  $\overline{E_{k,z}}$  has the highest values (between 150 and 210 minutes) the total density flux is higher for the base case than for case *ref\_nbw*, which implies that additional increase in potential energy can be related to the presence of internal waves. However, other mechanisms which are present in both cases cause the major changes in the potential energy, so internal waves are not the only mechanism affecting potential energy.

The increase in  $\overline{E_p}$  (see Figure 5.5b) can be addressed to an effect caused by the increasing background flow which is similar in both cases. The increase between  $t = 180$  and  $t = 270$  minutes (when  $U_0$  increases from 0.50 to 0.75 m/s) is observed in both cases. This could be horizontal advection or due to increased bed shear stress, which are both higher for higher values of  $U_0$ . Section 5.5 further highlights the influence of bottom friction.

Both the internal wave energy and the vertical buoyancy flux are small compared to the potential energy anomaly (PEA). The maximum value of  $\overline{E_{k,z}}$  at the time instance of mode 1 resonance is  $0.74 \text{ J/m}^3$ . Taking the estimates for the total internal wave energy (as explained in Section 5.2), shows that the average internal wave energy content is only a few percent (1-3%) of the PEA for the base case.

The total increase in average potential energy  $\Delta\overline{E_p}$  is more significant compared to the PEA, however it is partially caused by processes which are not related to (internal waves generated over) sinusoidal bottom topography. For a linearly stratified fluid ranging from 1000 to 1015  $\text{kg/m}^3$  the PEA is equal to  $184 \text{ J/m}^3$  (see Equation 3.14). The net buoyancy flux integrated over the entire domain over the full simulation time is very small ( $0.61 \text{ J/m}^3$ ) compared to the required energy to fully mix the stratified water column. The total increase in average potential energy  $\Delta\overline{E_p}$  over the simulation is  $47.1 \text{ J/m}^3$  for the base case and  $40.3 \text{ J/m}^3$  for the reference case. These values are 26% and 22% of the PEA respectively. The increase in  $\overline{E_p}$  (Figure 5.5b) is around 17% more for the case with bed waves compared to the case without bed waves. However, a distinct increase also occurs without bed waves and internal waves, which suggests internal waves have a small effect on the total increase in  $\overline{E_p}$ .

### 5.3.2 Barotropic flow over sinusoidal bottom topography

For the reference case with bed waves and a uniform density (*ref\_barotrop*), kinetic energy as function of vertical velocity  $\overline{E_{k,z}}$  is the only defined quantity of the ones shown in Figure 5.5.

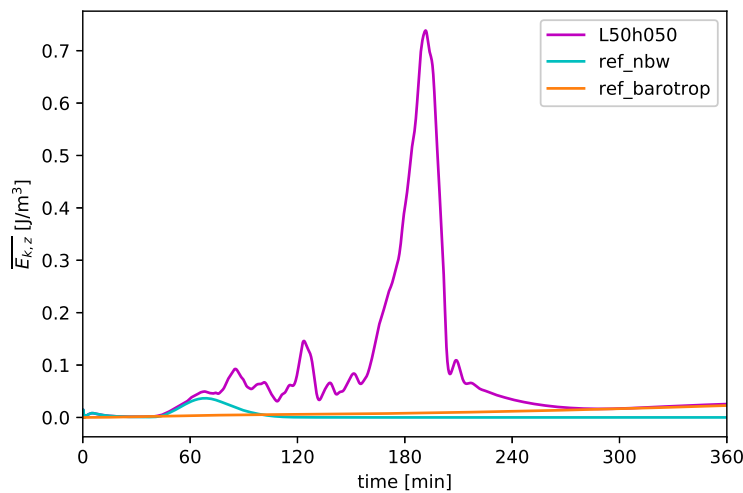


Figure 5.6: Domain-averaged kinetic energy  $\overline{E_{k,z}}$  for the base case and two reference cases. The reference cases without bed waves (*ref\_nbw*) and without stratification (*ref\_barotrop*) have a negligible amount of kinetic energy compared to the base case with stratification and bottom topography (*L50h050*).

Kinetic energy for a case without stratification shows that the 'external' vertical movement over the bottom topography with  $h_0 = 0.5$  m has a negligible influence on the contribution to kinetic energy (see Figure 5.6).

## 5.4 Analysis of vertical mixing

To investigate the nature and the regions of mixing, contour plots of the local Richardson number are investigated. Richardson numbers (Equation 2.15) below 0.25 give an indication of the presence of shear instabilities, which can contribute to mixing. Furthermore the vertical buoyancy flux is assessed in more depth, to determine which processes drive the vertical buoyancy flux.

### 5.4.1 Shear instabilities

To identify the regions of mixing the gradient Richardson number  $Ri$  (Equation 2.15) is computed throughout the entire domain for every time step. Throughout the water column  $Ri$  is equal to 1 or higher. Lower values of  $Ri$  are only found near the bed.

At some time instances  $Ri$  reaches well below 0.25 near the bed in the region of the bottom topography. For the lower bottom topography amplitudes this happens only during time instances of internal wave presence. Figure 5.7 shows  $Ri$  with maximum values of 1 for the base case  $L50h050$ . At  $t = 180$  minutes ( $U_0 = 0.50$  m/s) resonant internal waves are present (Figure 5.2) and low values of  $Ri$  are found near the bed (Figure 5.7a). At  $t = 250$  minutes ( $U_0 = 0.69$  m/s) there are no internal waves present anymore and only values of  $Ri > 0.25$  are present (Figure 5.7b).

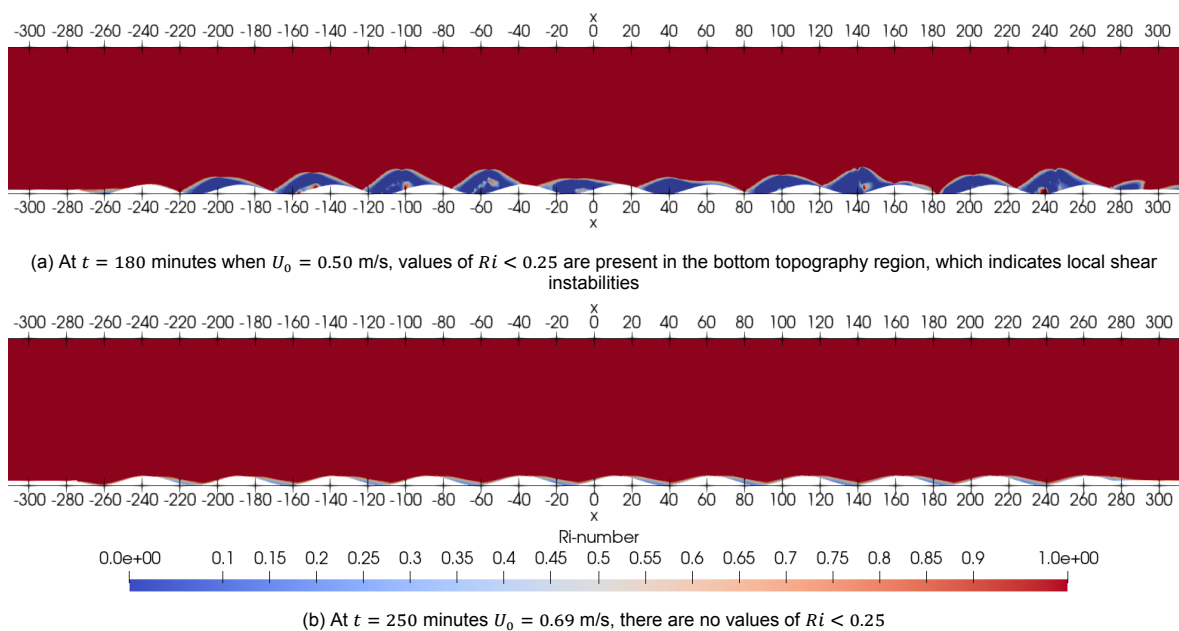


Figure 5.7: Richardson number  $Ri$  for base case  $L50h050$  where  $h_0 = 0.50$  m and  $L_\tau = 50$  m

From this can be concluded that internal waves contribute to increased shear stress around the bed, leading to shear instabilities and mixing. The interaction with the wave-induced velocities at the bed are important. Therefore the effect of bottom friction is further investigated in Section 5.5.

### 5.4.2 Vertical buoyancy flux

The vertical flux of density is a result of advection ( $\Delta\rho w$ ) and diffusion ( $\kappa \frac{d\Delta\rho}{dz}$ ). Figure 5.8 shows the domain-averaged vertical flux of potential energy  $b$  and the domain-averaged vertical velocity  $w$ .

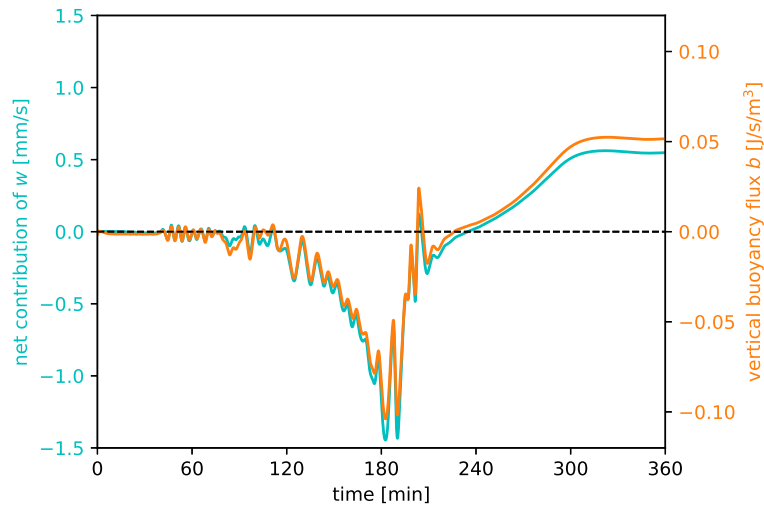


Figure 5.8: Domain-averaged vertical velocity  $w$  and vertical buoyancy flux  $b$  plotted over time for case  $L50h050$

These quantities of  $w$  and  $b$  roughly show the same structure, hence can be concluded that the vertical advection term is dominant over the diffusion term. The average domain vertical velocities ( $O \sim 10^{-4}$  to  $10^{-3}$  m/s) are a few order magnitudes smaller than the vertical velocities found in internal waves ( $O \sim 10^{-2}$  m/s).

Most shear instabilities were found at the time instance of internal wave presence ( $t = 180$  minutes), as explained in Section 5.4.1. However, at this time instance the average vertical buoyancy flux is negative (Figure 5.8), which means that the effect of the shear instabilities does not contribute to a significant upward buoyancy flux. In the simulations other processes causing changes in potential energy  $\overline{E_p}$  are dominant over vertical density transport by the observed internal waves.

Earlier observations show that the net downward fluxes are associated with time instances with high values of  $\overline{E_{k,z}}$  (presence of internal waves). The positive flux (with net upward velocities) happens without presence of internal waves. This upward flow increases for increasing background flow. When the background flow stays at a maximum of 0.5 m/s the buoyancy flux never becomes positive (see Figure F.11 of Appendix F).

The negative fluxes for high values of  $\overline{E_{k,z}}$  can be explained by additional bed friction caused by internal waves. The background flow, which is imposed by the velocity boundary, has to overcome more resistance in the channel. The additional resistance is compensated for by a reduced pressure in downstream direction (see Figure 5.9).

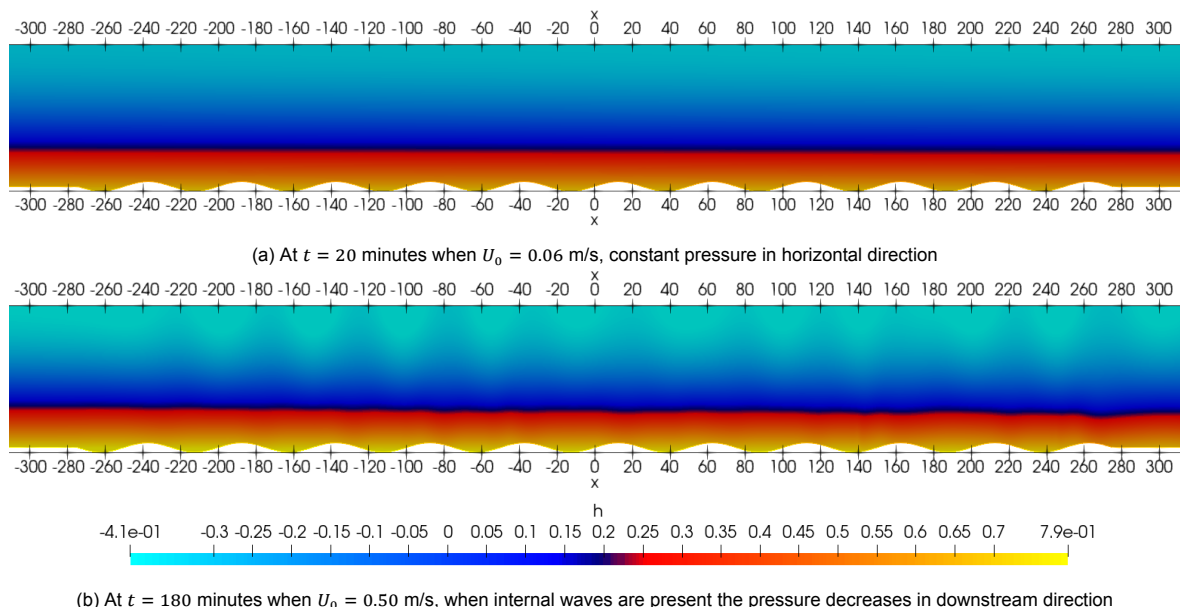
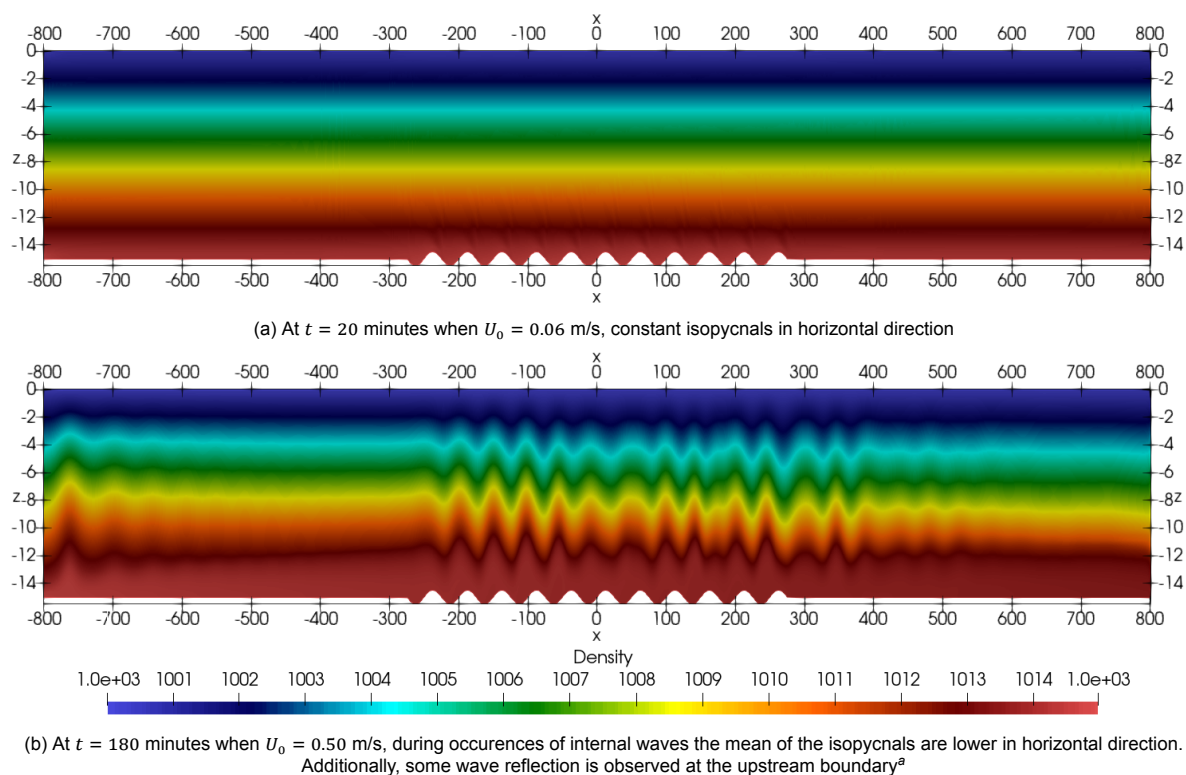


Figure 5.9: Pressure field in the bed wave domain for the base case  $L50h050$  where  $h_0 = 0.50$  m and  $L_\tau = 50$  m

To realise this lower pressure at the end of the bed wave domain as shown in Figure 5.9b, the isopycnals of the density distribution are lowered in downstream direction. This is clearly seen in the density field at  $t = 180$  minutes (Figure 5.10b) compared to initial conditions (Figure 5.10a).



<sup>a</sup>The absorbent Riemann boundary condition (which prevents wave reflection) has no application for stratified flows. Therefore, only the middle of the domain (bed wave domain between  $x = -X$  and  $x = X$  m) is considered in this study, to minimize the influence of reflecting waves.

Figure 5.10: Density field [ $\text{kg/m}^3$ ] of the full domain for the base case  $L50h050$  where  $h_0 = 0.50$  m and  $L_\tau = 50$  m

The lowering of the density profile requires a downward buoyancy flux. This effect also facilitates an increase in total potential energy, which is caused by a net horizontal density flux. A lowering of the density profile in downstream direction can result into a net horizontal buoyancy flux. Fluid with a relatively lower density is advected outside the domain than inside of the domain.

All in all, the vertical buoyancy transport is mainly caused by advective transport. During internal wave occurrences the increased flow resistance is compensated by a lowering of the isopycnals in downstream direction, which can facilitate changes in average potential energy. So the change in potential energy observed in Figure 5.5b cannot merely be addressed to vertical mixing.

## 5.5 Influence of bed friction

The sensitivity of bed friction is investigated to further explain the nature of mixing and the driving force of the observed increase in potential energy. The Nikuradse roughness is varied and a case with a frictionless bottom is investigated.

### 5.5.1 Variations in Nikuradse roughness

The domain-averaged kinetic energy as function of vertical velocity  $\overline{E_{k,z}}$  is plotted for different values of Nikuradse bed roughness  $k_n$  in Figure 5.11. For a lower bed roughness the kinetic energy increases, because a lower value of the bed roughness causes less viscous dissipation of energy in the system.

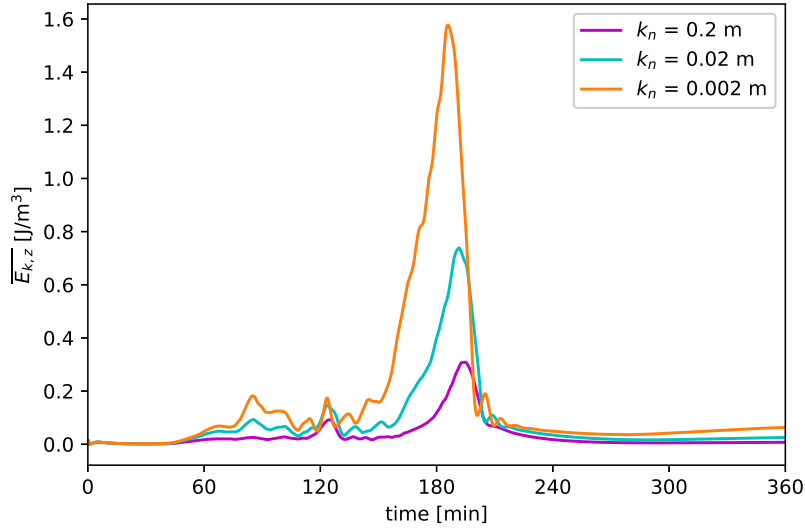


Figure 5.11: Domain averaged kinetic energy  $\overline{E_{k,z}}$  over bed wave domain for cases *L50h050*, *kn\_02* and *kn\_0002* showing influence with different values of Nikuradse roughness  $k_n$ . The kinetic energy increases for a lower bed friction.

The time averaged kinetic energy  $\langle \overline{E_{k,z}} \rangle$  also has a negative correlation with  $k_n$  (Figure 5.12). Friction at the bottom causes viscous dissipation, which decreases the wave energy. Figure 5.12b shows the time averaged buoyancy flux  $\langle b \rangle$  which also decreases for increasing  $k_n$ . Figure 5.12c shows the relative increase in potential energy due to the presence of bed waves compared to a case without bed waves  $\Delta E_{p,rel}$ , defined by

$$\Delta E_{p,rel} = \frac{\Delta E_{p,bedwaves} - \Delta E_{p,nobedwaves}}{\Delta E_{p,nobedwaves}} \cdot 100\% \quad (5.6)$$

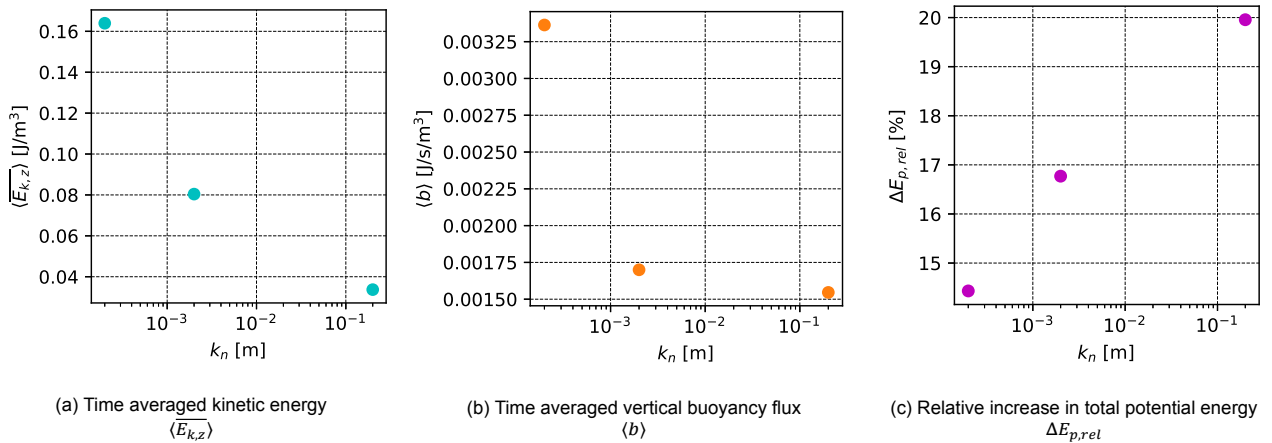


Figure 5.12: Effect of varying Nikuradse bed roughness  $k_n$  on energy parameters

The negative relation between  $k_n$  and  $\langle b \rangle$  (see Figure 5.12b), is in line with the finding in Section 5.4.2. For increased friction the vertical buoyancy flux is lower, because the increased resistance in the system needs a larger compensation, which is realised by lowering the isopycnals.

The effect on the relative increase in potential energy is opposite, for less friction (increasing internal wave energy) there is a smaller increase in  $\Delta E_{p,rel}$  (Figure 5.12c), in this case the effect of decreased bottom friction seems dominant over the increased availability of internal wave energy. The relative increase in potential energy compared to a similar case without bottom topography varies between 14% and 20% (corresponding to 4.7 to 9.3 J/m<sup>3</sup>, being between 2 and 5% of the PEA). The time averaged parameters  $\langle \overline{E_{k,z}} \rangle$  and  $\langle b \rangle$  are three orders magnitude smaller than the PEA and the average buoyancy flux to reach the PEA respectively.

## 5.5.2 Frictionless bottom

Here a theoretical case without any bed friction is simulated with a bottom boundary condition with free slip. The same background flow and bottom topography are imposed as for case *L50h050*. Here the reference case *kn0\_nbw* is a flat bed with a free slip bottom boundary condition. The density profile shows internal wave amplitudes up to 4 m (see Figure 5.13), which is significantly higher than the amplitudes found for the base case where  $k_n = 2 \cdot 10^{-2}$  m, where overturning is observed at  $x = -140$  m.

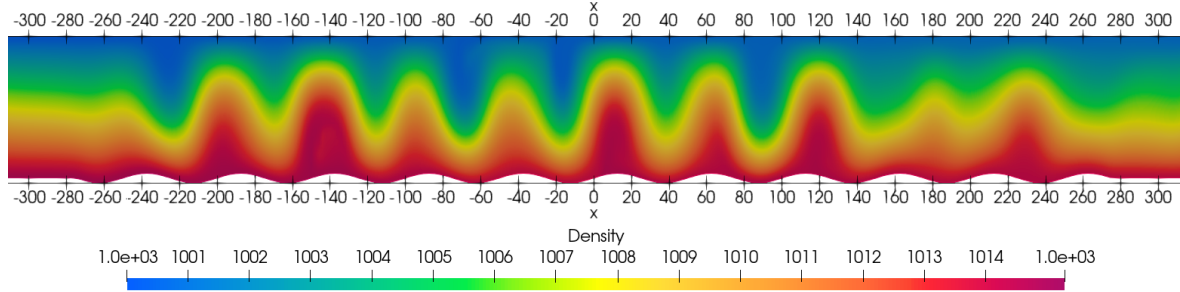


Figure 5.13: Density field [kg/m<sup>3</sup>] of case *kn\_0* which has a frictionless bed, at  $t = 150$  minutes when  $U_0 = 0.42$  m/s when high amplitude mode 1 internal waves have overturning structures

In Figure 5.14 the same quantities are plotted as done for the base case in Figure 5.5. The plot of kinetic energy as function of vertical velocity  $\overline{E_{k,z}}$  (Figure 5.14c) shows a higher amount of kinetic energy than for case *L50h050*, which is in line with the higher amplitudes observed in Figure 5.13.

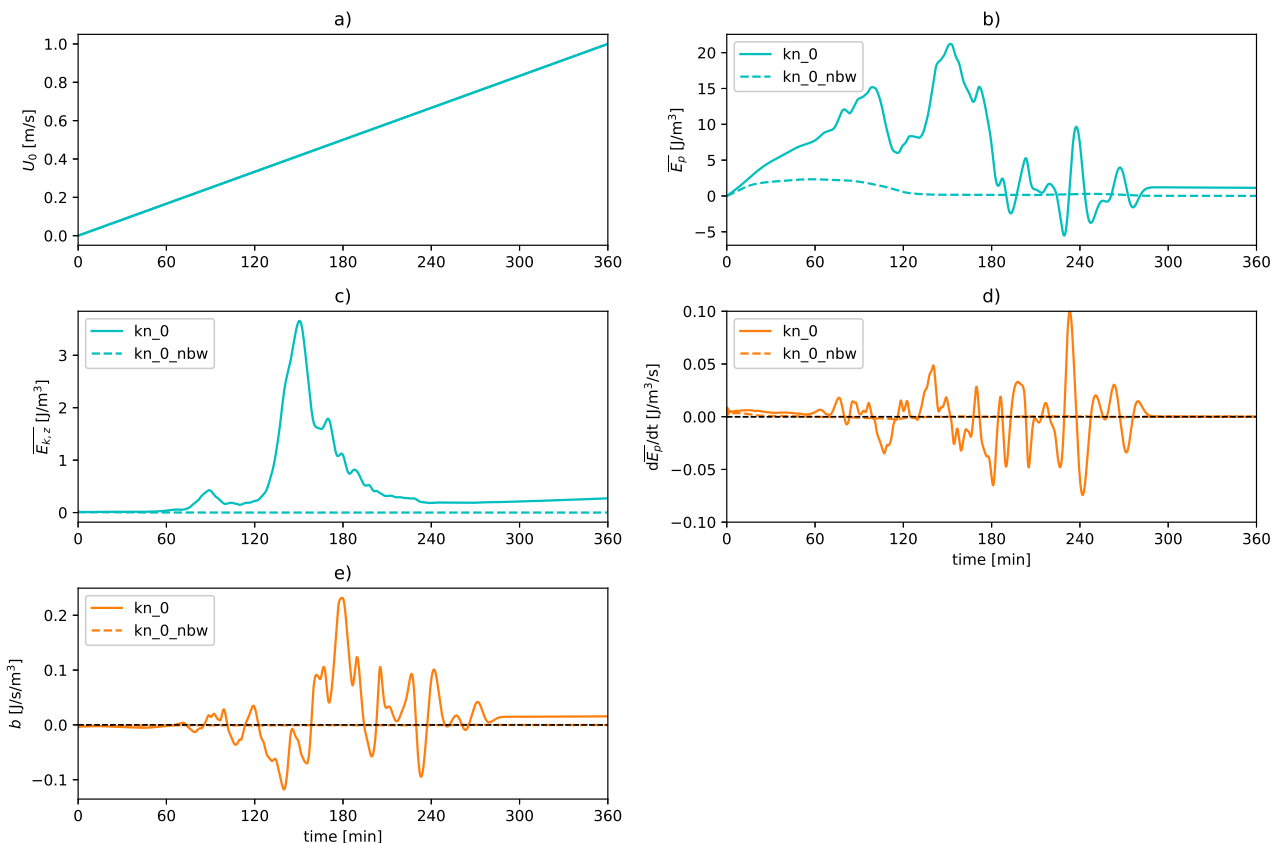


Figure 5.14: Difference between the base case without bottom friction *kn\_0* (solid line) and the reference case without bottom topography or bottom friction *kn\_0\_nbw* (dashed line). Domain-averaged kinetic energy  $\overline{E_{k,z}}$ , domain-averaged vertical buoyancy flux  $b$ , domain-averaged potential energy  $\overline{E_p}$  and total density flux  $\frac{d\overline{E_p}}{dt}$  for a linearly increasing background flow  $U_0$ .

Different behaviour is observed compared to the cases with bed friction. The main observations from Figure 5.14 compared to the base case with friction (Figure 5.14) are that upward buoyancy fluxes occur when internal waves are present and the total potential energy is constant for the frictionless case without bed waves (*kn\_0\_nbw*). For a frictionless bottom the increase in potential energy should be caused by vertical fluxes induced by internal waves.

Due to the absence of friction, the background velocity corresponding to mode 1 resonance is closer to the value based on the (frictionless) analytical expression. Mode 1 resonance is observed at  $t = 150$  minutes when  $U_0 = 0.42$  m/s, which is very close to theoretical value of  $U_0 = 0.41$  m/s.

The vertical buoyancy flux  $b$  (Figure 5.14e) is not as strongly correlated to the time instances with high values of  $\overline{E_{k,z}}$  as for the cases with bottom friction. In the time interval of highest kinetic energy (between  $t = 130$  and  $t = 190$  minutes) both upward and downward fluxes are present. The time integrated buoyancy flux is  $4.54$  J/m<sup>3</sup> and the maximum positive value of  $b$  reaches a higher value compared to the base case (Figure 5.5e).

At the beginning of the simulation total potential energy  $\overline{E_p}$  increases, however, afterwards there is an increase, so the net increase is negligible. The change in  $\overline{E_p}$  is nearly zero for the case without bed waves (Figure 5.14b). For the case with bed waves it is highest during occurrences of internal waves. This confirms that the change in  $\overline{E_p}$  for the cases with bed friction, must also be influenced by bottom shear (or processes occurring as a result of bottom shear).

## 5.6 Variation of bottom topography parameters

### 5.6.1 Bottom topography amplitude

Here the bottom topography amplitude  $h_0$  is varied where the bottom topography wavelength is equal in all cases ( $L_\tau = 50$  m). Figure 5.15 shows the domain-averaged kinetic energy as function of vertical velocity  $\overline{E_{k,z}}$  for different bottom topography amplitudes  $h_0$ . For higher bottom topography amplitude higher values of  $\overline{E_{k,z}}$  are observed. The bottom topography amplitude has no influence on the time instance (corresponding background flow velocity  $U_0$ ) at which resonance occurs. This is according to the analytical expression of Equation 3.12, which is visualized in Figure 3.8. Those maxima in the graph of  $\overline{E_{k,z}}$ , corresponding to mode 1 resonance have values between  $0.2$  and  $3.1$  J/m<sup>3</sup>. Based on the assumption made in Section 5.2 for the total amount of internal wave energy ( $\overline{E} \approx 4 \cdot \overline{E_{k,z}}$ ), the total internal wave energy is estimated between  $0.4\%$  and  $6.7\%$  of the PEA.

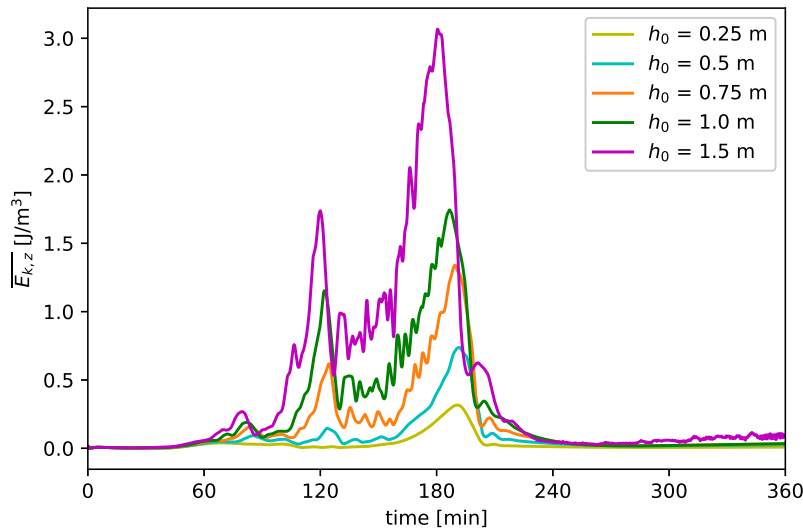


Figure 5.15: The effect of varying bottom topography amplitude  $h_0$  on domain-averaged kinetic energy  $\overline{E_{k,z}}$ . For higher values of  $h_0$  the energy content is higher.

The kinetic energy shown in Figure 5.15 is time averaged and plotted against the values of  $h_0$  in Figure 5.16a. Time averaged kinetic energy  $\langle \overline{E_{k,z}} \rangle$  increases nearly linearly with  $h_0$ . However, from frictionless linear theory a quadratic relationship is expected. Viscous dissipation in the simulations induce an energy loss, which could

explain the difference between the theoretical relation and the relation found from simulation results.

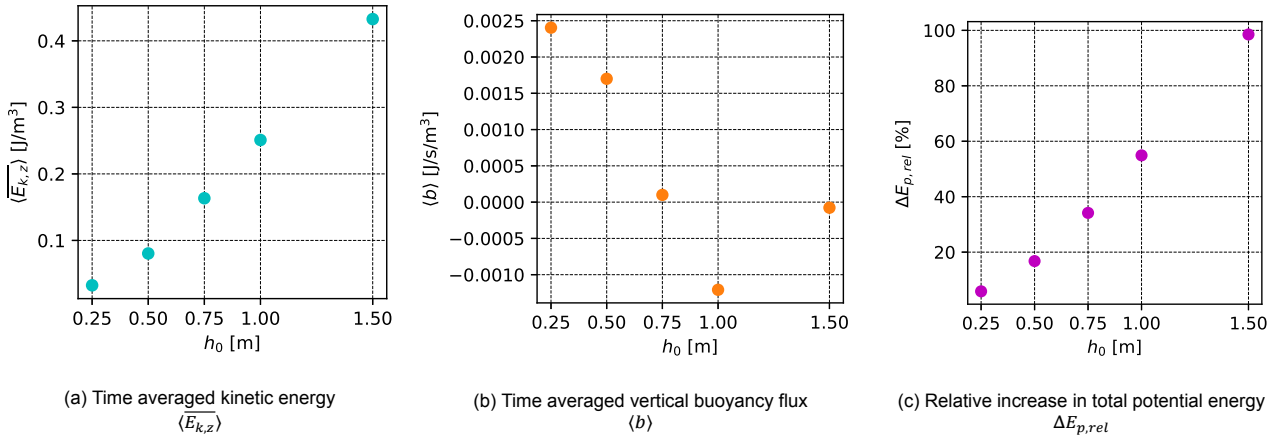


Figure 5.16: Effect of varying bottom topography amplitude  $h_0$  on energy parameters

The time averaged buoyancy flux  $\langle b \rangle$  is plotted against  $h_0$  in Figure 5.16b. This shows a negative correlation between  $h_0 = 0.25$  m and  $h_0 = 1.00$  m, and for  $h_0 = 1.50$  m  $\langle b \rangle$  increases with respect to  $h_0 = 1.00$  m. This is in line with the negative vertical fluxes found during internal waves presence. Similar behaviour to the base case (Figure 5.4) is seen for other cases with bottom topography amplitude variations, shown in Figures F.1 to F.4 of Appendix F. The resistance in the bed wave area increases for higher values of  $h_0$  due to an increased bed area. The values of  $\langle b \rangle$  are three orders magnitude smaller than the required average buoyancy flux to overcome the PEA (this is  $0.5$  J/s/m<sup>3</sup>, as explained in Section 5.2).

There is a positive linear relation between  $h_0$  and relative increase in total potential energy  $\Delta E_{p,rel}$ . The percentages ranging between 6% and 99% correspond to an additional average increase of potential energy between 2 and 40 J/m<sup>3</sup> over the duration of the 6 hours simulation. This additional increase in potential energy is significantly higher than the values found in Section 5.6.2 for variations in  $L_\tau$ . This difference can be explained by a larger mixing region that is present for higher bed waves, and they stay present for a longer amount of time. Figure 5.17 shows contour plots of the Richardson number for case  $L50h150$ , where  $h_0 = 1.5$  m, at different time instances, which shows shear instabilities near the bed.

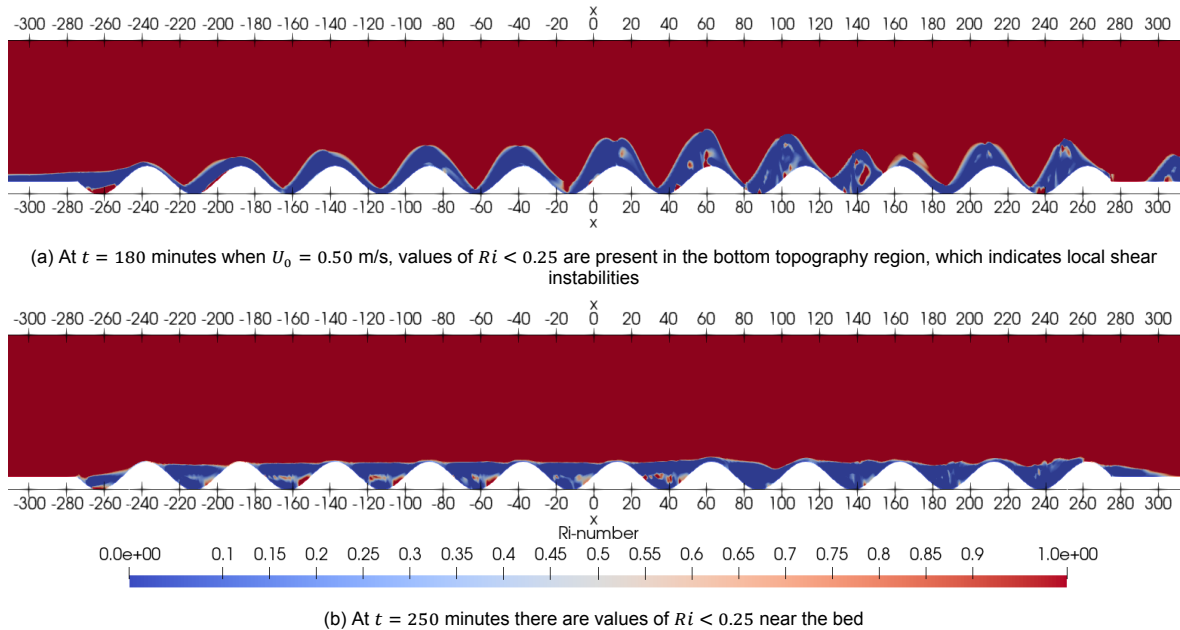


Figure 5.17: Richardson number  $Ri$  for simulation  $L50h150$  where  $h_0 = 1.50$  m and  $L_\tau = 50$  m

For larger bottom topography amplitudes  $h_0$  there is a larger region of instabilities and the instabilities stay present

in the domain even after the internal waves have significantly decreased in amplitude. For larger  $h_0$  the lower values for  $Ri$  are also found along the bottom at time instances with small or no internal waves. At the time instance with low values of  $Ri$  near the bed when internal waves are present ( $t = 180$  minutes) overturning is visible at the bed (Figure 5.18). This behaviour is also seen in the vertical buoyancy flux plotted in Figure F.4.

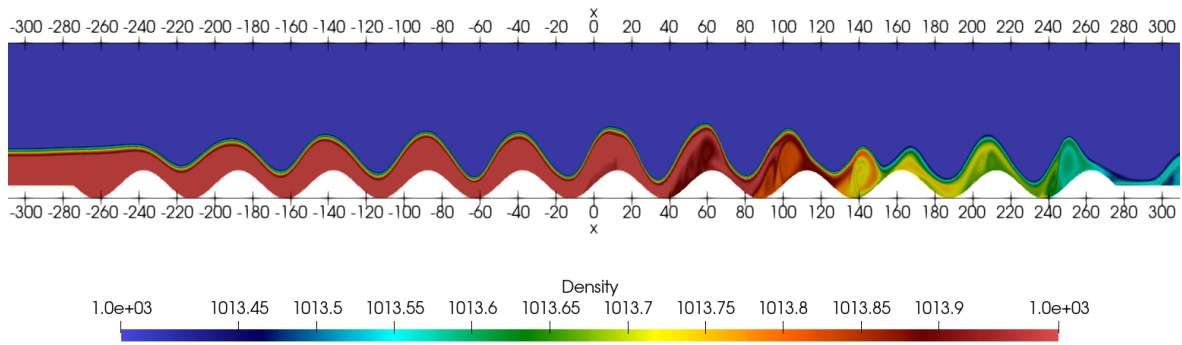


Figure 5.18: Density field [ $\text{kg/m}^3$ ] for simulation  $L50h150$  where  $h_0 = 1.50$  m and  $L_\tau = 50$  m overturning structures near the bottom at  $t = 180$  minutes

This overturning is not observed for lower bottom topography amplitudes, where mixing is only caused by shear instabilities. The amplitude of the bed waves has an important effect on mixing near the bed.

### 5.6.2 Bottom topography wavelength

Here the bottom topography wavelength  $L_\tau$  is varied where the bottom topography amplitude is equal in all cases ( $h_0 = 0.5$  m). Figure 5.19 shows the domain-averaged kinetic energy as function of vertical velocity  $\overline{E_{k,z}}$  for different bottom topography wavelengths. There is a clear shift of the maxima of kinetic energy to higher velocities  $U_0$  (later in time) for larger bottom topography wavelengths. This is in line with theory, for longer bottom topography wavelengths resonance occurs at higher flow velocities (see Figure B.2 to Figure B.6 in Appendix B). The values of the maxima of  $\overline{E_{k,z}}$  increase between  $L_\tau = 20$  m to  $L_\tau = 40$  m, and decrease after that (see Figure 5.19). According to the analytical expression (Equation 3.12), the bottom topography wavelength has two effects on the magnitude of the internal wave energy as explained in Section 3.4, so this behaviour could be expected.

The range of flow velocities for the interval near resonance is larger for higher flow velocities (Figure 3.6). This results in increasing wave energy for higher  $U_0$ . Another effect is that larger bottom topography wavelengths have relatively less friction, which causes less dissipation of internal wave energy. This effect is not explained by the analytical expression, because friction is neglected in the analytical analysis. Contrarily, the internal wave energy has a quadratic relation with  $k_\tau$  (Equation 3.12). Larger wavelengths have smaller gradients at the bed, generating smaller accelerations which results in less wave energy. The tipping point of these competing mechanisms seems to be at  $L_\tau = 40$  m for this case.

Those maxima in the graph of  $\overline{E_{k,z}}$ , corresponding to mode 1 resonance have values between 0.5 and 1.0  $\text{J/m}^3$ . This range is smaller than the ranges found for variations in  $h_0$ . Based on the assumption made in Section 5.2 for the total amount of internal wave energy ( $\overline{E} \approx 4 \cdot \overline{E_{k,z}}$ ), the internal wave energy is estimated between 1% and 2% of the PEA.

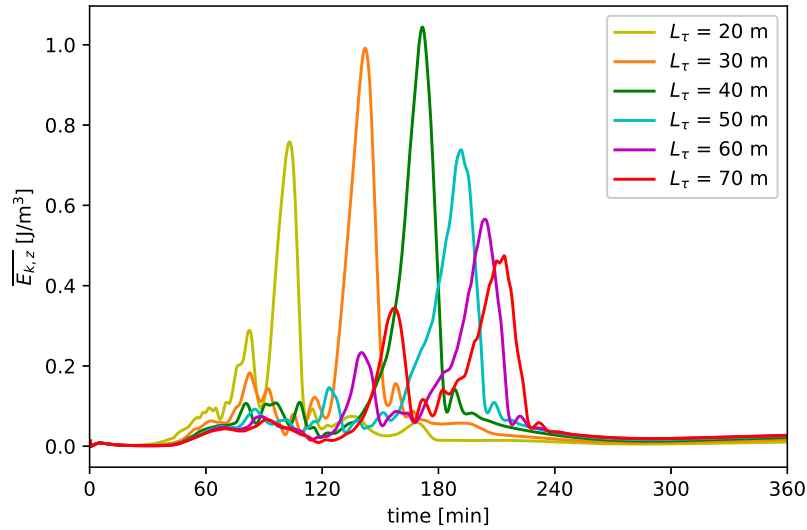


Figure 5.19: The effect of varying bottom topography wavelength  $L_\tau$  on domain-averaged kinetic energy  $\overline{E_{k,z}}$ . For higher values of  $L_\tau$  the maxima shifts to later time instances, corresponding to higher flow velocities

The kinetic energy shown in Figure 5.19 is time averaged and plotted against the values of  $L_\tau$  in Figure 5.20a. Time averaged kinetic energy  $\overline{E_{k,z}}$  increases between  $L_\tau = 20$  m to  $L_\tau = 40$  m, decreases between  $L_\tau = 40$  m to  $L_\tau = 60$  m and is roughly the same for  $L_\tau = 60$  m and  $L_\tau = 70$  m.

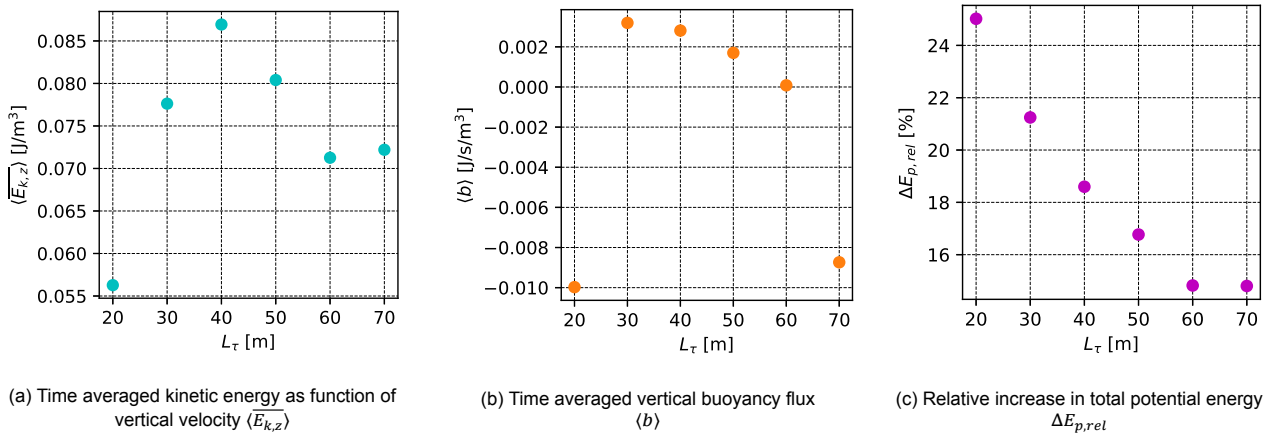


Figure 5.20: Effect of varying bottom topography wavelength  $L_\tau$  on energy parameters

Due to the different effects of  $L_\tau$  on the internal wave energy there is no very clear correlation between  $L_\tau$  and  $\langle \overline{E_{k,z}} \rangle$  or  $\langle b \rangle$ . This suggests that there is an optimum bottom topography wavelength to achieve the most energetic internal waves. The time averaged buoyancy flux  $\langle b \rangle$  is plotted against  $L_\tau$  in Figure 5.20b and shows a negative correlation, with exception of  $L_\tau = 20$  m.

There is a negative correlation between  $L_\tau$  and relative increase in total potential energy  $\Delta E_{p,rel}$  shown in Figure 5.20c. This would suggest that the amount of internal wave energy does not have a significant influence on  $\Delta E_{p,rel}$ , however, the influence of friction is more relevant. Increasing  $L_\tau$  corresponds to a relatively smaller bed area, which decreases bed resistance. This can explain the negative correlation shown in Figure 5.20c. The values ranging between 15% and 25% correspond to an additional average increase of potential energy between 6 and 10 J/m<sup>3</sup>. The total increase in average potential energy for the cases with bed waves ranges between 46 and 50 J/m<sup>3</sup>. This increase is about 25% of the PEA. It has to be noted however, that this increase in potential is also caused by a net horizontal buoyancy flux and bed friction induced mixing.

A relatively long part of the simulation there is no resonance. This could be optimized when a combination of bottom topography wavelengths is used, because with an unsteady tidal flow some resonance conditions are reached multiple times.

## 5.7 Summary parameter study

Simulations with a linearly increasing background flow show different time instances at which resonant trapped internal waves of the first two modes are generated. Different values of the bottom topography wavelength  $L_\tau$  result into different time instances (corresponding to different background flow velocities) of internal wave generation. The mode 1 response is most energetic, which is recognised by maxima in plots of kinetic energy as function of vertical velocity  $\overline{E_{k,z}}$ . The amount of internal wave energy is only 0.4% to 6.7% of the PEA.

The two considered reference cases (*ref\_nbw* and *ref\_barotrop* in Table 5.2) generate a negligible amount of  $\overline{E_{k,z}}$  compared to the case with both bed waves and stratification. This confirms that a stratified flow over a flat bed nor barotropic flow over bottom topography generates a significant amount of  $\overline{E_{k,z}}$ .

The net vertical buoyancy flux over the entire simulation, is almost equal for both cases with and without bed waves. An increase in domain-averaged potential energy  $\overline{E_p}$  is observed in both cases with and without bed waves, where the increase is larger for cases with bed waves (17% for the base case).

Richardson numbers below 0.25, associated with shear instabilities and mixing, are only observed near the bed, mainly when internal waves are present. The region of shear instabilities is larger for higher bottom topography amplitudes, and the instabilities stay present for a longer time period. The vertical buoyancy flux  $b$  is governed by advection and is downward directed during occurrences of internal waves. The increased bed resistance due to bottom topography induces additional resistance which the flow has to overcome. This is compensated for by a lower pressure downstream the bed wave domain, which is realised by lowering the isopycnals. Lowering of the isopycnals requires a negative buoyancy flux.

The system is sensitive to variations in Nikuradse bed roughness  $k_n$ . For increasing  $k_n$  the kinetic energy decreases, because more energy is dissipated. Contrarily, the time averaged buoyancy flux  $\langle b \rangle$  decreases with increasing bed roughness. More resistance requires more compensation by lowering the isopycnals. Increasing  $k_n$  increases the relative increase in potential energy (due to bed friction) compared to a case without bed waves  $\Delta E_{p,rel}$ . A case with a frictionless bottom shows amplitudes which are significantly higher than the bottom topography amplitude, up to a factor eight for mode 1 resonance. There is no increase in potential energy for a case without bed waves, which confirms that the interaction between flow velocity and bed friction causes an increase in potential energy.

The bottom topography amplitude  $h_0$  has a positive quadratic relation with  $\overline{E_{k,z}}$  and  $\Delta E_{p,rel}$ , and a negative relation with  $\langle b \rangle$ . Bottom topography wavelength  $L_\tau$  does not have a clear relation with  $\overline{E_{k,z}}$  and  $\langle b \rangle$ , because  $L_\tau$  influences the magnitude of internal wave energy as well as the resonance conditions. There is a negative relation between  $L_\tau$  and  $\Delta E_{p,rel}$ , which can be related to the amount of decreasing friction for increasing  $L_\tau$ . Changes in  $h_0$  have the most significant effect on internal wave energy generation and mixing.

Based on these observations several conclusions are drawn. The generated amount of energy is orders magnitudes smaller than the total amount of energy to fully mix a stratified water column. Vertical buoyancy flux has a domain averaged and time integrated value in order of  $10^{-2}$  J/m<sup>3</sup>. This is one order magnitude smaller than the absolute time integrated vertical buoyancy flux and two orders magnitude smaller than the total increase in potential energy.

The system is sensitive to bed resistance. A higher amount of friction results into a larger increase in total potential energy. This is caused by bottom induced shear instabilities, which are enhanced during internal wave presence. Additionally, a lowering of the isopycnals causes a net horizontal buoyancy flux. In this case the change in potential energy is caused by the net horizontal density fluxes. Bed resistance changes for a different value of  $k_n$ , but also for different bed wave configurations determined by  $h_0$  and  $L_\tau$ .

# 6

## Discussion

This study finds that applying undular bed topography generates resonant internal waves. The generation of internal wave energy is qualitatively well described by the formulation given in the analytical study. Applying undular bed topography in a stratified channel, generates additional mixing near the bed compared to a flat bed. Furthermore, the presence of internal waves enhance mixing induced by bottom friction. The Nikuradse bed roughness  $k_n$  is a parameter which significantly influences this behaviour. On one hand it induces viscous dissipation, decreasing internal wave amplitudes. Contrarily, a higher bed roughness increases mixing near the bed. The value of the bed roughness is not validated, such validation, however, is relevant due to the high sensitivity to friction. Consequently, proper quantification of bed friction induced mixing is challenging. Besides the uncertainty in the amount of friction, other model limitations and assumptions in this study cause a limitation in the quantification of the vertical mixing caused by (internal waves generated over) undular topography. Furthermore, model simplifications with respect to circumstances in the RWW are addressed. Finally some discussion points on the practical applicability are raised.

### 6.1 Quantification of vertical mixing

The amount of vertical mixing is a significant parameter in this study, the objective was to investigate whether internal waves can contribute to vertical mixing and hereby reduce stratification. Uncertainties in quantifying vertical mixing by internal waves are caused by various aspects of the approach and the model. Model limitations are found in turbulence modelling and the representation of diffusion in the model. Two simplifications in the model alter the amount of mixing compared to reality; cases where wave breaking is expected were not simulated and the density profile is simplified. Due to the uncertainties in the amount of mixing by internal waves, the mixing efficiency has not been determined. Finally, the significance of mixing by internal waves is related to salt intrusion.

#### 6.1.1 Performance of the turbulence model

When the Navier-Stokes equations are not directly solved in a numerical model, a turbulence closure model is applied, which always introduces uncertainties in the model. Large Eddy Simulation (LES) with a Smagorinsky turbulence closure model is used in the simulations of this study. Two points of discussion arise concerning the performance of this turbulence model for the application of this study.

First of all there is no lab data available for internal waves generated over sinusoidal bottom topography or internal wave breaking and mixing data on the required scale. Therefore, the turbulent behaviour calculated by the model cannot be directly validated for this specific application. The lab experiment in a tank with a moving wave paddle by Taylor (1992) does not give a direct validation on turbulence and mixing either.

Secondly, the grid resolution is relatively coarse compared to the displacement lengths found by Uittenbogaard and Imberger (1993) from turbulence measurements in the RWW. The model resolution in the bed wave domain is defined by  $\Delta x = 500$  mm and  $\Delta z = 375$  mm, while displacement lengths are of order 20 - 200 mm. This means that relevant turbulent scales are currently solved by the subgrid closure model, leading to either over- or

underestimation of the amount of generated turbulence. Increasing the resolution to a scale which can resolve mixing length scales of order  $10^{-2}$  m is computationally challenging, and therefore not considered a feasible approach.

### 6.1.2 Representation of diffusion in the model

The LES turbulence closure model calculates the turbulent diffusivity. The total diffusion in the model is a sum of a default diffusion rate  $\kappa$ , the calculated turbulent diffusion and the numerical diffusion. This total amount of diffusion in the model determines how much diffusive mixing is computed.

The first discussion point on diffusion is on the default  $\kappa$ . For the validation case by Taylor (1992) (with low velocities and high Richardson numbers) is concluded that the default value of diffusion ( $\kappa = 10^{-6} \text{ m}^2\text{s}^{-1}$ ) is at least two orders magnitude too high. The Prandtl-Schmidt number ( $\sigma = \frac{\nu}{\kappa}$ ) in the field of civil engineering is mainly assumed to have a value around 1. The question arises whether this formulation of  $\sigma$  should be reconsidered in stratified flows of estuary scale.

From the vertical buoyancy flux calculated in this study can be derived that the vertical advection is dominant over the diffusion term (see Figure 5.8). Therefore, there does not seem to be a direct reason to apply a different value for  $\sigma$  in this study. However, in the bigger context of modelling of estuaries this should be kept in mind.

Second, in the calculation of the turbulent diffusivity, the influence of density effects is not taken into account. In other words, there is no subgrid closure for diffusion. This gives a larger uncertainty in the mixing of the solved constituent caused by the smallest turbulent scales and diffusion. Again the significance of this effect could be investigated by means of laboratory experiments or field data.

Third, the observed values of numerical diffusion are low, this is promising for other studies where physical diffusion and mixing are important. Diffusion rates are observed in variations of resolution and  $\sigma$  for the validation case (Figures 4.7 and 4.9) and in the contribution of diffusion in the total buoyancy flux in the RWW cases (Figure 5.8). If the mixing by internal waves can be well presented by the model, numerical diffusion is expected to have negligible influence on the results.

### 6.1.3 Linear stratification

A model simplification is that the channel has a linearly stratified fluid, while the stratification structure in the RWW can better be described by a hyperbolic tangent function (see Figure A.1). In such stratification profile the regions near the bed and near the surface are better mixed than for a linearly stratified fluid. Model results show that mixing due to bed induced shear instabilities is an important process.

Therefore, the analysis made in this study is not completely representative for the RWW. Bed friction induced mixing might not be as significant with a hyperbolic tangent density profile.

### 6.1.4 Wave breaking

The expectation was that internal waves would generate mixing by local shear instabilities or wave breaking. In this study breaking waves were not observed for realistic cases. Only for the case where internal waves reflected at the boundaries and started interfering with waves in the middle of the domain, this simulation did show however that vertical mixing was enhanced (Figure F.10). Those simulation results also show that breaking waves generate more upward buoyancy fluxes and have more potential to generate vertical mixing. In the RWW waves could also break at the banks or at other objects, such scenarios were not captured in the 2D simulations. Breaking internal waves have significant implications for turbulence production and mixing (Lamb, 2014, Staquet and Sommeria, 2002), therefore taking into account wave breaking at banks and objects is expected to increase the vertical mixing.

### 6.1.5 Quantification of mixing efficiency

Mixing efficiency of internal waves can be defined by the fraction of the released internal wave energy that is utilized for irreversible mixing. The difficulty of determining the amount of vertical mixing induced by internal

waves, directly complicates the proper computation of a mixing efficiency. Alternatively, all the RWW cases are also simulated without bed waves, to compensate for other mixing effects that also occur with a flat bed. However, mechanisms caused by a stratified flow over a undular bottom topography unrelated to internal waves could also cause additional mixing.

Mixing is analysed by considering the change in total potential energy and by considering the vertical density flux. Both quantities have the complication that the nature of mixing cannot be determined exactly.

The change in potential energy can occur due to horizontal density fluxes as well as vertical density fluxes. The total potential energy is a relevant parameter to put the vertical fluxes into perspective with the total change in density structure. The vertical density flux can be directly linked to vertical mixing. This vertical mixing can still be driven by various processes; shear instabilities and breaking by internal waves and background flow induced bottom shear. Discrimination between those processes cannot directly be made.

The definition of *irreversible* mixing is not straightforward with a varying background flow, as experienced in the RWW. The background flow is a constantly changing driving force, that drives another mixing mechanism (internal waves). Additionally, other mechanisms play a role in the change in potential energy. A net increase in potential energy over one tidal cycles could be a good starting point.

Finally, a note on a future consideration for the mixing efficiency with time dependency is made. Currently, the potential energy anomaly (PEA) is compared to the internal wave energy, to give an indication on the potential of internal waves to reduce stratification. Both quantities are defined as an energy density with the unit  $J/m^3$ . In reality horizontal buoyancy renewal takes place due to river discharge. This facilitates restratification of the water column and introduces a time dependency of the PEA, as described by Simpson et al. (1990). Coupling a time-dependent mixing efficiency to a time-dependent expression of the PEA (or another quantity that accounts for restratification by river discharge) could give an improvement in the approach.

### 6.1.6 Significance of vertical mixing for salt intrusion

For the same reasons that the mixing efficiency of internal waves is not yet determined, there is not a strong conclusion on the significance of mixing by internal waves yet. Such mixing efficiency is relevant to conclude how effective applying undular topography can be to mitigate salt intrusion. The amount of generated internal wave energy is small compared to the PEA and this comparison does not provide a direct relation to the effect on salt intrusion. Pietrzak et al. (1991) derives an analytical expression for the ratio between the wave-induced production of turbulent kinetic energy and the turbulent kinetic energy of the background flow. This ratio can be used in an estimation of the contribution of internal waves to the reduction of salt intrusion length. Salt intrusion length is inversely proportional to a third power to vertical mixing according to the relation for a idealised estuary (Equation 2.1).

Measurements conducted at field campaigns in the RWW found a significant amount of turbulence production due to internal waves that cannot be neglected (Pietrzak et al., 1991), with respect to the turbulence production by the mean flow. So this should be considered in further analysis by the interpretation of model results.

## 6.2 Simplifications and assumptions in the model

Assumptions are made for the boundary conditions. The implications of these simplifications on the results, compared to the expected behaviour in the RWW, are discussed here.

### 6.2.1 Velocity boundaries

For simplicity, the modelling cases have a linearly increasing flow velocity instead of flow conditions determined by the tide. The flow velocity in the RWW is governed by the tide. The background flow velocity is a major parameter which determines the resonance conditions for the generation of internal waves over undular bottom topography. For a linearly increasing flow all the flow velocities occur for an equal amount of time. Considering a sinusoidal tide, accelerations will occur. Therefore the time frame at which certain velocities occur can greatly differ. This could alter the results of the difference between effectiveness of the different bottom topography wavelengths, since this parameter is also linked to the resonance condition.

The simulations have boundary conditions with uniform flow velocity over depth and an inflow concentration similar to the initial condition (a linearly stratified density profile). This implies that the effect of gravitational circulation is not taken into account. Gravitational circulation has different effects on different moments of the tidal flow. The residual flow pattern is a superposition of tidal flow and the exchange flow. The effect is a reduced flow velocity near the bed for ebb flow and an increased flow velocity near the bed for flood flow.

### 6.2.2 Rigid lid surface

A rigid lid is used as upper boundary in simulations of the RWW instead of a free surface. This simplification is made to neglect the influence of surface waves, because this study focuses on internal waves. This simplifies the interpretation of the model results, since there is no necessity to verify whether certain effects are caused by the surface or internal waves.

In reality these surface waves and internal waves do interact. Energy can also be present in fluctuations and movements of the free surface. This energy is extracted somewhere else in the system. Similar simulations with a free surface could have less energetic internal waves, since part of it will be present in the form of surface waves. However surface waves caused by internal waves have amplitudes which are significantly smaller<sup>1</sup> than the internal wave amplitudes.

### 6.2.3 Internal wave reflection at open boundaries

In the simulations of the RWW reflecting internal waves are observed at both inflow and outflow boundaries. In barotropic flows this can be solved by implementing a weakly reflective Riemann boundary condition. Such a weakly reflecting boundary does not exist for baroclinic flows. This reflection causes more internal wave action in the domain than would occur in real situations. In the case for a linearly increasing tide this effect can be accounted for by only considering the middle of the domain. This was a suitable approach for the purpose of this study, because the influence of the boundaries did not result in a visible influence in the considered domain.

For a sinusoidal tide the deceleration of the flow causes propagation of free waves further upstream and downstream. The reflected waves from both boundaries start interfering in the middle of the domain which causes chaotic motions and wave breaking. From this point the results become unrealistic in the entire modelling domain. In reality these internal waves would have propagated outside the domain.

## 6.3 Practical applicability

The bed wave amplitude  $h_0$  is the bottom topography parameter which gives the most significant effect on generated internal wave energy and increase in potential energy. In practice there will be an upper limit of applicability of very high values of  $h_0$ . Navigation in the RWW requires sufficient keel clearance. Furthermore, it should be kept in mind that the internal wave induced velocity gradients should not hinder shipping. Ships experience the largest hinder by horizontal density gradients. In the bed wave design it should be taken into account whether there is a threshold for horizontal velocity gradients.

## 6.4 Concluding remarks

All in all, this study cannot give a final conclusion on the significance of vertical mixing by internal waves generated over undular bottom topography. The main challenge in the model is that the parametrization of the relevant small scale mixing is not adequate. The model still requires validation of turbulent mixing behaviour and the friction parameter. Other limitations are found in certain modelling choices and the lack of a proper quantification of vertical mixing efficiency. Therefore, there is still a knowledge gap between this study and the behaviour in the RWW. This study provides a step forward in closing this gap. Insights are gained into possible improvements of the method and possibilities for additional research. Taking these steps will finally provide an answer on the effectiveness of internal waves generated over undular topography as a salt intrusion mitigation measure in the RWW, where the mitigation measure might eventually be applied to other vulnerable deltas worldwide.

<sup>1</sup>For a two-layered stratified system the internal wave at the interface has an amplitude of a factor  $\frac{\rho_{\text{bottom}} - \rho_{\text{surface}}}{\rho_{\text{surface}}} \frac{H_2}{H}$  larger than the amplitude of the surface wave. Here  $H$  is the total water depth and  $H_2$  the water depth of the bottom layer.

## Conclusions and recommendations

Salt intrusion in estuaries is an increasingly relevant problem. This study investigates whether internal waves generated over undular bottom topography can contribute to vertical mixing and hereby have the potential to be a good salt intrusion mitigation measure, the main question is:

*Can internal waves, generated over bottom topography, contribute to vertical mixing and hereby reduce stratification in estuaries?*

This question is approached by simulating a stratified 2D channel with sinusoidal bed waves with a non-hydrostatic numerical model. Bottom topography configurations have bottom topography amplitudes ranging between 0.25 and 1.5 meter and bottom topography wavelengths ranging between 20 and 70 meter.

This chapter draws conclusions of the study by answering the main question and the subquestions proposed in Section 1.3. Finally, recommendations on improvement of this study are proposed.

### 7.1 Conclusions

In all simulations resonant internal waves are generated. Internal waves with a mode one structure are the most energetic waves. An analytical expression for internal wave energy density of linear internal waves generated over sinusoidal bottom topography is given by Equation 3.12. This equation describes the influence of the relevant parameters on the magnitude of internal wave energy density and the moments of resonance. When the background flow has the same magnitude as the wave celerity of the free wave, resonance occurs. This is when the horizontal wave number of the free wave coincides with the wave number of the bottom topography. The parameters in the numerator (bottom topography amplitude, bottom topography wave number and background flow velocity) amplify the magnitude.

Mode one is the most energetic wave mode. The amount of internal wave energy computed in the numerical modelling cases are between 0.4 and 6.7 percent of the potential energy anomaly (PEA), which is the amount of energy required to fully mix a stratified water column.

The hypothesis was that this internal wave energy would be transmitted to turbulent kinetic energy (TKE) and mixing by shear instabilities and wave breaking. For the stable trapped internal waves observed in the model results, the internal wave energy is transmitted to TKE through shear instabilities near the bed. Internal wave breaking is only found for unrealistic cases in this study, where wave breaking is observed for internal waves reflecting at the boundaries that interfere with internal waves already present in the centre of the domain. From this however can be concluded that internal wave breaking can be resolved in the model.

For the considered cases the relative increase in total potential energy is 6% to 99% compared to a similar case without bottom topography. This relative increase in potential energy is caused by the interaction of bed friction and flow velocity, and is therefore not merely related to vertical mixing. First of all, flow over a rough bottom creates a mixing layer, which is enhanced during occurrences of internal waves. In the cases with bottom topography the flow has to overcome additional resistance in the bed wave domain. This is compensated for by

lowering the pressure by means of tilted isopycnals in downstream direction. Consequently, there is a positive net horizontal buoyancy flux.

The bottom topography amplitude has the strongest influence on internal wave energy and mixing. The relative increase in potential energy increases for increasing bottom topography amplitude. This can be explained by larger instability regions near the bed for increasing bottom topography amplitude. Additionally, higher bed waves also have a larger bed area and hence more bed resistance. The relative increase in potential energy decreases for increasing bottom topography wavelength. This could be explained by a decrease in bed area (and thus in bed resistance) for longer bed waves.

Reflecting on the main research question, there is an increased amount of vertical mixing present when undular bottom topography is applied in a stratified channel. However, it is yet to be quantified how significant the mixing caused by internal waves is.

## 7.2 Recommendations

The results of this study give insight into how to further approach the problem. These recommendations follow from the Discussion (Chapter 6), this section only elaborates on the most important recommendations.

### Representation of vertical mixing in the model

Mixing due to small-scale shear instabilities was not reproduced by the currently used model. Increasing the model resolution to the relevant mixing scales is not considered a feasible solution, therefore the problem can be solved by a better validation on mixing. The unresolved mixing could be better represented in the model. A closure for transport and mixing of the solved constituent (salt in this case) could be defined similarly to a subgrid closure for the turbulent transport of momentum. Subgrid diffusion can be calculated as a function of turbulent dissipation and a mixing efficiency. This however would require an estimation of the small scale mixing efficiency, which has to be determined from lab experiments or Direct Numerical Simulations (DNS).

### Influence of bottom friction induced processes

Wave-induced shear instabilities were only found near the bed in this study, and the system shows a high sensitivity to variations in bed friction. Therefore the friction parameter requires validation. This is a first step towards a proper quantification of bed friction induced mixing processes.

### Significance of internal wave mixing for salt intrusion

The amount of generated internal wave energy is related to the PEA in this study. The change in the PEA does not have direct relation to salt intrusion. Alternatively, the significance of mixing by internal waves could be determined similarly to the approach of Pietrzak et al. (1991). Here the turbulence production of the internal waves is related to the turbulence production of the background flow.

### Additional modelling cases

This study focuses on a 2D domain where the local behaviour of internal waves is investigated. Consequently, several effects that might improve vertical mixing are not considered in this case. In a 3D channel, internal waves could break at the banks. For a longer domain waves could also interfere with other internal waves or objects, leading to breaking. Optimization cases for different bed wave designs could be considered:

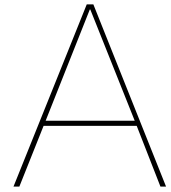
- The effect of the length of the region where bed waves are applied;
- Effect of combination of bottom topography wavelengths and/or bottom topography amplitudes;

An example is that collision of internal waves could be purposely induced. Two regions of bed waves with different bottom topography wavelengths should be positioned with some distance from each other. For a varying background flow the internal waves will be generated at different time instances and the trapped waves will be released at different moments. When the internal waves interfere and collide they could break.

# Bibliography

- Bahari, M. and Hejazi, K. (2009). Investigation of Buoyant Parameters of  $k-\epsilon$  Turbulence Model in Gravity Stratified Flows. *World Academy of Science, Engineering and Technology*, 55:537–544.
- Chen, Z.-W., Xie, J., Xu, J., Zhan, J.-M., and Cai, S. (2013). Energetics of nonlinear internal waves generated by tidal flow over topography. *Ocean Modelling*, 68:1–8.
- Drinkwaterplatform (2019). Verzilting: een bedreiging voor ons drinkwater? Available at <https://www.drinkwaterplatform.nl/verzilting-drinkwater/>.
- Ericson, J., Vorosmarty, C., Dingman, S., WARD, L., and Meybeck, M. (2006). Effective sea-level rise and deltas: Causes of change and human dimension implications. *Global and Planetary Change*, 50(1-2):63–82.
- Geyer, W. R. and MacCready, P. (2014). The Estuarine Circulation. *Annual Review of Fluid Mechanics*, 46(1):175–197.
- Groenenboom, J., Kranenburg, W., Laan, S., and Kester, J. (2019). Strategisch Baggeren; Onderdeel van KPP CIP 2019. Technical report, Deltares.
- Groenenboom, J. and Veenstra, J. (2017). Beperking Zoutindringing Nieuwe Waterweg-CIP 2017: Studie naar de effecten van openingen in de Splitsingsdam, pompschepen en bellenboten. Technical report, Deltares.
- Hogg, C. A. R., Egan, G. C., Ouellette, N. T., and Koseff, J. R. (2017). Shoaling internal waves may reduce gravity current transport. *Environmental Fluid Mechanics*, 18(2):383–394.
- Holloway, G. (1988). The buoyancy flux from internal gravity wave breaking. *Dynamics of Atmospheres and Oceans*, 12(2):107–125.
- Huismans, Y., van der Wijk, R., Fujisaki, A., and Sloff, C. (2018). Zoutindringing in de Rijn-Maasmonding; Knelpunten en effectiviteit stuurknoppen. Technical Report 11200589-001, Deltares.
- Klymak, J., Legg, S., Alford, M., Buijsman, M., Pinkel, R., and Nash, J. (2012). The Direct Breaking of Internal Waves at Steep Topography. *Oceanography*, 25(2):150–159.
- Kranenburg, C. (1988). Long internal waves and turbulence production in estuarine flows. *Estuarine, Coastal and Shelf Science*, 27(1):15–32.
- Kranenburg, C., Pietrzak, J. D., and Abraham, G. (1991). Trapped internal waves over undular topography. *Journal of Fluid Mechanics*, 226:205–217.
- Kranenburg, W. and van der Kaaij, T. (2019). Dispersiemechanismen in de Rijn-Maasmonding; Verkenning van de verhouding tussen zouttransportprocessen middels zoutfluxdecompositie. Technical report, Deltares.
- Kundu, P. K., Cohen, I. M., and Dowling, D. R. (2016). *Fluid mechanics*, volume 4, chapter 8, pages 392–402. Academic Press, San Diego, 6 edition.
- Labeur, S. (2009). *Finite element modelling of transport and non-hydrostatic flow in environmental fluid mechanics*. s.n, S.I.
- Lamb, K. G. (2014). Internal Wave Breaking and Dissipation Mechanisms on the Continental Slope/Shelf. *Annual Review of Fluid Mechanics*, 46(1):231–254.
- Laurent, L. C. S., Toole, J. M., and Schmitt, R. W. (2001). Buoyancy Forcing by Turbulence above Rough Topography in the Abyssal Brazil Basin. *Journal of Physical Oceanography*, 31(12):3476–3495.
- Lerczak, J. A., Geyer, W. R., and Ralston, D. K. (2009). The Temporal Response of the Length of a Partially Stratified Estuary to Changes in River Flow and Tidal Amplitude. *Journal of Physical Oceanography*, 39(4):915–933.

- McEwan, A. D. (1983). Internal mixing in stratified fluids. *Journal of Fluid Mechanics*, 128(-1):59.
- Mikhailova, M. V. (2013). Processes of seawater intrusion into river mouths. *Water Resources*, 40(5):483–498.
- Moum, J. N., Klymak, J. M., Nash, J. D., Perlin, A., and Smyth, W. D. (2007). Energy Transport by Nonlinear Internal Waves. *Journal of Physical Oceanography*, 37(7):1968–1988.
- Nieuwstadt, F. T. M., Boersma, B. J., and Westerweel, J. (2016). *Turbulence*. Springer-Verlag GmbH.
- NWO (2020). SALTISolutions – Salt intrusion through urbanizing deltas: Solutions. Available at <https://www.nwo.nl/en/research-and-results/programmes/ttw/perspectief/2019-saltisolutions.html>.
- Peltier, W. R. and Caulfield, C. P. (2003). MIXING EFFICIENCY IN STRATIFIED SHEAR FLOWS. *Annual Review of Fluid Mechanics*, 35(1):135–167.
- Pietrzak, J. and Labeur, R. J. (2004). Trapped internal waves over undular topography in a partially mixed estuary. *Ocean Dynamics*, 54(3-4).
- Pietrzak, J. D., Kranenburg, C., and Abraham, G. (1990). Resonant internal waves in fluid flow. *Nature*, 344(6269):844–847.
- Pietrzak, J. D., Kranenburg, C., Abraham, G., Kranenburg, B., and van der Wekken, A. (1991). Internal Wave Activity in Rotterdam Waterway. *Journal of Hydraulic Engineering*, 117(6):738–757.
- Pörtner, H.-O., Roberts, D., Masson-Delmotte, V., Zhai, P., Tignor, M., Poloczanska, E., Mintenbeck, K., Nicolai, M., Okem, A., Petzold, J., Rama, B., and (eds.), N. W. (2019). IPCC Special Report on the Ocean and Cryosphere in a Changing Climate. In *IPCC, 2019: Summary for Policymakers*.
- Rijkswaterstaat (2020a). Nieuwe Waterweg. Available at <https://www.rijkswaterstaat.nl/water/voorwaarden/overzicht/nieuwe-waterweg/>.
- Rijkswaterstaat (2020b). Verzilting. Available at <https://www.rwsleefomgeving.nl/@122136/verzilting-versus/>.
- Schulz, E. (2014). *Residual circulation in tidally energetic estuaries: contributions and dependencies*. PhD thesis, Universität Rostock.
- Schönfeld, J. and Kranenburg, C. (1977). *Dichtheidsstromen en interne golven: Collegehandleiding*. TU Delft, Department of Hydraulic Engineering. Available at <http://resolver.tudelft.nl/uuid:55eb3a2f-8ddd-4edc-a35e-d88d78558eb0>.
- Simpson, J. H., Brown, J., Matthews, J., and Allen, G. (1990). Tidal Straining, Density Currents, and Stirring in the Control of Estuarine Stratification. *Estuaries*, 13(2):125.
- Staquet, C. and Sommeria, J. (2002). Internal Gravity Waves: From Instabilities to Turbulence. *Annu. Rev. Fluid Mech.*
- Taylor, J. R. (1992). The energetics of breaking events in a resonantly forced internal wave field. *Journal of Fluid Mechanics*, 239(-1):309.
- Uittenbogaard, R. (1995). *The importance of internal waves for mixing in a stratified estuarine tidal flow*. PhD thesis, TU Delft.
- Uittenbogaard, R. and Imberger, J. (1993). The importance of internal waves for mixing in a stratified estuarine tidal flow. Technical report, Delft Hydraulics. Part two: tables and figures.
- Van der Boon, C. M. (2011). Numerical modelling of internal waves in the browse basin. Master's thesis, TU Delft.
- Van der Heijden, J. (2018). Strategical Dredging Measures; CIP 2018: Effects of strategical dredging measures on salt water intrusion in the Nieuwe Waterweg. Technical Report 11202197-004, Deltares.
- Venayagamoorthy, S. K. and Koseff, J. R. (2016). On the flux Richardson number in stably stratified turbulence. *Journal of Fluid Mechanics*, 798.
- Waterforum (2018). Zoutindringing vanuit zee is nog steeds een probleem. Available at <https://www.waterforum.net/zoutindringing-vanuit-zee-is-nog-steeds-een-probleem/>.
- Zijta, M. (2019). Internship report: Internal waves in the Nieuwe Waterweg. Onderdeel van KPP CIP 2019.



# Case description: the Rotterdam Waterway

The case study will focus on the Rotterdam Waterway (RWW), which connects the Rhine and the Meuse to the North Sea.

## Characteristics of the RWW

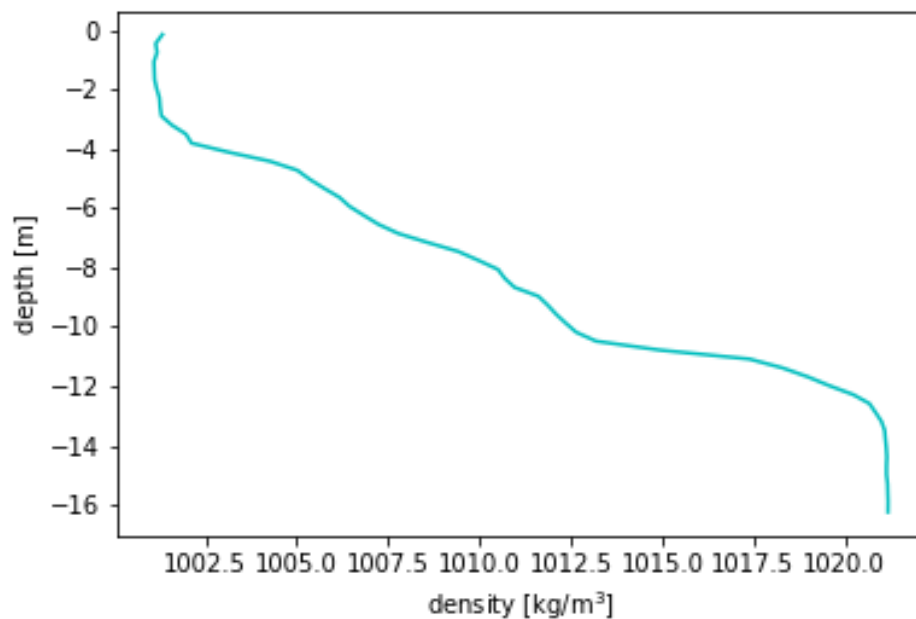


Figure A.1: Characteristic density profile of the RWW, measurement taken at 16:07 near Hoek van Holland (51.9732313, 4.121972) on 06-07-2016

The RWW is a manmade channel in the Rhine-Meuse Delta that runs from Hoek van Holland till the Maeslantkering. The approach channel of the Rotterdam Harbour is frequently dredged, and has a depth varying between -16,20 and -14,50 NAP. The length of the RWW is 7 km and after that the channel becomes Het Scheur and subsequently de Nieuwe Maas (Rijkswaterstaat, 2020a). Pietrzak et al. (1990) found periodic bed forms with wavelengths and amplitudes varying between 30-50 m and 0.5-1 m respectively. The most important time scales in the RWW are related to the tide. The North Sea has a semi-diurnal tidal cycle (M2), which is approximately 12.5 hours. The spring-neap tidal cycle is about 14.5 days. The river discharge in the RWW is 800-1500 m<sup>3</sup>/s and the flow velocity of the river is 0.13-0.25 m/s. The tidal flow velocity varies between 0.9-1.2 m/s (Groenen-

boom et al., 2019). The estuary can be classified as partially-mixed (Pietrzak et al., 1990). Depending on the hydrodynamic forcing it varies between a stratified and a vertically well-mixed density profile (Kranenburg and van der Kaaij, 2019)

Table A.1: Typical parameters RWW (Rijkswaterstaat, 2020a, Zijta, 2019)

Parameter	Dimension	Unit
River discharge	800-1500	m <sup>3</sup> /s
Flow velocity (river)	0.13-0.25	m/s
Flow velocity (tidal)	0.9-1.2	m/s
Density (Fresh water)	1000	kg/m <sup>3</sup>
Density (Salt water)	1015	kg/m <sup>3</sup>
River width near the bed	400	m
River width near the surface	600	m
River depth	15	m

## Critical conditions salt intrusion

Kranenburg and van der Kaaij (2019) conducts a salt flux decomposition of the RWW by breaking up components of results from 3D simulations, where lateral variations in bathymetry and salinity are neglected. Gravitational circulation is found to be the dominant mechanism for salt intrusion in the RWW most of the time. Except for during a set-up event, when the gravitational circulation is strongly reduced. During set-up events the net flow in the RWW is landward directed for a short period, leading to an influx of salt water. A balance exists between river discharge and tidal forcing as described in Section 2.1. In the RWW gravitational circulation is the dominant salt import mechanism, which means a low river discharge enhances salt intrusion. According to Huisman et al. (2018) a critical condition for salt intrusion is a river discharge measured by Lobith of  $Q_{Lobith} = 2000 \text{ m}^3/\text{s}$ . Below this discharge salt intrusion in the RWW increases significantly and strong stratification is observed Groenenboom et al. (2019). With low discharges the estuary moves more landward (to the right in Figure A.2) and hence salt intrudes further landward.

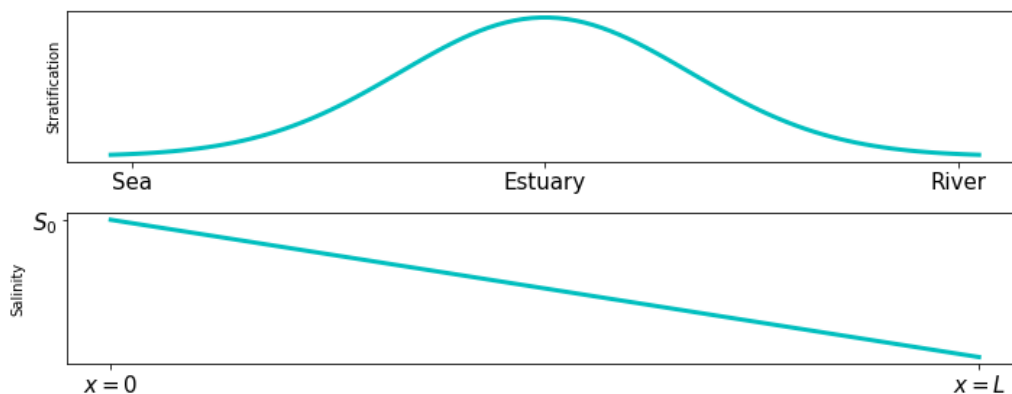


Figure A.2: a) Schematic of stratification in an estuary, adapted from Groenenboom et al. (2019)  
b) Idealized cross-sectionally averaged salinity vs distance along estuary, adapted from Lerczak et al. (2009)

# B

## Resonance conditions

This appendix shows plots of internal wave amplitude  $\zeta$  for different bottom topography wavelengths  $L_\tau$ . The plots show at which background flow velocities  $U_0$  resonance occurs.

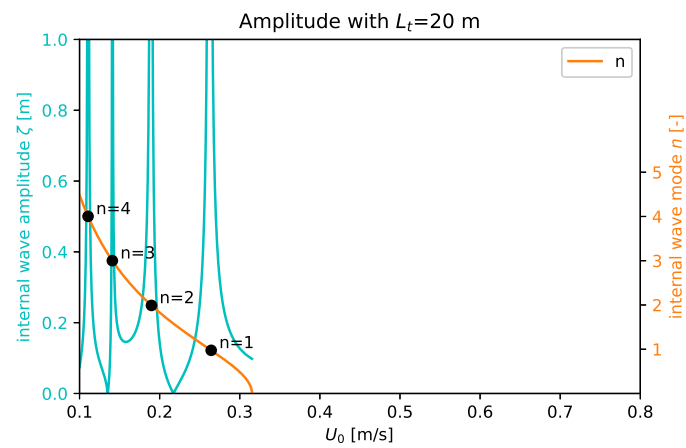


Figure B.1: Magnitude of the internal wave amplitude  $\zeta$  for varying background flow velocity  $U_0$ . Resonant conditions are met for flow velocities of 0.26, 0.19, 0.14 and 0.11 m/s with corresponding internal modes 1, 2, 3 and 4 respectively. Internal wave modes are marked with black dots (indicated on the right y-axis). Here  $L_\tau = 20$  m,  $N = 0.099$  s $^{-1}$

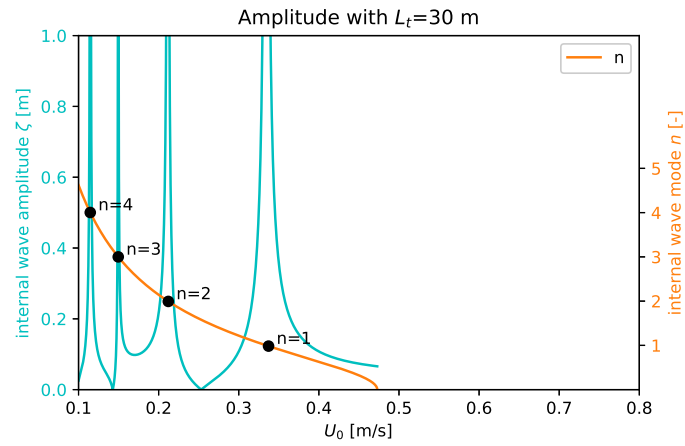


Figure B.2: Magnitude of the internal wave amplitude  $\zeta$  for varying background flow velocity  $U_0$ . Resonant conditions are met for flow velocities of 0.34, 0.21, 0.15 and 0.11 m/s with corresponding internal modes 1, 2, 3 and 4 respectively. Internal wave modes are marked with black dots (indicated on the right y-axis). Here  $L_\tau = 30$  m,  $N = 0.099$  s $^{-1}$

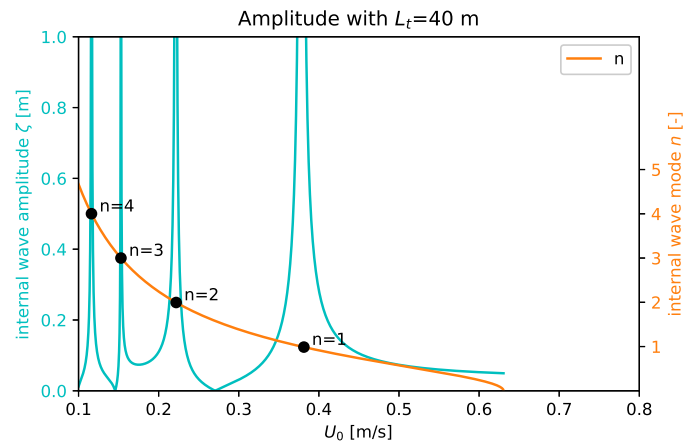


Figure B.3: Magnitude of the internal wave amplitude  $\zeta$  for varying background flow velocity  $U_0$ . Resonant conditions are met for flow velocities of 0.38, 0.22, 0.15 and 0.12 m/s with corresponding internal modes 1, 2, 3 and 4 respectively. Internal wave modes are marked with black dots (indicated on the right y-axis). Here  $L_\tau = 40$  m,  $N = 0.099$  s $^{-1}$

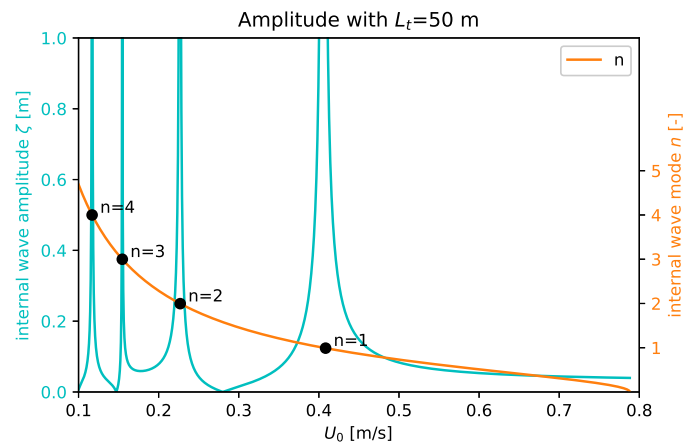


Figure B.4: Magnitude of the internal wave amplitude  $\zeta$  for varying background flow velocity  $U_0$ . Resonant conditions are met for flow velocities of 0.41, 0.23, 0.15 and 0.12 m/s with corresponding internal modes 1, 2, 3 and 4 respectively. Internal wave modes are marked with black dots (indicated on the right y-axis). Here  $L_\tau = 50$  m,  $N = 0.099$  s $^{-1}$

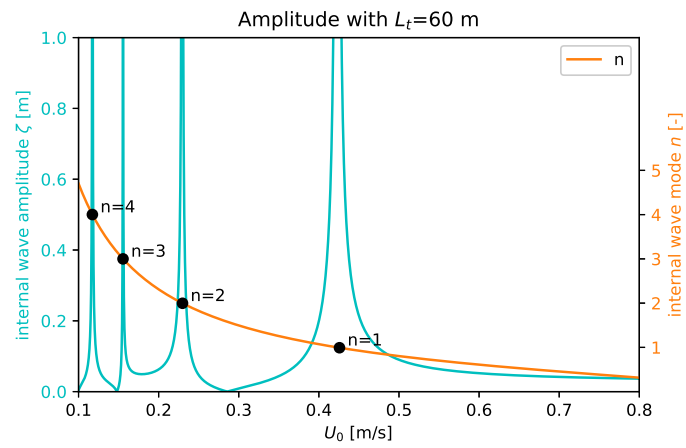


Figure B.5: Magnitude of the internal wave amplitude  $\zeta$  for varying background flow velocity  $U_0$ . Resonant conditions are met for flow velocities of 0.43, 0.23, 0.16 and 0.12 m/s with corresponding internal modes 1, 2, 3 and 4 respectively. Internal wave modes are marked with black dots (indicated on the right y-axis). Here  $L_\tau = 60$  m,  $N = 0.099$  s $^{-1}$

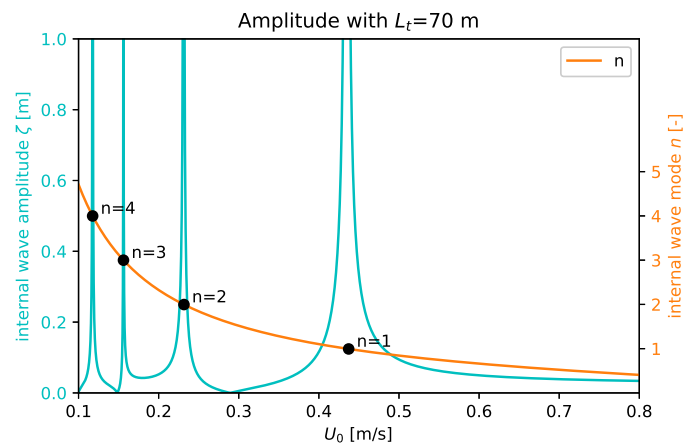
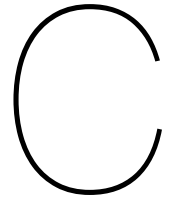


Figure B.6: Magnitude of the internal wave amplitude  $\zeta$  for varying background flow velocity  $U_0$ . Resonant conditions are met for flow velocities of 0.44, 0.23, 0.16 and 0.12 m/s with corresponding internal modes 1, 2, 3 and 4 respectively. Internal wave modes are marked with black dots (indicated on the right y-axis). Here  $L_\tau = 70$  m,  $N = 0.099$  s $^{-1}$



## Workings of depth-averaging

Depth average of  $\hat{w}^2(z)$  (Equation 3.10) can be described by the following integral

$$\overline{\hat{w}^2(z)} = \frac{1}{H} \int_0^H \hat{w}^2 \cdot \sin^2 \left[ (l^2 - k^2)^{1/2} (H - z) \right] dz \quad (\text{C.1})$$

It can be written in alternative form with  $A = (l^2 - k^2)^{1/2}$

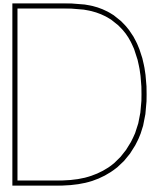
$$\frac{\hat{w}^2(z)}{H} \int \sin^2 [A(H - z)] dz = \frac{\hat{w}^2}{H} \frac{2A(z - H) + \sin(2A(H - z))}{4A} \quad (\text{C.2})$$

Solving the integral between the surface with rigid lid  $z = H$  and channel depth  $z = 0$

$$\overline{\hat{w}^2(z)} = \frac{\hat{w}^2}{H} \frac{2A(z - H) + \sin(2A(H - z))}{4A} \Bigg|_0^H = \frac{\hat{w}^2}{H} \left[ \frac{0 + \sin(0)}{4A} - \frac{-2H \cdot A + \sin(2H \cdot A)}{4A} \right] \quad (\text{C.3})$$

Re-substitution of  $A$  gives

$$\overline{\hat{w}^2(z)} = \hat{w}^2 \left( \frac{1}{2} - \frac{\sin \left[ 2H (l^2 - k^2)^{1/2} \right]}{4H (l^2 - k^2)^{1/2}} \right) \quad (\text{C.4})$$



## Model settings

Here an overview of model settings is given for the validation case (Chapter 4) and for the RWW case (Chapter 5).

### Validation case

Parameter	Setting	Unit
Left boundary condition	Free slip	
Right boundary condition	Wave paddle	
Surface boundary condition	Free slip (rigid lid)	
Bottom boundary condition	Free slip	
Initial conditions	Linearly stratified	
Horizontal grid size	4.92	mm
Vertical grid size	8.83	mm
Time step	0.1	s
Simulation duration	6000	s
Time discretization method	Fractional-Step	
Implicitness mom equation	0.5	
Implicitness cont equation	0.5	
Turbulence model	LES	
Prandtl-Schmidt number	1.0	

Table D.1: Model settings validation case

## RWW case

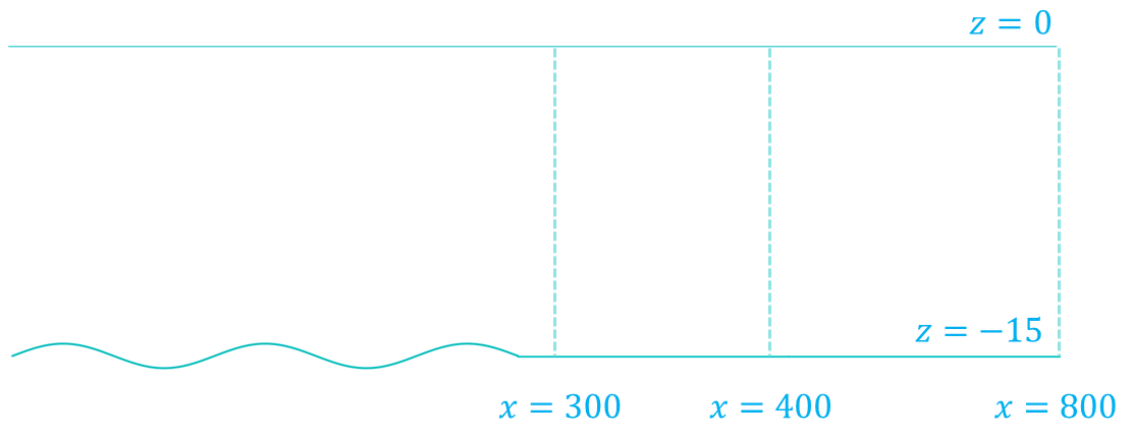
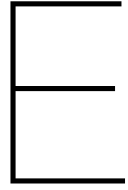


Figure D.1: Domain discretization where the domain has three different regions with different horizontal resolution

Parameter	Setting	Unit
Left boundary condition	Velocity	
Right boundary condition	Velocity	
Surface boundary condition	Free slip (rigid lid)	
Bottom boundary condition	Wall	
Transport inflow	Linearly stratified	
Initial conditions	Linearly stratified	
Horizontal grid size for $ x  = [400, 800]$	2.0	m
Horizontal grid size for $ x  = [300, 400]$	1.0	m
Horizontal grid size for $ x  = [0, 300]$	0.5	m
Vertical grid size	0.375	m
Time step	2.0	sec
Simulation duration	6	hours
Time discretization method	Crank-Nicolson	
Implicitness mom equation	1.0	
Implicitness cont equation	0.5	
Turbulence model	LES	
Prandlt-Schmidt number	1.0	

Table D.2: Model settings RWW case



## Derivation energy change FinLab

FinLab resolves the incompressible Navier-Stokes equations and the transport equation for salinity with the Boussinesq assumption (see Equations (4.1) to (4.3)).

To get to the energy equation the momentum equation (Equation 4.2) is multiplied with the velocity vector  $\vec{u}$ , which yields Equation E.1 and the density equation (Equation 4.3) is multiplied with  $gz$  which yields Equation E.2.

$$\frac{\partial \frac{1}{2} |\vec{u}|^2}{\partial t} + \vec{u} \cdot \nabla \left( \frac{1}{2} |\vec{u}|^2 \right) + g\vec{u} \cdot \nabla h + g \frac{\Delta \rho}{\rho_0} u_z - \nabla \cdot (\nu \nabla \vec{u}) \cdot \vec{u} = 0 \quad (\text{E.1})$$

$$\frac{\partial gz \Delta \rho}{\partial t} + gz \vec{u} \cdot \nabla (\Delta \rho) - gz \nabla \cdot (\kappa \nabla \Delta \rho) = 0 \quad (\text{E.2})$$

The momentum equation is multiplied by reference density  $\rho_0$ , then Equations (E.1) and (E.2) are added. Thereafter it is integrated over the domain of the tank. This integration uses the Gauss's theorem (divergence theorem).

$$\begin{aligned} \frac{d}{dt} \int_{\text{domain}} \left( \frac{1}{2} \rho_0 |\vec{u}|^2 + gz \Delta \rho \right) dx + \int_{\text{domain}} g \Delta \rho u_z dx \\ + \int_{\text{domain}} \mu |\nabla \vec{u}|^2 dx - \int_{\text{domain}} -\Delta \rho g u_z dx + \int_{\text{domain}} g \kappa \frac{\partial \Delta \rho}{\partial z} dx = 0 \end{aligned} \quad (\text{E.3})$$

In the integration procedure some terms will cancel out, due to the divergence free flow (incompressible flow). For example:

$$\int_{\text{domain}} g\vec{u} \cdot \nabla h dx = \int_{\text{rand}} g\vec{u} \cdot \vec{n} h ds - \int_{\text{domain}} gh \nabla \cdot \vec{u} dx \quad (\text{E.4})$$

For a closed tank also the right hand side of Equation E.4 is zero because of incompressible flow ( $\nabla \cdot \vec{u} = 0$ ) and the flow perpendicular to the wall is equal to zero ( $\vec{u} \cdot \vec{n} = 0$ ).

Some more terms will cancel out, so hence the resultant equation is given by:

$$\frac{d}{dt} \int_{\text{domain}} \left( \frac{1}{2} \rho_0 |\vec{u}|^2 + gz \Delta \rho \right) dx = - \int_{\text{domain}} \mu |\nabla \vec{u}|^2 dx - \int_{\text{domain}} g \kappa \frac{\partial \Delta \rho}{\partial z} dx \quad (\text{E.5})$$

which is the same as:

$$\frac{d}{dt} \int_{\text{domain}} (E) dx = - \int_{\text{domain}} \mu |\nabla \vec{u}|^2 dx - \int_{\text{domain}} g \kappa \frac{\partial \Delta \rho}{\partial z} dx \quad (\text{E.6})$$

In Equation E.6 can be seen that the change in energy is caused by a viscous term and a diffusion term. The viscous term is always positive and thus causes a decrease in energy by dissipation. The diffusion term is negative for a stable stratification which implies  $\partial\Delta\rho/\partial z < 0$ .

Hence for a wave tank with length  $L$  the increase in energy is given by:

$$- \kappa g (\Delta\rho_{\text{surface}} - \Delta\rho_{\text{bottom}}) L \quad (\text{E.7})$$



## Additional figures

### Kinetic energy and vertical buoyancy plots

This section includes plots of the domain-averaged vertical density flux  $b$  and the domain-averaged kinetic energy as function of vertical velocity  $\overline{E_{k,z}}$  for all the cases where bottom topography parameters were varied. The base case is shown in Figure 5.4. Cases are labelled according to Table 5.2.

### Variations in bottom topography amplitude

Results of bottom topography amplitude  $h_0$  variations are shown below. The bottom topography wavelength is equal in all cases ( $L_\tau = 50$  m).

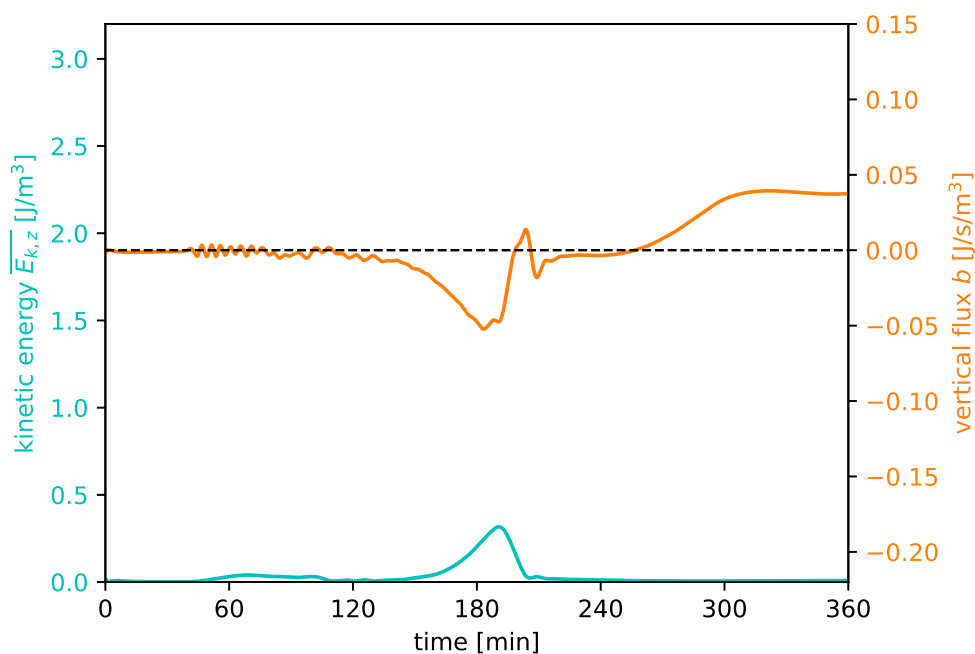


Figure F.1: Kinetic energy  $\overline{E_{k,z}}$  and vertical density flux  $b$  for case  $L50h025$

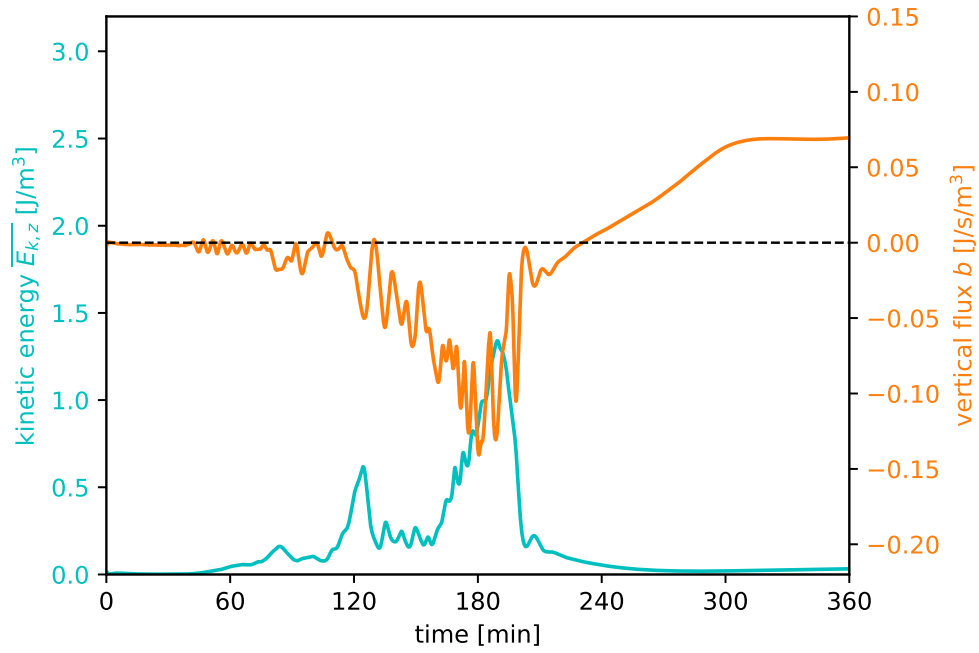


Figure F.2: Kinetic energy  $\overline{E_{k,z}}$  and vertical density flux  $b$  for the base case *L50h075*

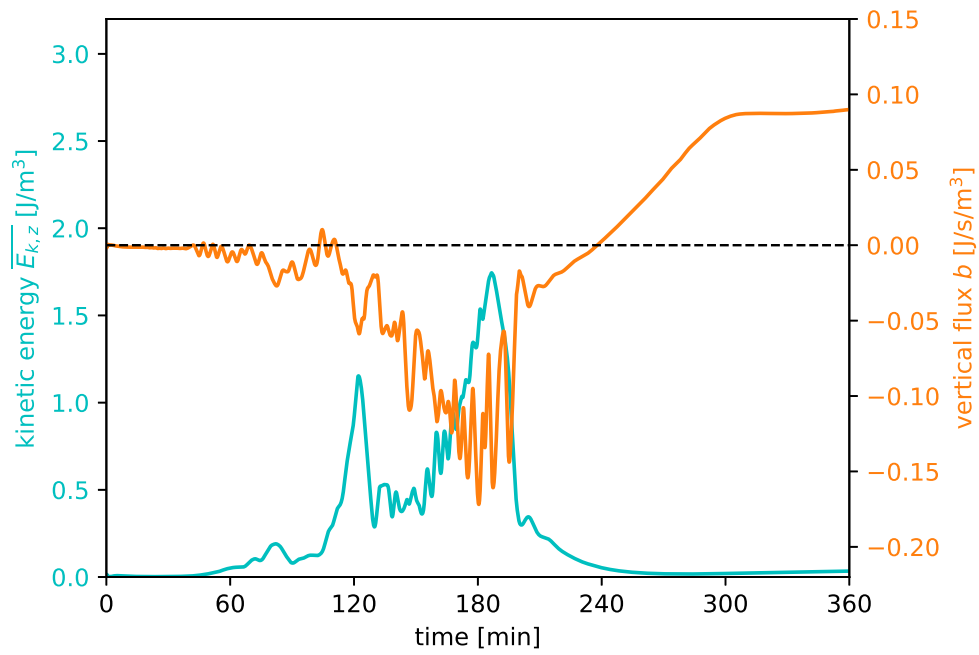


Figure F.3: Kinetic energy  $\overline{E_{k,z}}$  and vertical density flux  $b$  for the base case *L50h100*

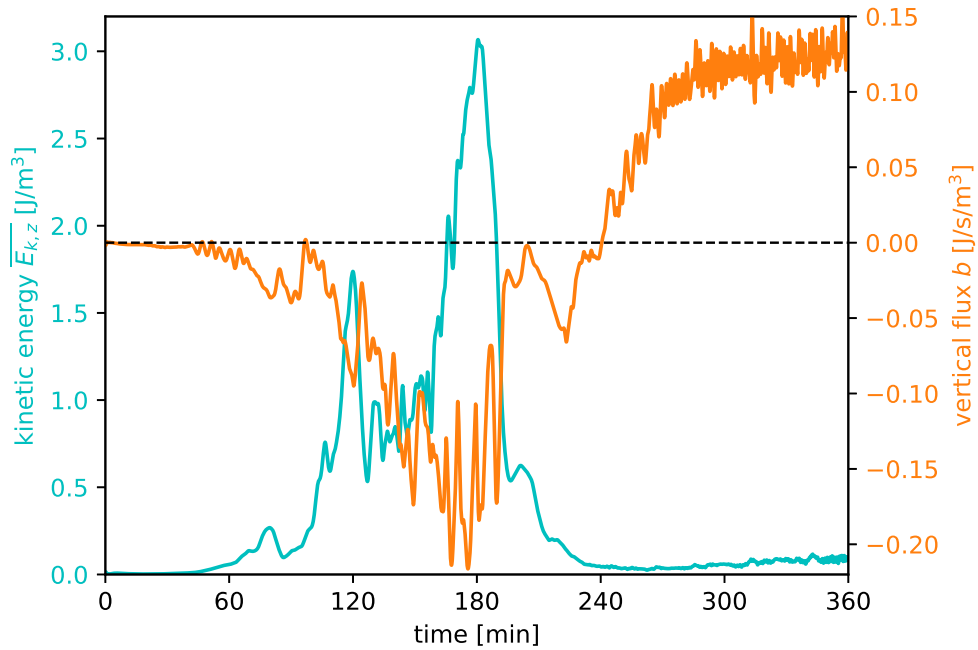


Figure F.4: Kinetic energy  $\overline{E_{k,z}}$  and vertical density flux  $b$  for the base case  $L50h150$

### Variations in bottom topography wavelength

Results of bottom topography wavelength  $L_\tau$  variations are shown below. The bottom topography amplitude is equal in all cases ( $h_0 = 0.5$  m).

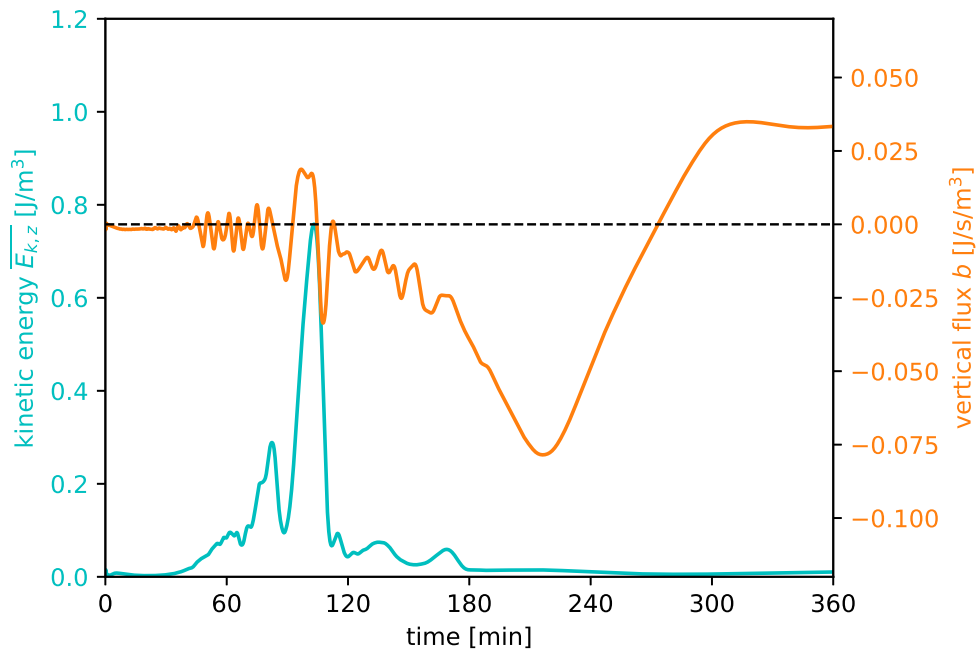


Figure F.5: Kinetic energy  $\overline{E_{k,z}}$  and vertical density flux  $b$  for the base case  $L20h050$

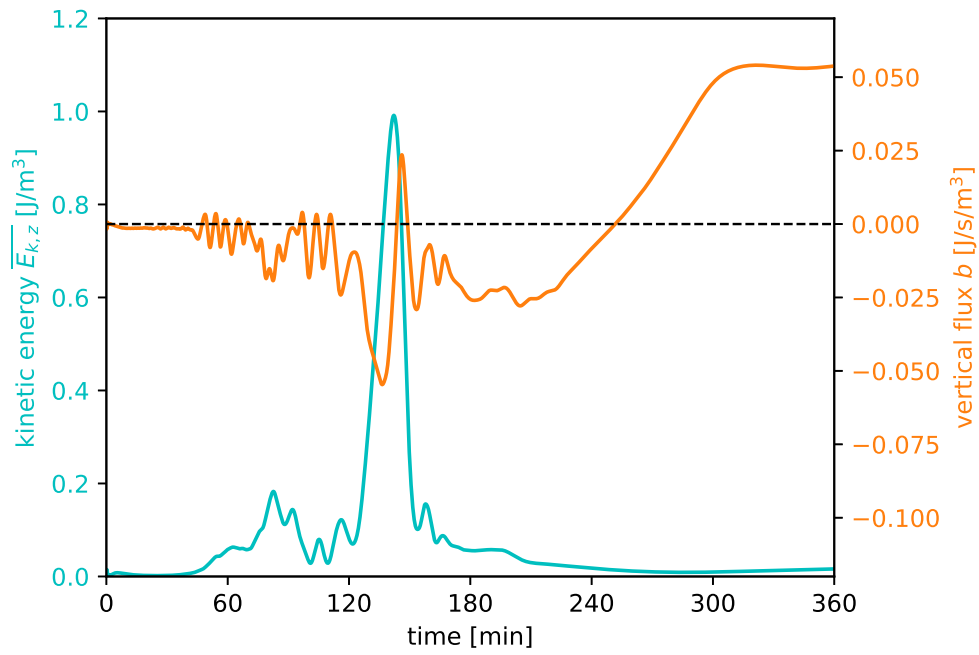


Figure F.6: Kinetic energy  $\overline{E_{k,z}}$  and vertical density flux  $b$  for the base case *L30h050*

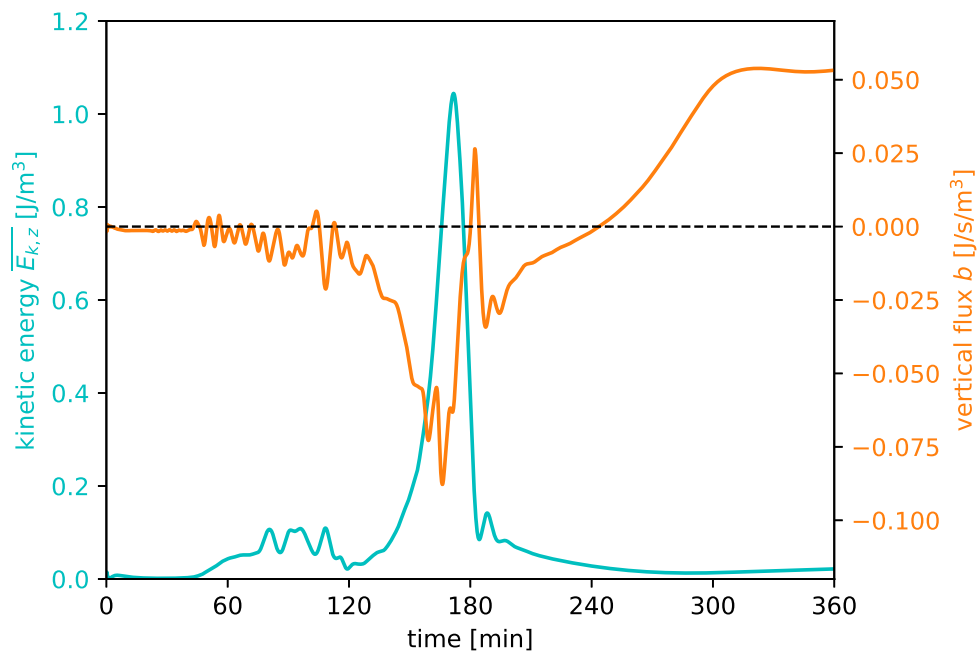


Figure F.7: Kinetic energy  $\overline{E_{k,z}}$  and vertical density flux  $b$  for the case *L40h050*

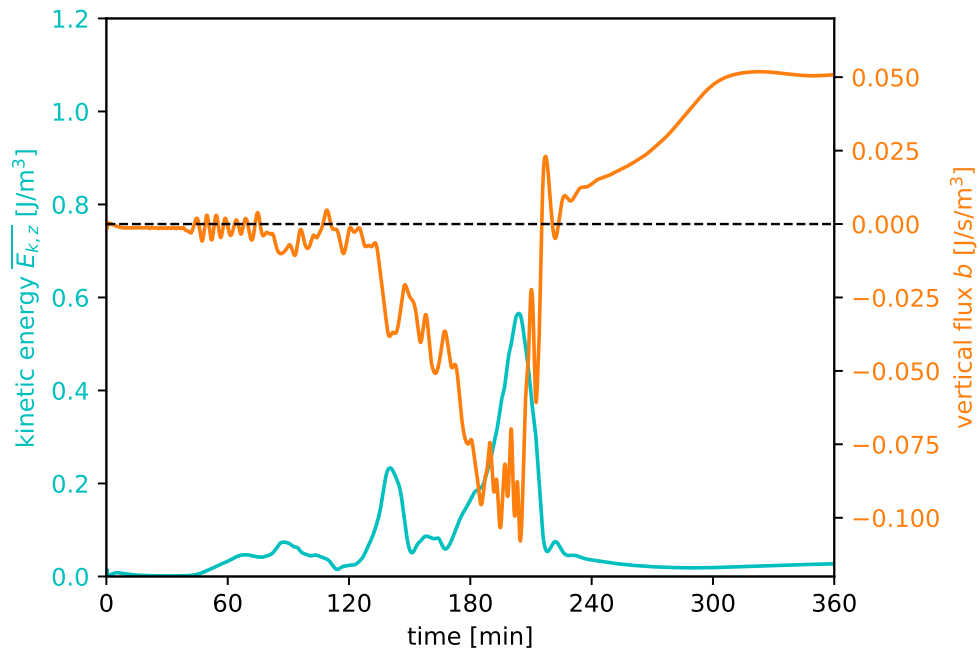


Figure F.8: Kinetic energy  $\overline{E_{k,z}}$  and vertical density flux  $b$  for the base case *L60h050*

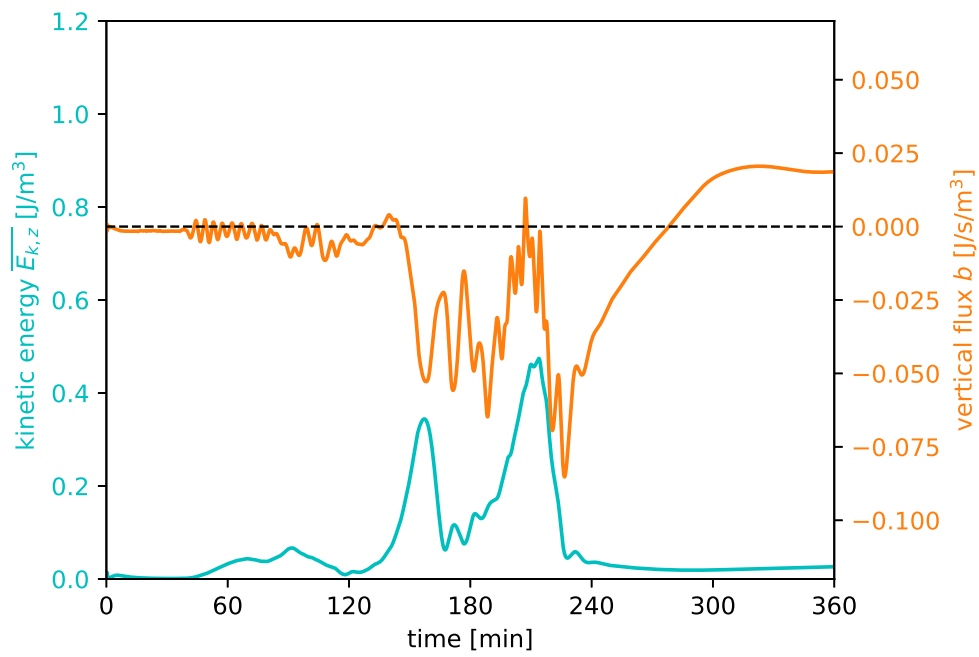


Figure F.9: Kinetic energy  $\overline{E_{k,z}}$  and vertical density flux  $b$  for the base case *L70h050*

## Influence of flow velocity

Chapter 5 concludes that the increase in  $\overline{E_p}$  and the positive values of the vertical buoyancy flux  $b$ , which are observed in cases both with and without bottom topography, are caused by the background velocity. This is the similar driving force in all considered cases. Hence this section further investigates the influence of flow velocity. First a half tidal cycle with an amplitude of 0.5 m/s is applied. Secondly the background flow linearly increases towards 0.5 m/s for the first 180 minutes after which it stays constant.

### Tidal flow with amplitude of 0.5 m/s

The RWW has a background flow governed by the tide. Therefore a simulation is done with half a tidal cycle. This case, however also introduces a problem with a lot of internal wave reflection at the boundaries.

Highest values of kinetic energy as function of vertical velocity  $\overline{E_{k,z}}$  for the case with bed waves is found at time instances where waves reflect at the boundaries, between  $t = 300$  and  $t = 360$  minutes (see Figure F.10c). At  $t = 180$  minutes there is the same flow velocity and resonance condition occurs as for linear flow, with 0.5 m/s a mode 1 response takes place. The density flux only starts being clearly positive for breaking waves. At this moment also  $Ri < 0.25$  is observed higher in the water column than for cases with linearly increasing flow velocity discussed in Section 5.4.1.

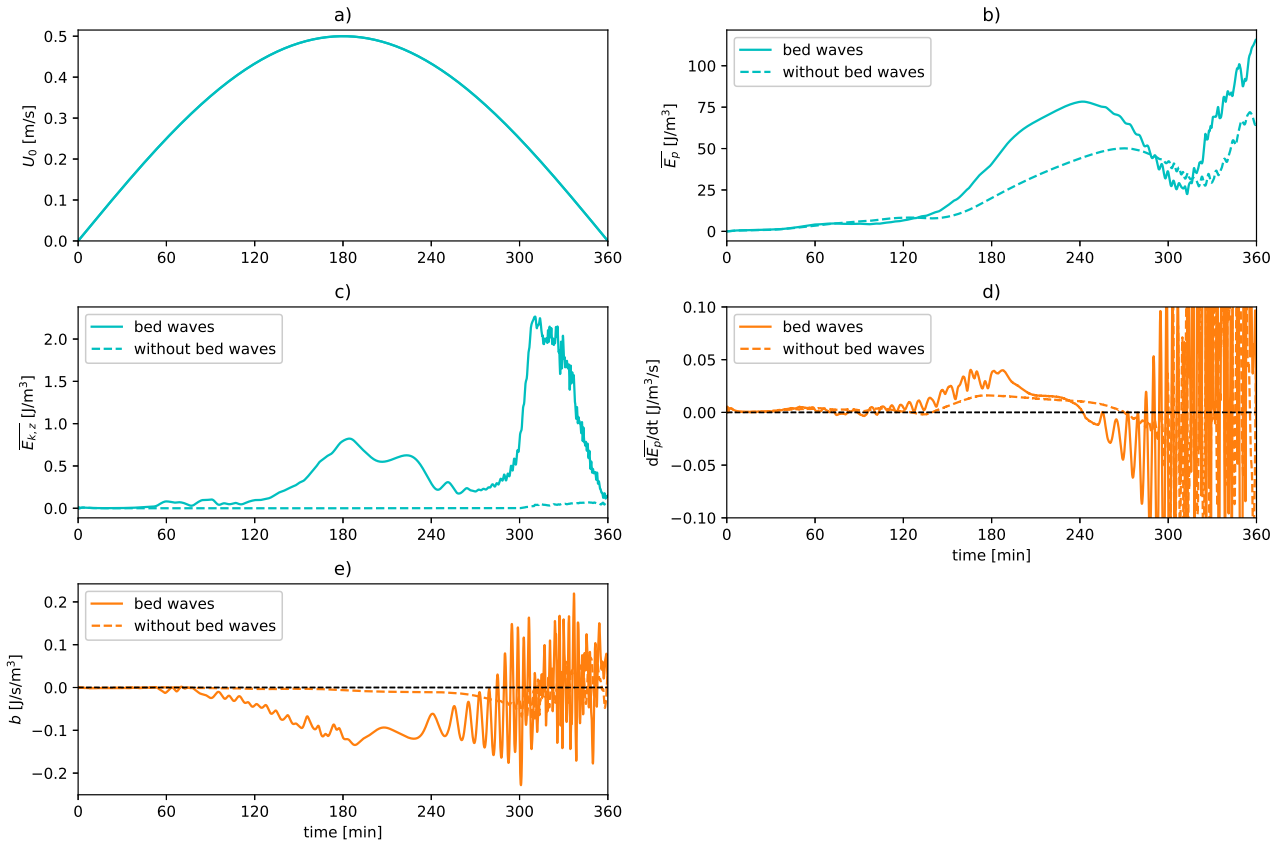


Figure F.10: Difference between the a case with (solid line) and without (dashed line) bottom topography for a case with tidal flow  $U_0$  with a velocity amplitude of 0.5 m/s. Domain-averaged kinetic energy  $\overline{E_{k,z}}$ , vertical buoyancy flux  $b$ , domain-averaged potential energy  $\overline{E_p}$  and total density flux  $\frac{d\overline{E_p}}{dt}$ .

Now the case without bed waves still shows a distinct increase in  $\overline{E_p}$ . However the magnitude of the increase is clearly larger in the case with bed waves. Till  $t = 120$  minutes the increase is equal, however from this point  $\overline{E_{k,z}}$  starts increasing and simultaneously the increase in  $\overline{E_p}$  is steeper for the case with bed and internal waves than for the case with a flat bed. For this case there is a longer time interval of mode 1 resonance, because the flow

velocity is near 0.5 m/s for a long time instance.

### Linearly increasing flow velocity up to 0.5 m/s

Here the flow velocity increases linearly up to 0.5 m/s for the first 180 minutes after which it stays at a constant velocity of 0.5 m/s. This is done to see the influence of lower background flow velocities. Figure F.11b shows a steeper increase in  $\overline{E_p}$  is visible for the case with bed waves between 180 and 240 minutes when the most energetic internal waves are present.

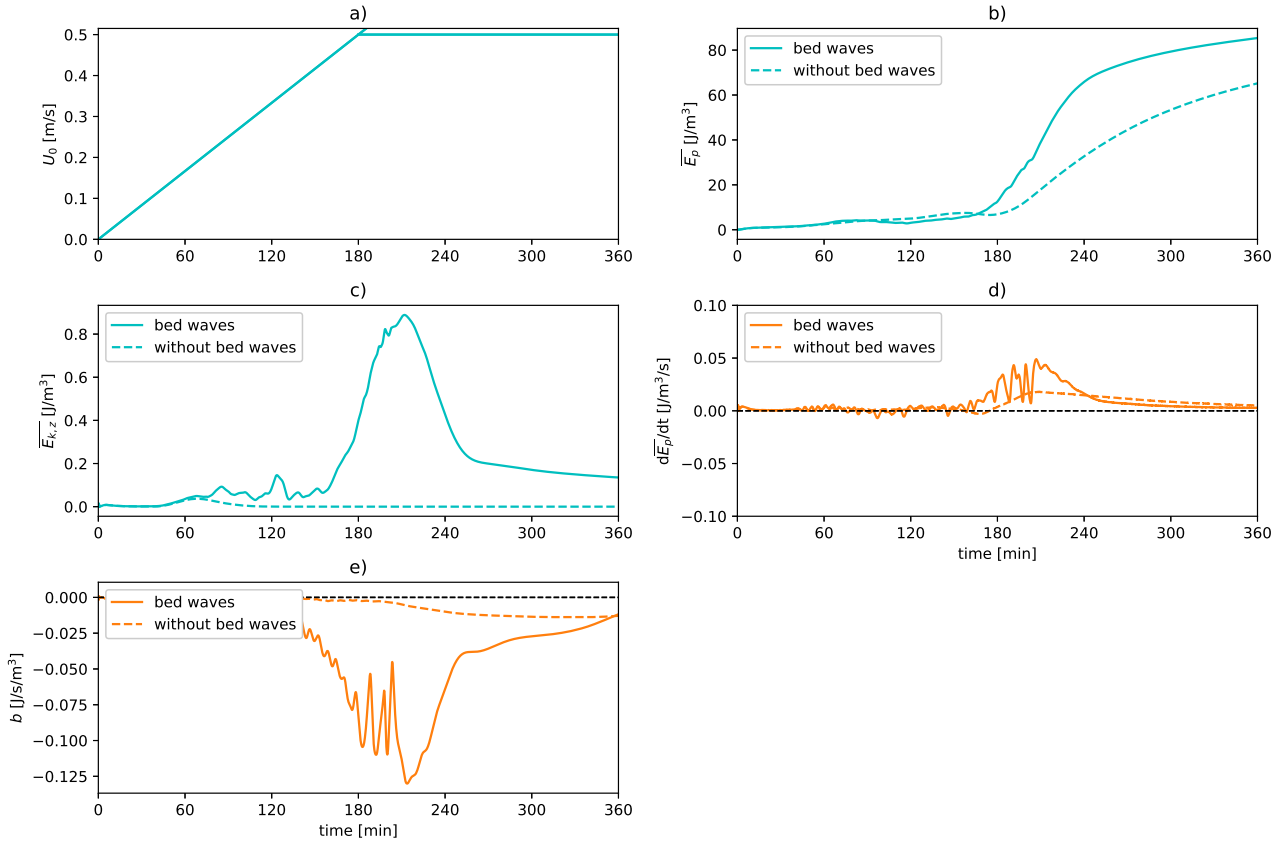


Figure F.11: Difference between the a case with (solid line) and without (dashed line) bottom topography for a case with a linearly increasing flow velocity up to a maximum of 0.5 m/s. Domain-averaged kinetic energy  $\overline{E_{k,z}}$ , vertical buoyancy flux  $b$ , domain-averaged potential energy  $\overline{E_p}$  and total density flux  $\frac{d\overline{E_p}}{dt}$ .

From both cases with and without bottom topography can be seen that  $U_0$  has a large influence on the change of  $\overline{E_p}$  (Figure F.11d). An accelerating background flow increases  $\overline{E_p}$ .